First-principles theory of dilute magnetic semiconductors

K. Sato

Graduate School of Engineering Science, Osaka University, 1-3 Machikaneyama,
Toyonaka, Osaka 560-8531, Japan

L. Bergqvist

Department of Physics and Astronomy, Uppsala University, P.O. Box 516,
SE-751 20 Uppsala, Sweden

J. Kudrnovský

Institute of Physics, Academy of Sciences of the Czech Republic, Na Slovance 2,
CZ-18221 Prague 8, Czech Republic

P. H. Dederichs

Institut für Festkörperforschung, Forschungszentrum Jülich, D-52425 Jülich, Germany

O. Eriksson

Department of Physics and Astronomy, Uppsala University, P.O. Box 516,
SE-751 20 Uppsala, Sweden

I. Turek

Institute of Physics of Materials, Academy of Sciences of the Czech Republic, Žižkova 22,
CZ-61662 Brno, Czech Republic

B. Sanyal

Department of Physics and Astronomy, Uppsala University, P.O. Box 516,
SE-751 20 Uppsala, Sweden

G. Bouzerar

Institut Néel, MCBT, CNRS, 25 Avenue des Martyrs, BP 166, 38042 Grenoble Cedex 9,
France

H. Katayama-Yoshida

Graduate School of Engineering Science, Osaka University, 1-3 Machikaneyama,
Toyonaka, Osaka 560-8531, Japan

V. A. Dinh

Computational Materials Science Center, National Institute of Material Science,
1-2-1 Sengen, Tsukuba, Ibaraki 305-0047, Japan

T. Fukushima

CNR/INFM, Department of Physics, University of L'Aquila, Stanza A1/43, Via Vetoio 10,
Coppito, L'Aquila, 67010 Abruzzo, Italy

H. Kizaki

Graduate School of Engineering Science, Osaka University, 1-3 Machikaneyama,
Toyonaka, Osaka 560-8531, Japan

R. Zeller

Institut für Festkörperforschung, Forschungszentrum Jülich, D-52425 Jülich, Germany

(Published 20 May 2010)

This review summarizes recent first-principles investigations of the electronic structure and magnetism of dilute magnetic semiconductors (DMSs), which are interesting for applications in spintronics. Details of the electronic structure of transition-metal-doped III-V and II-VI semiconductors are described, especially how the electronic structure couples to the magnetic properties of an impurity. In addition, the underlying mechanism of the ferromagnetism in DMSs is investigated from the

electronic structure point of view in order to establish a unified picture that explains the chemical trend of the magnetism in DMSs. Recent efforts to fabricate high-T_C DMSs require accurate materials design and reliable T_C predictions for the DMSs. In this connection, a hybrid method (*ab initio* calculations of effective exchange interactions coupled to Monte Carlo simulations for the thermal properties) is discussed as a practical method for calculating the Curie temperature of DMSs. The calculated ordering temperatures for various DMS systems are discussed, and the usefulness of the method is demonstrated. Moreover, in order to include all the complexity in the fabrication process of DMSs into advanced materials design, spinodal decomposition in DMSs is simulated and we try to assess the effect of inhomogeneity in them. Finally, recent works on first-principles theory of transport properties of DMSs are reviewed. The discussion is mainly based on electronic structure theory within the local-density approximation to density-functional theory.

CONTENTS

I. INTRODUCTION

Dilute magnetic semiconductors (DMSs) are semi-conductors doped with magnetic impurities. Typical examples are Mn-doped II-VI compounds such as

(Cd,Mn)Te. So far, their magneto-optical properties have been investigated intensively. Since the discovery of carrier-induced ferromagnetism in Mn-doped InAs and GaAs, much effort has been devoted to the use of DMS systems as a foundation for semiconductor spintronics. The physical properties of DMSs continue to challenge our understanding of these materials. As a result several different models and mechanisms have been proposed to explain their magnetism. The field has attracted considerable attention over recent years, and there are now several thousands of papers being published annually on this topic. The reason is the hope that the manipulation of the electron spin in semiconducting devices will improve the conventional semiconductor technology. Hence it has been suggested that DMS materials will be the building blocks of novel technologies for nonvolatile memories, devices with increased data processing speed and decreased power consumption, and possibly smaller structures (Prinz, 1998; Wolf *et al.*, 2001; Jungwirth *et al.*, 2005, 2006; MacDonald *et al.*, 2005).

Since the general ambition is to use materials and devices at room temperature, one of the primary goals in the research into DMS materials is to develop a ferromagnetic semiconductor with an ordering temperature well above room temperature. The avenue that has been pursued most intensively is to dope regular III-V or II-VI semiconductors with a magnetic element, such as Mn or Co. In general, the magnetic ($3d$) atoms in DMS materials are located on substitutional and/or interstitial sites of the semiconducting host, and most attention has been focused on III-V and II-VI semiconductors, where the underlying lattice has wurtzite or zinc-blende structure. An important fact is that for II-VI semiconductors a larger concentration of $3d$ elements can be substituted in the semiconducting lattice: up to $\sim$35% magnetic atoms can be absorbed, which should be compared to $\sim$8% for III-V semiconductors. Several DMS materials have been predicted to have ordering temperatures above room temperature, for example, Mn-doped GaN (Bonanni, 2007) and Co-doped TiO_2 as well as Mn-doped ZnO (Pearton *et al.*, 2004). However, no experimental report on DMS materials with an ordering temperature above room temperature has been left unchallenged by other studies, where a much lower ordering temperature or even absence of magnetic ordering is reported. The large difference in ordering temperatures reported by different experimental groups is normally attributed to difficulties in sample handling. The differences may also be caused by clustering of the doped $3d$ elements on the semiconducting host lattice or concentration differences of other defects.

Hence, one of the main experimental challenges is to synthesize materials that are well characterized with respect to the distribution of magnetic atoms (of $3d$ elements) on the semiconducting host lattice. In addition one requires a good control of other defects in the material. An example of this is provided by one of the earliest findings by Ohno (1998), who found Mn-doped GaAs to be ferromagnetic with an ordering temperature
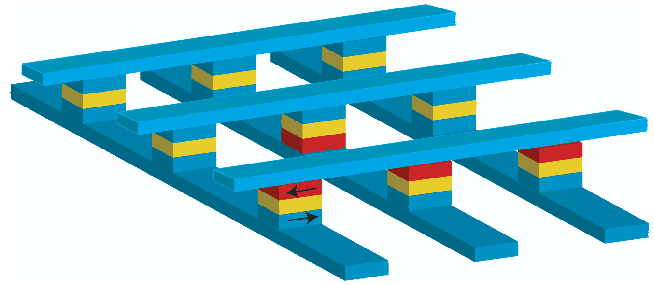

FIG. 1. (Color online) Schematic illustrating the MRAM device. Each magnetic pillar consists of three layers; two magnetic layers (depending on the magnetization direction of these layers) are separated by a nonmagnetic layer, yielding a structure with a regular GMR functionality. The binary code is stored as the coupling between the two magnetic layers in a pillar and it is read via the magnetoresistive property of the pillar (see text).

of 110 K. Subsequent studies of the same system resulted in a higher ordering temperature, 170 K (Edmonds *et al.*, 2002a), and most of the difference from the earlier results was attributed to the fact that interstitial Mn atoms and As antisite defects were removed by annealing.

Historically the field of spintronics can be said to have begun with the discovery of the giant magnetoresistance (GMR) effect and the interlayer exchange coupling in metallic multilayers by Grünberg and Fert (Baibich *et al.*, 1988; Binasch *et al.*, 1989). They were awarded the Nobel prize in physics in 2007 for their work in this field. The important aspect of a GMR device is that its conductance depends strongly on an applied magnetic field, which switches the coupling between magnetic layers. At low temperatures the GMR effect, i.e., the field-induced change in resistance, is typically on the order of 10% in metallic systems, but in multilayers up to 100% has been measured. A theoretical explanation for the interlayer exchange coupling was provided by Bruno and Chappert (1991); several explanations for the GMR effect have been provided with different levels of sophistication. Reviews of the GMR effect can be found in Gijs and Bauer (1997) and Thompson (2008). It should be noted that the GMR effect has been applied further, involving also insulating magnetic layers in the device; this is called tunneling magnetoresistance (TMR) and can result in a much enhanced magnetoresistance, increased by upto 400% at room temperature (Yuasa *et al.*, 2006).

Man-made materials exhibiting GMR or TMR have been shown to be useful for magnetic sensors, and manufacturers of disk drives and hard disks use the magnetoresistance effect in the so-called read head. Another application of the GMR or TMR effect is shown in Fig. 1, where we display schematically the idea behind the magnetic random access memory (MRAM). Commercial products that build on the nonvolatile MRAM technology are already available on the market. A MRAM stores a binary code (a 1 or a 0) utilizing the possibility of aligning magnetic layers ferromagnetically (which
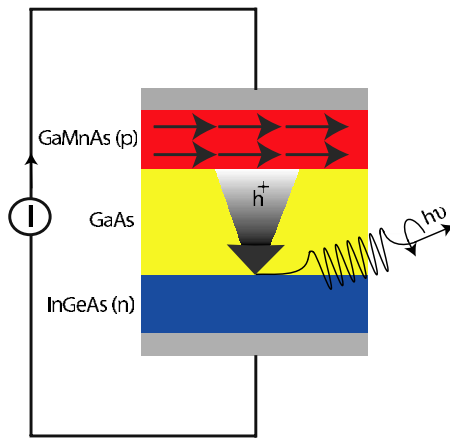
FIG. 2. (Color online) Spin-polarized light-emitting diode. Spin-polarized holes of the Mn-GaAs region recombine with electrons in the InGaAs region, with emission of circularly polarized light.

FIG. 3. (Color online) Predicted ordering temperatures of Mn-doped DMS materials. The concentration of Mn atoms is 5%. From Dietl *et al.*, 2000.

may represent a 1) or antiferromagnetically (which may represent a 0). An antiferromagnetic alignment between two magnetic films in the pillar will have a different resistance compared to a ferromagnetic alignment due to the GMR effect, and the resistance of a pillar will reveal if a 1 or 0 has been stored. It is simple to read the information by measurement of the resistance of any given pillar. Writing of information involves a change in the coupling between the two magnetic layers in a given pillar, from antiparallel to parallel or vice versa, and is typically done via an Oersted field generated when current flows in the leads connecting the pillars.

A second example of a spintronics device is the spin-polarized light-emitting diode (SPLED) shown in Fig. 2. Unlike the example shown in Fig. 1, the SPLED actually utilizes a dilute magnetic semiconducting material, and it has a demonstrated functionality at low temperatures. In this device a region of Mn-doped GaAs is found to order at low temperatures. Mn doping is accompanied by holes (*p*-type doping) in the valence band which couple their spins to the moments of the Mn atoms, producing spin-polarized carriers. An *n*-type-doped region is separated from the *p*-type-doped region by a GaAs layer. When a voltage is applied, spin-polarized holes of the *p*-type region travel over the GaAs layer to recombine with electrons in the *n*-type region. Since the holes are spin polarized, the light emitted in the recombination process has a specific helicity in order to conserve angular momentum. Hence, the fact that the device shown in Fig. 2 has been demonstrated to emit circularly polarized light proves that the holes in the Mn-doped GaAs layer are spin polarized (Ohno *et al.*, 1999). The device shown in Fig. 2 operates so far only at low temperatures and is not available commercially.

This review has outlined general principles of spintronics and we have given a few examples of functional devices. Further examples may be found, in Žutić *et al.* (2004). Now we focus our attention on the main issue of this review; the nature of the magnetism and the interatomic exchange interaction in dilute magnetic semiconductors. The nature of the exchange interactions in semiconductors was analyzed by Anderson (1963). Subsequent studies of DMS materials focused on model Hamiltonians that have been suggested to describe the magnetism in these systems. Among the most frequently quoted is the work of Dietl *et al.* (2000), where Zener's theory for ferromagnetism, in particular, the so-called *p*-*d* exchange, was used. This theory considers a coupling between carrier spins and local atomic moments of magnetic impurities and in parallel to mean-field theory provides an estimate of the ordering temperatures of several DMS materials (Dietl *et al.*, 2000). The theory has predicted several systems with potential for large ordering temperatures (for example, ZnO and GaN). We show as an example in Fig. 3 the calculated ordering temperatures of DMS systems as analyzed by Dietl *et al.* (2000). We also mention that these and similar ideas of DMS materials have been reviewed by Jungwirth *et al.* (2005) and MacDonald *et al.* (2005). It will be shown in the following that ordering temperatures found within Zener's *p*-*d* mean-field theory are strongly overestimated because neither thermal fluctuations nor disorder effects (percolation), which can drastically reduce the Curie temperature, are properly treated.

More precise calculations based on density-functional theory (DFT) have also been performed for magnetic semiconductors. For instance, the electronic structure and calculated size of the magnetic moments of 3*d* impurities in semiconductors were reviewed by Zunger (1986). Analysis of the magnetism and exchange interaction of DMS materials took a great leap forward with the invention of materials-specific calculations using DFT. In particular, the implementation of the local force theorem (Andersen *et al.*, 1980) for magnetic exchange (Oswald *et al.*, 1985; Liechtenstein *et al.*, 1987) has proven useful for obtaining information about the interatomic exchange interactions. At an early stage these methods gave valuable information concerning the nature of the magnetic state, for example, ferromagnetic or spin-glass-like (or disordered local moment) in Mn-doped InAs (Akai, 1998) and GaAs (Korzhavyi *et al.*,

2002), and in addition they revealed the existence of a coupling between magnetism and defect concentration.

In the traditional picture of exchange interaction in DMS materials, the exchange interaction is long ranged and has no angular component [the work of Dietl *et al.* (2000) is consistent with this range of exchange interaction], whereas the exchange interaction suggested by DFT is much more short ranged and reflects the orbital character of the atoms building up the lattice. The short-ranged nature of the exchange interaction suggests that the magnetic properties of DMS materials are influenced by magnetic percolation. In fact, calculated interatomic exchange interactions have been used to estimate the ordering temperature of these materials (Bergqvist *et al.*, 2004; Fukushima *et al.*, 2004; Sato, Schweika, *et al.*, 2004), and it was found that, once the traditional mean-field description was abandoned, the calculated Curie temperature decreased, and good agreement between theory and observations could be obtained. These methods have also provided an understanding of the nature of the exchange interaction in these materials. Hence different microscopic mechanisms behind the interatomic exchange have been discussed, for example, the *p-d* exchange and, Zener's superexchange and double-exchange mechanisms. It is, however, important to realize that the results from DFT depend on the quality of the effective potential; we review results from different approximations for this potential and how the choice of effective potential influences the calculated properties.

In this article, we review the results of theoretical calculations based on density-functional theory of DMSs. We discuss, in particular, the central problem for dilute ferromagnetic semiconductors. Do DMSs with Curie temperature T_C well above room temperature exist, such that realistic applications are feasible? The hope for high-T_C values was raised by Dietl *et al.* (2000). However, this hope does not seem yet to be supported from *ab initio* theory.

We begin by discussing the hybridization of the transition-metal (TM) *d* states with the valence band *p* states. We also discuss multiple charge states of TM impurities and correlation effects due to screening. Calculations for lattice relaxations are reviewed; at least for the well-known (Ga,Mn)As system, analysis shows that they are not important in real technological applications. Then we discuss the electronic structure of concentrated DMSs by applying the coherent potential approximation. Within this mean-field treatment of the electronic structure, the energetic stability of the ferromagnetic state versus the disordered local moment (DLM) state is demonstrated to show clear trends which enable a deeper understanding of the relevant exchange mechanisms of DMS.

We also analyze asymptotically the relation between the exchange coupling constants and the Curie temperature. These coupling constants show an exponential decrease with distance, superimposed on an oscillatory Ruderman-Kittel-Kasuya-Yosida (RKKY) type of behavior. The exponential decrease is to a large extent the result of the half-metallic behavior of DMSs, i.e., the band gap in the minority band, and is particularly important for wide-band-gap semiconductors, for which the interaction is very short ranged. Additional damping arises for larger concentrations of impurities and larger distances between them, from the impurity-impurity scattering. Somewhat longer-ranged interactions occur only for relatively narrow band gaps, in particular, for GaAs and GaSb.

Simple models for the understanding of the exchange mechanisms are also reviewed. Double exchange is the dominating mechanism for ferromagnetism in wide-band-gap semiconductors such as GaN or ZnO. Here the atomic *p* levels of N and O are very low in energy, leading to deep-lying *p* valence bands and a large band gap. For the same reason the transition-metal *d* states form impurity bands in the gap, which determine the magnetic interactions. Therefore double exchange is very strong and short ranged. The opposite behavior occurs for relatively narrowband DMSs such as (Ga,Mn)As and (Ga,Mn)Sb. Here the atomic *p* levels are higher in energy, leading, on the one hand, to narrower band gaps and, on the other hand, to the centering of the majority *d* state of Mn in the lower region of the valence *p* band. This leads to increased importance of Zener's *p-d* exchange, which is relatively weak but longer ranged. We show that the normal and dominating mechanism for ferromagnetism in DMSs is double exchange.

Superexchange is argued to be the dominant antiferromagnetic interaction, leading to the disordered local moment phase of DMSs. It is also rather strong and essentially restricted to nearest neighbors. It is largest when the Fermi level falls in the gap between the majority and minority impurities. If E_F lies in an impurity band, it competes with the ferromagnetic double exchange.

It is furthermore shown how the Curie temperature T_C can be calculated by the local random-phase approximation (LRPA) and by the Monte Carlo (MC) method. An important finding of recent research on DMSs is that the mean-field approximation overestimates the Curie temperature of dilute systems since the magnetic behavior is dominated by the percolation problem; we review the details of this finding. We also discuss results for some other DMS systems, for example, the wide-gap semiconductor SiO_2 doped with transition metals. The ferromagnetism in these systems [$(Si,V)O_2$ and $(Si,Mn)O_2$] is caused by double exchange. Another example is the semiconductor $CuAlO_2$ doped with TM impurities on the Cu and the Al sublattices. In both systems the magnetism is due to narrow impurity bands in the gap and ferromagnetism is caused by double exchange. For a concentration of 20% of TM impurities, the largest T_C obtained in these calculations is 100 K for $Cu(Al,Mn)O_2$. We also discuss DMSs based on semiconducting Heusler alloys. Here we consider the nonmagnetic half-Heusler alloys CoTiSb and NiTiSn, all doped with 5% Mn. Strong ferromagnetism due to double exchange is found; however, the coupling con-

stants are large only for the first neighbors. Thus a high Curie temperature cannot be obtained in the dilute limit; rather a Mn concentration of 25% [in Ni (Ti,Mn)Sn] or 30% [in Co (Ti,Mn)Sb] is necessary for a Curie temperature around room temperature.

We also review in this article recent attempts to enhance the ordering temperature by considering inhomogeneous phases, driven by, for example, spinodal decomposition, where locally one may obtain higher concentrations of magnetic impurities. Kinetic Monte Carlo simulations based on *ab initio* potentials for the interaction reveal that by three-dimensional (3D) decomposition large nonoverlapping clusters are formed, which show a superparamagnetic behavior with a relatively high blocking temperature. For higher concentrations (above 20%) a 3D network of percolating clusters with substantially increased Curie temperature can be obtained, which holds promise for realizing DMS materials for spintronics technology.

State of the art calculations of the residual resistivity of DMSs are also reviewed here. The method used is the Kubo-Greenwood linear response formalism. It is shown that this method gives excellent results for (Ga,Mn)As despite the large number of defects and the nearly insulating behavior. The calculations also show that the transport is totally dominated by the majority band and that vertex corrections are of minor importance. The experimentally observed nearly linear relation between Curie temperature and conductivity is found in these calculations, provided compensating defects are considered.

We end our article by an outlook to the future of DMS materials and try to identify areas where most exciting new research on these materials is likely to appear.

II. 3*d* TRANSITION-METAL IMPURITIES IN SEMICONDUCTORS

A. Self-consistent *ab initio* theory of the electronic structure

Since we use the density-functional theory (Hohenberg and Kohn, 1964; Kohn and Sham, 1965) as a working tool, we give an introduction to it. In its simplest form for spin-polarized (magnetic) materials, one arrives at an energy functional, which depends both on the majority and on the minority spin densities [or total density $n(\mathbf{r}) = n^\uparrow(\mathbf{r}) + n^\downarrow(\mathbf{r})$ and magnetization density $m(\mathbf{r}) = n^\uparrow(\mathbf{r}) - n^\downarrow(\mathbf{r})$].[1] The Kohn-Sham scheme attempts to calculate this functional from an effective one-electron theory, where the majority and minority electrons move in an effective potential that is constructed to generate the ground-state density for these electrons. This theory is a practical way of calculating charge and magnetization

densities, and in addition it is possible to write down an expression for the total energy of the system,

$$E[n^\uparrow(\mathbf{r}), n^\downarrow(\mathbf{r})] = T_{op}[n^\uparrow(\mathbf{r}), n^\downarrow(\mathbf{r})] + \int n(\mathbf{r})v(\mathbf{r})d^3r$$
$$+ \frac{1}{2}\int\int e^2 \frac{n(\mathbf{r}) \cdot n(\mathbf{r}')}{|\mathbf{r} - \mathbf{r}'|}d^3r d^3r'$$
$$+ E_{xc}[n^\uparrow(\mathbf{r}), n^\downarrow(\mathbf{r})]. \tag{1}$$

Here $T_{op}[n^\uparrow(\mathbf{r}), n^\downarrow(\mathbf{r})]$ is the kinetic energy of one-particle (or independent) electrons, the second term contains interactions between the electrons and an external potential, like the one given by a nucleus, and the third term is the classical Hartree interaction. The last term, the exchange-correlation energy, for which useful parametrizations as functions of $n^\uparrow(\mathbf{r})$ and $n^\downarrow(\mathbf{r})$ exist (Ceperley and Alder, 1980), is defined as the difference between the true (unknown) energy functional and the three first terms on the right-hand side of Eq. (1).

The Kohn-Sham equation with spin-up (-down) effective potentials

$$[-\nabla^2/2 + V_{eff}^{\uparrow(\downarrow)}]\psi_i^{\uparrow(\downarrow)} = E_i^{\uparrow(\downarrow)}\psi_i^{\uparrow(\downarrow)} \tag{2}$$

determines the one-particle wave functions from which the majority and minority spin densities can be calculated as

$$n_{op}^{\uparrow(\downarrow)}(\mathbf{r}) = \sum_{i=1} |\psi_i^{\uparrow(\downarrow)}(\mathbf{r})|^2. \tag{3}$$

The effective potentials in Eq. (2) are different for the two spin directions due to differences in the exchange-correlation potential,

$$V_{eff}^{\uparrow(\downarrow)}(\mathbf{r}) = v(\mathbf{r}) + \int e^2 \frac{n(\mathbf{r}')}{|\mathbf{r} - \mathbf{r}'|}d^3r' + \mu_{xc}^{\uparrow(\downarrow)}(\mathbf{r}), \tag{4}$$

where $\mu_{xc}^{\uparrow(\downarrow)}(\mathbf{r}) = dE_{xc}/dn^{\uparrow(\downarrow)}$.

Hence the simplest form of spin-polarized calculation treats spin-up and -down electrons separately in the Kohn-Sham equation. Spin-up and -down densities are then calculated by occupation of the lowest (spin-up or -down) eigenvalues of the two separate Kohn-Sham equations. Since a given $V_{eff}^\uparrow(\mathbf{r})$, which may be different from $V_{eff}^\downarrow(\mathbf{r})$, may lead to more occupied (below Fermi level E_F) spin-up states $n_i^\uparrow$ than spin-down states $n_i^\downarrow$, spin polarization can occur. With a self-consistent spin and magnetization density the magnetic moment is calculated as $\int m(\mathbf{r})d^3r$ (in Bohr magneton units) and the total energy may be calculated from Eq. (1).

For practical reasons it is sometimes advantageous to calculate the Green's function of the material instead of the eigenvalues E_i and wave functions ψ_i, especially when one attempts to calculate in disordered systems or the interatomic exchange interactions, described below. The Green's function is defined by

$$(-\nabla^2/2 + V_{eff} - E - i\epsilon)G(\mathbf{r}, \mathbf{r}'; E) = \delta(\mathbf{r} - \mathbf{r}'), \tag{5}$$

where for simplicity we have suppressed the spin indices. In operator notation this reads

---

[1]We note here that this approach has simplified the situation since the magnetization density is a scalar property with both magnitude and spin. In this analysis we are assuming that the magnetization is collinear, i.e., parallel or antiparallel to the z direction of the system.

$$G = \frac{1}{E + i\epsilon - h_{\text{eff}}} \quad \text{with } h_{\text{eff}} = -\frac{\nabla^2}{2} + V_{\text{eff}}(\mathbf{r}), \quad (6)$$

where $i\epsilon$ denotes causality. The Green's function describes the propagation of electrons that have energy E and are produced at position r in a medium described by V_{eff}. Once G is known, all single-particle properties needed to perform self-consistent calculations can be calculated. For instance, the spin densities are given by

$$n^{\uparrow(\downarrow)}(\mathbf{r}) = -\frac{1}{\pi} \text{Im} \int^{E_F} dE \, G^{\uparrow(\downarrow)}(\mathbf{r},\mathbf{r};E). \quad (7)$$

It should be noted that for most electronic structure calculations the effective potential of Eq. (2) is calculated using the local density approximation (LDA), the local spin-density approximation (LSDA), or the generalized gradient approximation (GGA) (Perdew and Wang, 1986; Dreizler and Gross, 1995). Unfortunately these approximations are not always sufficient for reproducing the electronic structure of a given material; for DMSs this is one of the important questions for which we do not have a clear answer. In order to improve on this approximation a mean-field treatment of the Coulomb repulsion of electrons situated on the same atom has been suggested. There are several methods for doing this. In this review we consider only the so-called LDA+U approximation (Anisimov *et al.*, 1997). We end this section by remarking that the calculations reviewed are scalar relativistic and omit spin-orbit interaction.

1. Coherent potential approximation for alloy calculations

In the study of ferromagnetism in DMSs we are interested in magnetic exchange coupling between TM impurities; therefore electronic structure calculations at finite impurity concentrations are needed. Moreover, in DMSs TM impurities substitute at cation sites of the host semiconductors randomly; thus we have to consider substitutional disorder in a realistic way. One of the most efficient methods for this purpose is the coherent potential approximation (CPA) (Shiba, 1971). The CPA accurately describes the configuration average of the electronic structure of disordered systems. This method is conveniently used to calculate averaged properties of substitutional alloys and magnetically disordered systems (Akai and Dederichs, 1993).

In the CPA method, an effective CPA medium describes the configuration average of the disordered system (Velický *et al.*, 1968; Faulkner and Stocks, 1980). In the framework of multiple-scattering theory, the electronic structure of the whole system is constructed from single-site properties, which are described by the so-called atomic t matrices that describe all repeated scattering events at one and the same atom. For the CPA medium we consider a hypothetical atom whose atomic t matrix is written as t_{CPA}, which is evaluated in a mean-field procedure. For example, in case of a two-component alloy $A_{1-x}B_x$, where x is the concentration of B atoms, the scattering path operator τ calculated

from t_{CPA} should be equal to the weighted average of τ_A and τ_B, i.e., $\tau = (1-x)\tau_A + x\tau_B$, where τ_A and τ_B are the scattering path operators calculated for single A and B impurities in the effective CPA medium. This equation is solved iteratively for a self-consistent t_{CPA}. Normally, τ_A and τ_B are calculated within the single-site approximation and local environment effects are neglected. The CPA method should be contrasted with the virtual crystal approximation (VCA) where for an electronic structure calculation of an alloy composed of two neighboring atoms in the periodic table, one simply considers an average atom with a nuclear charge in Eq. (2), which is an average of the nuclear charges of the two atomic species of the alloy. The VCA method has severe limitations and is often used only for alloys composed of neighboring elements of the periodic table.

As described above, the CPA method is formulated within the framework of multiple-scattering theory; therefore it can be efficiently combined with the Green's function method for electronic structure calculations. So far, the Korringa-Kohn-Rostoker (KKR) method (Akai, 1989) and the linear muffin-tin orbital (LMTO) method (Turek *et al.*, 1997) have been combined with the CPA and applied successfully to magnetic alloy systems and, in particular, DMSs. Compared to the supercell approach, utilizing standard electronic structure packages, which is frequently used to model impurities, defects, and alloys, the CPA method can be much more powerful for systematic materials design because of its calculational speed and ability to deal with arbitrary concentrations. However, due to the single-site approximation in the CPA, short-range order of the impurities and local environment effects cannot be described. In this article, most of the results presented are obtained from KKR-CPA and LMTO-CPA calculations. Detailed descriptions of the methods and numerical techniques can be found in Shiba (1971), Akai (1989), Akai and Dederichs (1993), and Turek *et al.* (1997).

2. Disordered local moment picture

One of the most important properties of a ferromagnet is the Curie temperature, above which the system becomes paramagnetic. An estimation of the Curie temperature can be obtained from the total energy difference between the ferromagnetic and paramagnetic states (Sato *et al.*, 2003; Sato, Schweika, *et al.*, 2004). In the paramagnetic state the direction of local moments is random, resulting in zero global magnetization. This magnetic disorder is conveniently treated by the concept of a DLM state (Oguchi *et al.*, 1983; Gyorffy *et al.*, 1985; Staunton *et al.*, 1985). In the DLM state, we consider two components for one magnetic atom, with opposite magnetization directions but chemically equivalent. In the case of (Ga,Mn)As, for example, the ferromagnetic state is described as $\text{Ga}_{1-x}\text{Mn}_x^{\uparrow}\text{As}$ and the DLM state is described as $\text{Ga}_{1-x}\text{Mn}_{x/2}^{\uparrow}\text{Mn}_{x/2}^{\downarrow}\text{As}$. Since the up and down components have the same concentration, the total moment vanishes. It is known that the DLM state describes the paramagnetic state of ferromagnets reasonably well
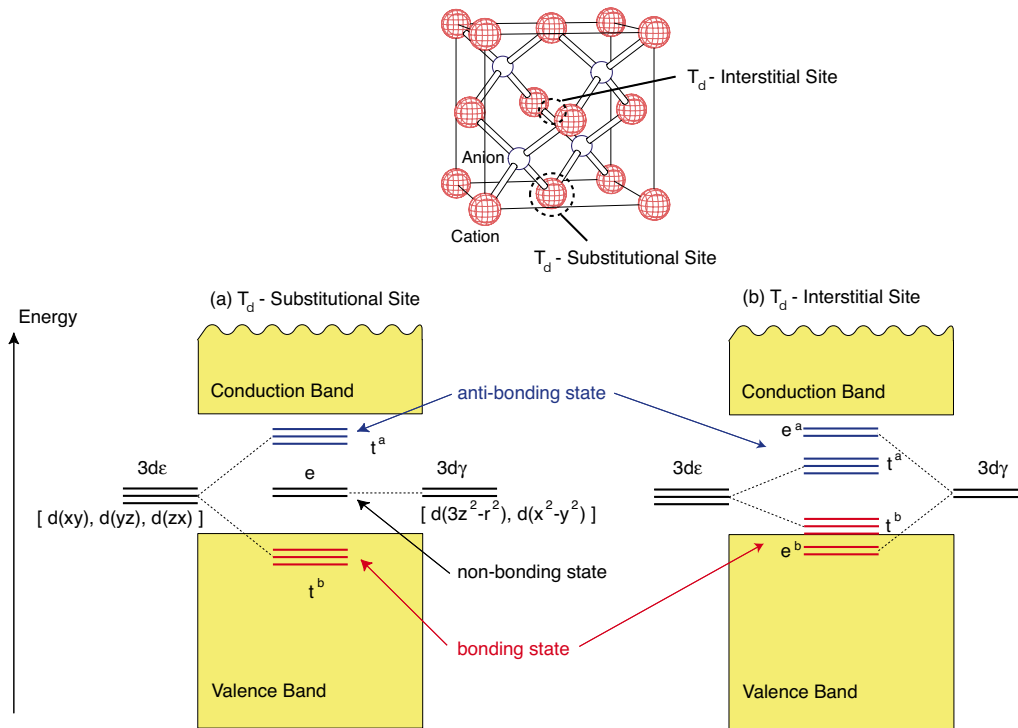
FIG. 4. (Color online) Schematic of the electronic structure of $3d$ TM impurities in semiconductors at (a) the tetrahedral (T_d) substitutional site and (b) the tetrahedral (T_d) interstitial site.

(Oguchi *et al.*, 1983; Gyorffy *et al.*, 1985; Staunton *et al.*, 1985). In Sec. IV we analyze the Curie temperature and its coupling to the energy difference between ferromagnetic and DLM states.

B. Dilute limit

1. Electronic structure of 3*d*-TM impurities in semiconductors

We begin our review of the electronic structure and magnetism of DMSs by considering the electronic structure of a $3d$-TM impurity in semiconductors. At the T_d substitutional site (with an environment of tetrahedral symmetry T_d), a $3d\epsilon(xy,yz,zx)$ orbital hybridizes strongly with the ligand s and p orbitals (p-d hybridization) and forms the bonding (t_b) state in the valence band, whereas the antibonding state (t_a) is pushed up into the band gap. However, a $3d\gamma(x^2-y^2,3z^2-r^2)$ orbital forms a highly localized nonbonding (e) state due to the small p-d hybridization (Zunger, 1986; Katayama-Yoshida, 1987; Sato and Katayama-Yoshida, 2001a, 2002; Mahadevan and Zunger, 2004). This usually leads to a high-spin ground state, where the exchange splitting is larger than the crystal field splitting. Unlike the $3d$-TM impurity at the substitutional site, both $d\epsilon$ and $d\gamma$ states at the interstitial site can hybridize strongly with the ligand s and p orbitals. At the T_d interstitial site, the p-d hybridization of the $3d\gamma$ orbital with an octahedrally coordinated second-nearest-neighbor p orbital is much stronger than that of the $3d\epsilon$ orbital with the tetrahedrally coordinated first-nearest-neighbor p orbital because of the larger coordination number. Therefore, the

t_a and e_a level ordering at the tetrahedral (T_d) substitutional site is reversed at the tetrahedral (T_d) interstitial site (see Fig. 4), leading to a completely different level sequence.

2. Multiple charged states and negative-*U* system of 3*d*-TM impurities in semiconductors

The size of the band gap in semiconductors is a few eV, and one can change the chemical potential from the maximum of the valence band to the minimum of the conduction band by acceptor or donor doping. Hence, one can find multiple charged states (for example, Mn^{2+}, Mn^+, Mn^0, Mn^-, and Mn^{2-}) of $3d$-TM impurity-doped semiconductors by changes in the chemical potential upon acceptor or donor co-doping (Zunger, 1986; Katayama-Yoshida, 1987). The microscopic origin of the multiple charged states is the strong intra-atomic Coulomb repulsion (U) of the $3d$-TM impurity and the strong p-d hybridization between the $3d$-TM impurity and ligand s and p orbitals (see Fig. 5). A change in the electron chemical potential by doping can therefore change the charge state of a $3d$-TM impurity in a semiconductor. This Coulomb interaction can be calculated as $U_0 = E(N+1) + E(N-1) - 2E(N)$, where $E(N)$ is the total energy of the N-electron system. For atoms this interaction can be as large as 20 eV. In a semiconductor, however, the effective intra-atomic Coulomb repulsion $U_{\text{eff}} = E(N+1) + E(N-1) - 2E(N)$ of the $3d$-TM impurity can be reduced by two orders of magnitude, resulting in values on the order of 0.2–0.5 eV (Haldane and Anderson, 1976; Katayama-Yoshida and Zunger, 1984, 1985a,
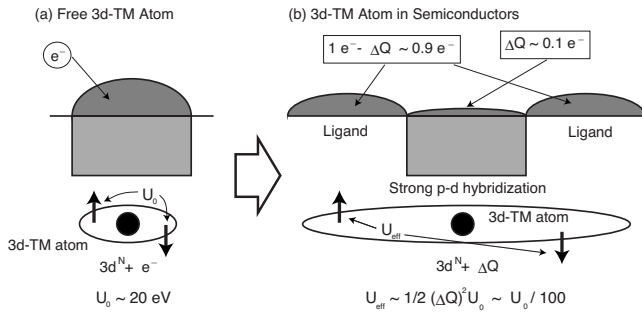
FIG. 5. Schematic explanation of the microscopic mechanism of the reduction of intra-atomic Coulomb repulsion (U_0) of a 3d TM impurity (3d^N) in semiconductors (Haldane and Anderson, 1976). (a) In the free 3d TM atoms the additionally attached electron (e^-) leads to a large $U_0 \sim 20$ eV due to the strong localization at the 3d atomic orbital. (b) In the semiconductor, due to the repulsive Coulomb interaction and the strong p-d hybridization, the additional electron is delocalized; 90% of the charge is located in extended impurity band states at the ligand sites and only 10% (ΔQ) is localized on the 3d TM atomic site. This is called the Haldane-Anderson mechanism and reduces the effective intra-atomic Coulomb interaction (U_{eff}) by almost two orders of magnitude.

1985b, 1985c, 1986) [see Zunger (1986) and Katayama-Yoshida (1987)], and it is possible to stabilize the multiple charged states by co-doping with acceptor or donor impurities. Multiple charged states arise because the effective U_{eff} is reduced by almost two orders of magnitude. In experiments by deep-level transient spectroscopy (DLTS) or electron paramagnetic resonance (EPR), multiple charged states are observed in the band gap when acceptor or donor doping changes the chemical potential (Zunger, 1986; Katayama-Yoshida, 1987).

The microscopic origin of the multiple charged states was first explained by Haldane and Anderson using the Anderson model (Haldane and Anderson, 1976). Multiple charged states were then found in *ab initio* calculations by Katayama-Yoshida and Zunger (1984, 1985a, 1985b, 1985c, 1986), Beeler *et al.* (1985), Oshiyama *et al.* (1988), and others [see Zunger (1986) and Katayama-Yoshida (1987)]. A schematic explanation of the microscopic origin of the multiple charged states of a 3d-TM impurity (d^N) in semiconductors is given in Fig. 5. Because of the repulsive Coulomb interaction and the strong p-d hybridization, electrons added to the deep-impurity states are delocalized through the crystal. Then, it may happen that 90% of the charge ($1 - \Delta Q$) added by co-doping is located in extended impurity band states at the ligand sites and the remaining 10% (ΔQ) is localized on the 3d-TM atomic site. This Haldane-Anderson mechanism (Haldane and Anderson, 1976) reduces the effective intra-atomic Coulomb interaction (U_{eff}) by almost two orders of magnitude because $U_{\mathrm{eff}} \propto (\Delta Q)^2 U_0 \sim U_0/100$ (Haldane and Anderson, 1976; Katayama-Yoshida and Zunger, 1984, 1985a, 1985b, 1985c, 1986; Zunger, 1986; Katayama-Yoshida, 1987; Oshiyama *et al.*, 1988). We say that the charge of the 3d-TM impurity in a semiconductor is well screened by
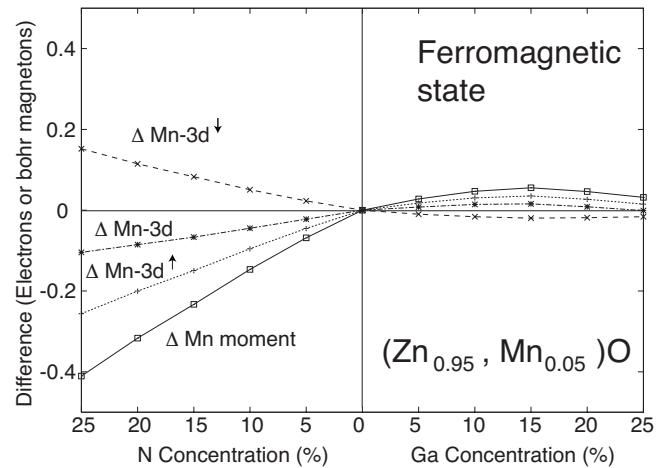

FIG. 6. Change in the doping dependence of the magnetic moment (ΔM) and number of 3d electrons (ΔMn 3d) in (Zn, Mn)O. Upon hole (acceptor) doping by N, the number of 3d electrons with up-spin states (ΔMn 3$d^\uparrow$) decreases; on the other hand, (ΔMn 3$d^\downarrow$) with down-spin states increase. Thus the change in the total 3d TM charge, both up and down spin, upon hole doping is only 10% of the change in the total charge, and the remaining 90% of the total charge must exist in extended impurity band states at the ligand sites. In contrast, the change in the magnetic moment ($\Delta M = \Delta$Mn 3$d^\uparrow - \Delta$Mn 3$d^\downarrow$) is very large, since the exchange-correlation interaction is not well screened by multipole screening.

covalent bonding. The reduction of the effective U_{eff} caused by the Haldane-Anderson mechanism is important and useful for future semiconductor spintronics applications because one can change the charge and spin states by controlling the electron chemical potential by co-doping or an applied electric field by a gate voltage.

A 3d-TM impurity in a semiconductor is carrying spin and charge at the same time. The charge-charge interaction is based on the direct Coulomb interaction, a long-ranged interaction which is screened by long-wavelength electrons (monopole screening). However, the spin-spin interaction is based on the exchange-correlation interaction, a short-ranged interaction which is screened by short-wavelength electrons (multipole screening) in semiconductors with a large dielectric constant. Thus, the charge and spin of 3d-TM impurity are screened differently in semiconductors with a large dielectric constant (Katayama-Yoshida and Zunger, 1985c; Katayama-Yoshida, 1987; Sato and Katayama-Yoshida, 2001b). The additional charge, for example, due to co-doping of N acceptors or Ga donors in Mn-doped ZnO, is screened well; however, the magnetic moment is poorly screened by carriers upon co-doping with acceptor or donor impurities (Katayama-Yoshida and Zunger, 1985c; Katayama-Yoshida, 1987; Sato and Katayama-Yoshida, 2001b).

As an example we can choose the (Zn,Mn)O system (Sato and Katayama-Yoshida, 2001c) co-doped with N acceptor or Ga donor states. The change in doping dependence of the magnetic moment (ΔM) and number of 3d electrons (ΔMn 3d) is shown in Fig. 6. Upon hole

(acceptor) doping by nitrogen (N), the number of $3d$ electrons with up-spin states (ΔMn $3d^{\uparrow}$) decreases and stabilizes ferromagnetism; on the other hand, the number of $3d$ electrons with down-spin states (ΔMn $3d^{\downarrow}$) increases. Therefore, the total change in the $3d$-TM impurity charge upon hole doping is only 10% of the change in the total charge, and the remaining 90% of the total charge (hole) is located in the delocalized valence band. Unlike the change in the total charge, the change in the magnetic moment (spin) ($\Delta M = \Delta$Mn $3d^{\uparrow} - \Delta$Mn $3d^{\downarrow}$) of the $3d$-TM impurity is large and drastic since the exchange-correlation interaction is not well screened by multipole screening of electrons. In contrast to the hole doping, electron doping by Ga does not influence the number of $3d$ electrons and the magnetic moment of Mn, because the introduced electrons mainly occupy the host conduction bands, which consist of Zn-$4s$ states. It is energetically too expensive for the doped electrons to occupy the minority d states of Mn.

Since the effective U_{eff} is reduced by two orders of magnitude from the atomic U_0, the situation of a negative effective $U = E(N+1) + E(N-1) - 2E(N) \leqslant 0$ can occur. This is caused by exchange-correlation interaction (exchange-correlation-induced negative U) or by lattice relaxation due to the Jahn-Teller (JT) effect [Anderson's negative effective U (Anderson, 1975)]. We can decompose the correlation energy as $U = U_{\text{eff}} + \Delta U_{\text{JT}} + \Delta U_{\text{MC}}$, where the latter two contributions are due to JT and many-electron correction (MC) energies. ΔU_{MC} is caused by the exchange-correlation interaction (Katayama-Yoshida and Zunger, 1985c) combined with the Frank-Condon transition term reduced by the Haldane-Anderson mechanism. Since U_{eff} (0.2–0.5 eV) is much smaller than the value for the free atom (U_0), the negative ΔU_{JT} and ΔU_{MC} can overcome the positive U_{eff} and Anderson's negative-U systems (Anderson, 1975) or exchange-correlation-induced negative-U systems (Katayama-Yoshida and Zunger, 1985c) can be realized. If a negative effective U occurs for a d^N configuration of a $3d$-TM impurity in a semiconductor, the d^N configuration becomes unstable in thermal equilibrium and disproportionates into d^{N+1} and d^{N-1} configurations through the reaction $2d^N \rightarrow d^{N+1} + d^{N-1}$. Possible candidates for negative-U systems are d^4 and d^6 configurations (Katayama-Yoshida *et al.*, 2008). Missing oxidation states and charge disproportionation can be found for negative-effective-U systems such as (Ga, Mn)As, (Mg,Mn)O, and (Ca,Mn)O. While both Mn^{2+}(d^5) and Mn^{4+}(d^3) are observed, the Mn^{3+}(d^4) center is missing (Zunger, 1986; Katayama-Yoshida, 1987). It is also possible to use a negative-U system to realize the colossal magnetic response by photoexcitation or applied gate voltage for realistic semiconductor nanospintronics applications (Katayama-Yoshida *et al.*, 2007a).

3. Lattice relaxations around impurities

When an impurity is doped in a semiconductor, it usually occupies the cation site of the host. In some situa-

TABLE I. Magnetic moments (μ_B/cell) of $3d$ impurities (Cr–Ni) in GaAs calculated with and without atomic relaxations.

	Cr	Mn	Fe	Co	Ni
Unrelaxed	3.00	4.00	3.74	2.18	0.0
Relaxed	3.00	4.00	1.06	0.00	0.0

tions, the impurities can also be situated at interstitial sites. The effect of lattice relaxations due to substitutional doping of $3d$ transition-metal atoms in GaAs has been investigated by Mirbt *et al.* (2002). They showed with DFT calculations that early transition metals (Cr,Mn) introduce small relaxations around them, yielding a high-spin state, whereas Fe, Co, and Ni introduce strong relaxations, yielding a low- or zero-spin state. For the former case, the exchange splitting of the TM d states dominates over the tetrahedral crystal field produced by the host, whereas in the latter case the situation is reversed. The calculated magnetic moments of Mn-doped GaAs are listed in Table I for unrelaxed and relaxed systems. These can be qualitatively related to the energy level diagram shown in Fig. 4. However, as discussed above, one should keep in mind that this level diagram is rather schematic, whereas in reality the transition-metal d states hybridize with the host anion p states, and the result may differ substantially from this model. As discussed above and also shown in Table I, atomic relaxations reduce the moment, leading to a smaller exchange splitting for Fe and no splitting at all for Co and Ni. Cr and Mn impurities retain strong exchange splitting with a half-metallic DOS. Substitutional doping of Mn in a Ga site in GaAs and GaN causes a partial filling of the $t_{\uparrow}^a$ level (Fig. 4). Since only two of the three t_2 levels (xy, yz, and zx) are occupied, the system has a lower charge symmetry than T_d so that this configuration may give rise to a so-called Jahn-Teller distortion, leading to a structure with lower symmetry, depending on which two of the three orbitals are occupied. Luo and Martin (2005) investigated this possibility in Mn-doped GaAs and Mn-doped GaN systems with density-functional calculations. They considered three different lower-symmetry distortions, D_{2d}, C_{2v}, and C_{3v}, starting from the tetrahedral symmetry T_d of the pure host environment. The displacement of four nearest-neighbor N or As atoms around the Mn impurity can be decomposed into two parts. One part is a symmetric radial breathing component, which preserves the tetrahedral symmetry, and the other arises from symmetry-breaking Jahn-Teller distortions. A schematic diagram is shown in Fig. 7 where the breathing mode and lower-symmetry JT distortions are illustrated.

For a symmetry-preserving breathing mode, all four N nearest neighbors of the Mn atom in GaN move closer to the Mn by 0.034 Å and the energy decreases by 50 meV (Luo and Martin, 2005). For Mn-doped GaAs, all four As nearest neighbors move closer to Mn by only a small amount, 0.007 Å, and the energy decreases by 8 meV (Luo and Martin, 2005). No appreciable JT dis-
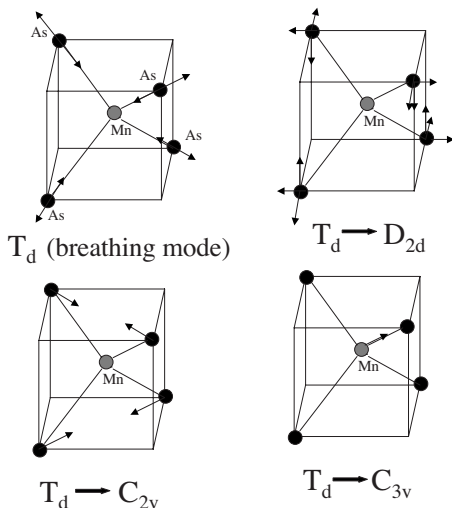
FIG. 7. Schematic showing the T_d symmetry-preserving breathing mode and other lower-symmetry JT distorted modes. The arrows indicate the direction of displacement of As atoms.

tortion was observed in GaAs. In contrast to that, the total energy of GaN was found to decrease by an amount of 0.1 eV with lowering of symmetry from T_d to D_{2d}. Lowering of symmetry to C_{2v}, where two neighbors of the Mn atom move along the [110] direction and two along the [$\bar{1}$10] direction, results in an energy decrease of 80 meV (Luo and Martin, 2005). Finally, a distortion toward C_{3v} symmetry results in an energy decrease of 20 meV only. One can conclude that a strong Jahn-Teller effect should be observed for low concentrations in Mn-doped GaN, but not in Mn-doped GaAs. The partial occupancy in the triplet t_2 state of Mn causes the JT distortion to the lower D_{2d} symmetry where the t_2 level splits into singlet and doublet states at the Γ point.

The density of states for Mn-doped GaN is shown without and with JT distortion in Figs. 8 and 9, respectively. The impurity band of Mn is more localized in GaN than in GaAs. Due to this difference, JT distortion has different effects on the impurity states. The splitting in the t_2 state is small in Mn-doped GaAs when the symmetry is changed from T_d to D_{2d}, whereas a relatively large splitting of 0.23 eV is observed for Mn-doped GaN. This can be observed in Fig. 9.
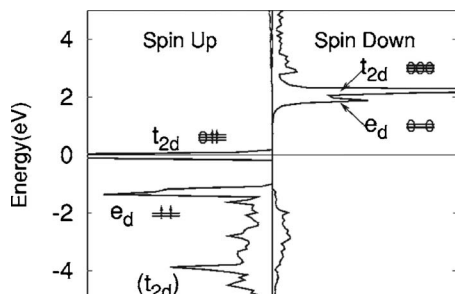
FIG. 8. DOS for Mn-doped GaN for an ideal structure with a tetrahedral T_d symmetry. From Luo and Martin, 2005.
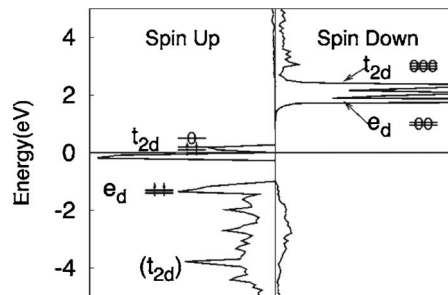
FIG. 9. DOS for Mn-doped GaN in a JT-distorted structure with D_{2d} symmetry. From Luo and Martin, 2005.

C. Typical electronic structure of DMSs

1. Electronic structure of III-V DMSs

The electronic structures of DMS based on III-V compounds calculated by the KKR-CPA method are shown in Fig. 10. As typical examples, we show the results for GaN- and GaAs-based DMSs. Mn-doped GaAs is the
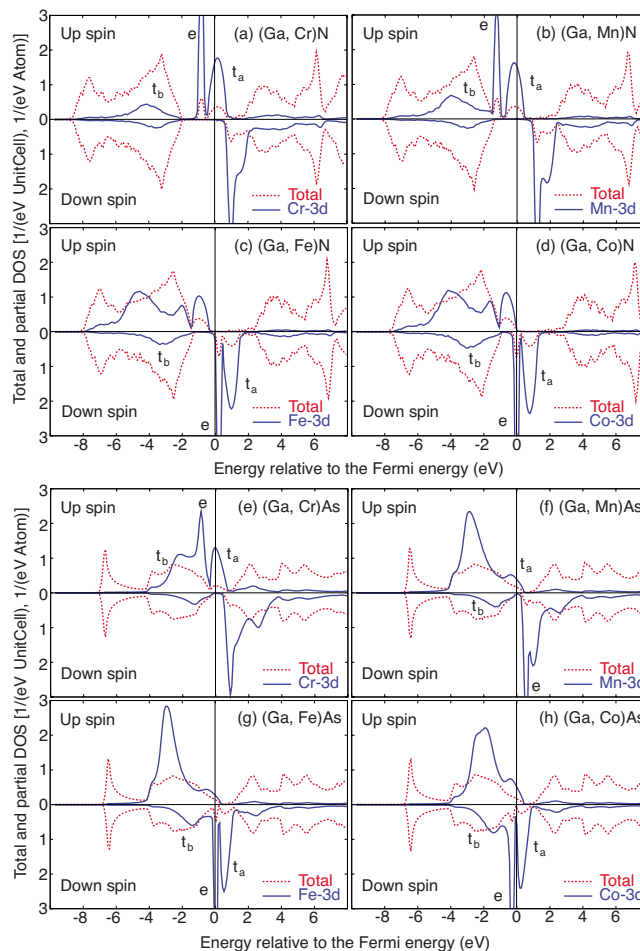
FIG. 10. (Color online) Calculated density of states of GaN-based (upper panels) and GaAs-based (lower panels) DMSs with $3d$ impurities ranging from Cr to Co. Dotted lines show total averaged DOS per unit cell and solid lines show partial DOS per atom of $3d$ components at TM sites. (Note the different scales.) A ferromagnetic configuration is assumed and the TM concentration is 5% for all cases.

most investigated DMS and its magnetic properties are well established experimentally. Mn-doped GaN has been investigated as a prototypical wide-band-gap DMS; however, its ferromagnetism has not yet been confirmed. In the figure, the concentration of TM impurities is 5% and a ferromagnetic configuration is assumed. For GaN and GaAs, the wurtzite and zinc-blende crystal structures with experimental lattice constants of the host compounds (Wyckoff, 1963) are assumed. As discussed in Sec. II.B.3, in some systems lattice relaxation is important in the dilute limit. In DMS systems magnetic impurities are usually doped up to high concentrations, where the band broadening of the impurity band due to randomness is always larger than the level splitting due to relaxation. Therefore, in the following discussion on ferromagnetism we neglect the lattice relaxation due to impurity doping.

Isolated TM impurities induce impurity states in the gap. The electronic structure for TM impurities under tetrahedral symmetry has already been discussed previously. Due to the finite concentration, these impurity states are broadened and form impurity bands as shown in Fig. 10. However, we can still distinguish characteristic structures in the calculated density of states (DOS) (Sato and Katayama-Yoshida, 2002). For example, in (Ga,Cr)N threefold-degenerate $d\epsilon$ states hybridize strongly with the host valence band states and form bonding t_b and antibonding t_a states. The t_b states are merged in the valence band and the t_a states appear as a broad peak in the gap. Between the t_b and t_a states, we recognize sharp e states, which have nonbonding character due to the incompatible symmetry of these states with the host valence states, as discussed in Sec. II.B.1. For the other systems, we distinguish similar structures in the calculated DOS. Due to the small coordination number at the tetrahedral site, the hybridization effect is relatively small, resulting in a high-spin configuration for all 3d TM impurities. A half-metallic or highly spin-polarized DOS at the Fermi level is obtained for all investigated DMSs, with the exception of (Ga,Fe)N, (Ga,V)As (insulating), and (Ga,Ni)As (nonmagnetic) (Sato and Katayama-Yoshida, 2002).

From Cr to Co, the TM d states are shifted gradually to lower energy and the impurity bands are occupied accordingly. The occupation of the impurity band might be estimated from a simple ionic picture. The Cr, Mn, Fe, and Co atoms have six, seven, eight, and nine valence electrons, respectively. When they substitute at a Ga site in GaN, three electrons are donated to make a bond with the N atom. The residual electrons occupy the impurity bands as discussed in Sec. II.B.1. From the discussion of this section we expect the following electronic configurations: $e_\uparrow^2 t_{a\uparrow}^1$, $e_\uparrow^2 t_{a\uparrow}^2$, $e_\uparrow^2 t_{a\uparrow}^3$, and $e_\uparrow^1 t_{a\downarrow}^0$ in Cr-, Mn-, Fe-, and Co-doped GaN, respectively, where the superscripts show electron populations and the arrows distinguish the spin directions. This estimate is easily confirmed in the calculated DOS [Figs. 10(a)–10(d)] of GaN-based DMSs (Sato and Katayama-Yoshida, 2002). As predicted from the ionic picture, in (Ga,Fe)N the impurity states with up spin are fully occupied and down-spin states are

TABLE II. Calculated total magnetic moment per TM impurity and local magnetic moment (in parentheses) at the TM site of III-V DMS systems. The concentration of TM impurity is 5%. FM and DLM indicate the ferromagnetic and disordered local moment states. A bold number indicates that the system has integer magnetic moment within numerical error, i.e., it is half metallic (except for insulating Fe-doped GaN).

	Cr	Mn	Fe	Co
GaN (FM)	**3.00** (2.33)	**4.01** (3.17)	**4.98** (3.58)	3.61 (2.48)
(DLM)	0 (2.26)	0 (3.10)	0 (3.51)	0 (2.46)
GaP (FM)	**3.01** (2.74)	**4.01** (3.48)	3.57 (2.85)	2.01 (1.52)
(DLM)	0 (2.70)	0 (3.44)	0 (2.92)	0 (1.43)
GaAs (FM)	**3.01** (2.97)	**4.01** (3.65)	3.63 (2.96)	2.02 (1.62)
(DLM)	0 (2.96)	0 (3.64)	0 (3.00)	0 (1.58)
GaSb (FM)	3.37 (3.42)	4.22 (3.85)	3.27 (2.90)	1.94 (1.61)
(DLM)	0 (3.43)	0 (3.85)	0 (2.91)	0 (1.58)

empty; thus the system is almost insulating. In (Ga,Cr)N and (Ga,Mn)N, ~1/3 and ~2/3 of the impurity t_a bands are occupied.

The electronic structure and crystal chemistry of the host semiconductor are also important for establishing a systematic understanding of the electronic structure and magnetism of DMSs. To illustrate this we compare two different semiconducting hosts, GaN and GaAs. In Figs. 10(e)–10(h), the calculated DOSs of GaAs-based DMSs are shown. Here the host valence bands are mainly formed by As 4p states, which are located at a higher energy position than the N 2p states. This difference changes the relative positions of the host valence p band and the impurity d bands and controls the strength of the hybridization. For example, in (Ga,Cr)N we can distinguish e and t_a bands as impurity bands in the gap [Fig. 10(a)]. However, in (Ga,Cr)As they are almost merged with the valence bands [Fig. 10(e)]. We can still distinguish t_b, e, and t_a peaks in the DOS of (Ga,Cr)As; however, due to the broadening caused by hybridization, the structures are less pronounced than in (Ga,Cr)N. In (Ga,Mn)As, the main peak of the Mn 3d states appears well below the valence bands and only a small peak is remains around the Fermi level. For (Ga,Ni)As, the hybridization is so large that the local magnetic moment cannot be sustained, leading to a nonmagnetic ground state.

For a concentration of TM impurities of 5%, Table II summarizes the calculated total magnetic moments per magnetic impurity and local magnetic moments integrated in each muffin-tin sphere for the III-V DMS systems. From the minor deviations between total and local moments, one can conclude that the TM impurity carries the main contribution to the total magnetic moment. For Ni-doped GaP, GaAs, and GaSb *ab initio* calculations predict nonmagnetic ground states (Sato and Katayama-Yoshida, 2002). The electronic configurations of III-V DMS discussed above explain the overall electronic structure of the system quite well. In the ionic picture,

Cr-, Mn-, Fe-, and Co-doped III-V DMSs are predicted to have total magnetic moments of $3\mu_B$, $4\mu_B$, $5\mu_B$, and $4\mu_B$. In general, if the system is half metallic, the total magnetic moment should be an integer and the prediction from the ionic picture should be reproduced well by *ab initio* calculations. As shown in Table II this occurs in the first half of the 3*d* TM series. For the second half the DOS is no longer half metallic, as shown in Fig. 10, and hence the calculated total magnetic moments deviate from integer values. For GaSb-based DMSs the deviation of the magnetic moments from integer values is larger than in other DMS systems. This is mainly due to the underestimation of the band gap by the local-density approximation. Small deviations ($\sim 0.01\mu_B$) from integer values are due to a finite imaginary part of the energy (typically $i\epsilon = 0.1i$ mRy is chosen in the present KKR-CPA calculations).

2. Electronic structure of II-VI DMSs

Here we discuss DMS materials composed of II-VI compounds. As typical examples, we show results for ZnO- and ZnTe-based DMS in Fig. 11, where we assumed wurtzite and zinc-blende structures with the experimental lattice constants of the host compounds (Wyckoff, 1963). We consider again 3*d* transition metals as magnetic impurities. In the figure, the concentration of TM impurities is 5% and the ferromagnetic configuration is assumed. For ZnO-based DMSs [Figs. 11(a)–11(d)] we can distinguish two peaks in the host valence band. One consists mainly of Zn 3*d* states and appears ≈ 0.5 Ry below the Fermi level. The other is due to O 2*p* bands and is distributed from -0.4 to -0.2 Ry. In the band gap the TM impurities induce impurity bands as shown in the figures. The structure of the impurity bands is similar to that of GaN-based DMSs because of the same symmetry at the substitutional tetrahedral site (Sato and Katayama-Yoshida, 2002), i.e., there are bonding t_b states in the energy range of the valence bands, antibonding t_a states above the valence bands, and nonbonding *e* states between these states. In ZnTe-based DMSs, the Te 5*p* states, which lie higher in energy than the O 2*p* states, form the host valence bands; therefore the Zn 3*d* states are split off from the valence band and the TM 3*d* states are energetically closer than in ZnO-based DMSs. Except for this slight difference, the electronic structure of ZnTe-based DMSs is similar to that of ZnO-based DMSs.

For of II-VI DMSs, the TM impurities have two electrons contributing to the bonding, since the TM impurities substitute for the divalent Zn atom. This is different from the situation in III-V DMSs, where three electrons are donated to the valence band, and means that Cr, Mn, Fe, and Co have the following electronic configurations: $d^4(e_\uparrow^2 t_{a\uparrow}^2)$, $d^5(e_\uparrow^2 t_{a\uparrow}^3)$, $d^6(e_\downarrow^1 t_{a\downarrow}^0)$, and $d^7(e_\downarrow^2 t_{a\downarrow}^0)$. These configurations are actually confirmed in first-principles calculations as shown in Fig. 11.

Another important difference between III-V and II-VI DMSs is the location of the valence band. Since the *p* states of the six-valent anions are lower than those
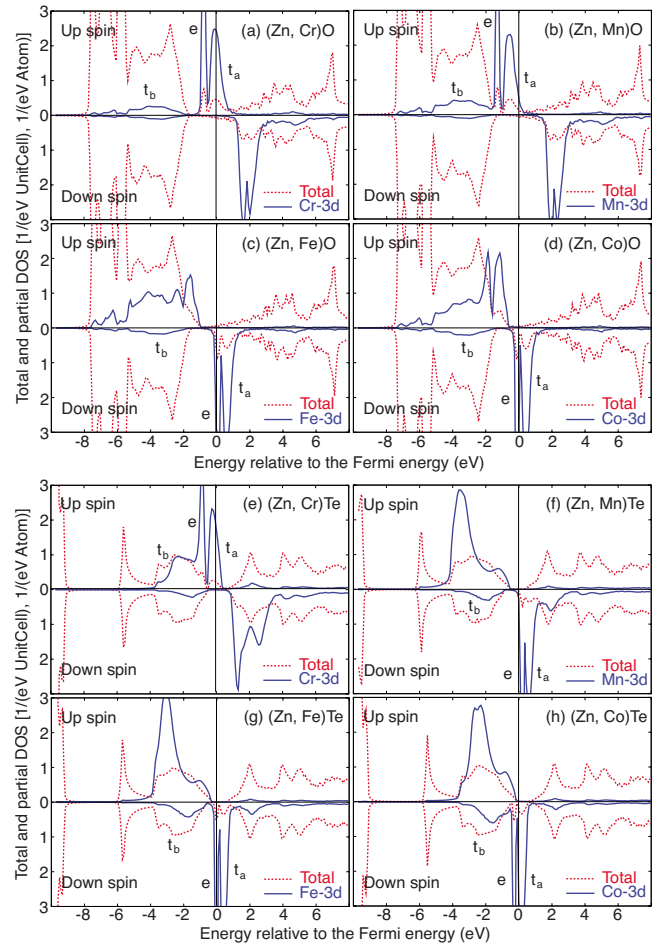

FIG. 11. (Color online) Calculated density of states of ZnO-based (upper panels) and ZnTe-based (lower panels) DMSs. Transition-metal impurities ranging from Cr to Co are considered. Dotted lines show total averaged DOS per unit cell and solid lines show partial DOS per atom of 3*d* components at TM sites. (Note the different scales.) A ferromagnetic configuration is assumed and the TM concentration is 5% for all cases.

of the five-valent anions, the relevant impurity *d* states are always in the gap. Thus a situation as in (Ga,Mn)As, where the *d* level lies in the lower part of the *d* band, does not occur in II-VI DMSs. For the same reason the relevant exchange interaction is always the double-exchange mechanism (see Sec. III.C)

Table III summarizes the calculated total magnetic moment per magnetic impurity and local magnetic moment integrated in each muffin-tin sphere for the II-VI DMS systems. A behavior similar to that of the III-V DMS systems is observed, except for the absolute values of total and local magnetic moments. From the ionic picture, Cr-, Mn-, Fe-, and Co-doped II-VI DMS are predicted to have total magnetic moments of $4\mu_B$, $5\mu_B$, $4\mu_B$, and $3\mu_B$, respectively. This dependence of the total magnetic moment on the atomic number of the TM impurity is almost perfectly reproduced by the *ab initio* calculations, in particular for ZnS, ZnSe, and ZnTe DMS systems. This fact is reasonably well understood from the well-defined half-metallic DOS for these sys-

TABLE III. Calculated total magnetic moment per TM impurity and local magnetic moment (in parentheses) at the TM site of II-VI DMS systems. The concentration of TM impurity is 5%. FM and DLM indicate ferromagnetic and disordered local moment states. A bold number indicates that the system has integer magnetic moment within numerical error, i.e., it is half metallic (except for insulating Mn-doped cases).

	Cr	Mn	Fe	Co
ZnO (FM)	3.57 (2.88)	4.91 (3.94)	4.35 (3.47)	3.11 (2.44)
(DLM)	0 (2.86)	0 (3.93)	0 (3.46)	0 (2.42)
ZnS (FM)	**4.01** (3.35)	**4.99** (4.06)	**3.98** (3.18)	**2.97** (2.22)
(DLM)	0 (3.32)	0 (4.03)	0 (3.15)	0 (2.17)
ZnSe (FM)	**4.02** (3.48)	**4.99** (4.10)	**3.97** (3.17)	**2.97** (2.17)
(DLM)	0 (3.46)	0 (4.08)	0 (3.14)	0 (2.14)
ZnTe (FM)	**4.02** (3.65)	**4.98** (4.05)	**3.97** (3.08)	**2.94** (2.03)
(DLM)	0 (3.63)	0 (4.02)	0 (3.05)	0 (1.98)

FIG. 13. Chemical trends of the energy difference (ΔE) between FM and paramagnetic (DLM) states for ZnO-, ZnS-, ZnSe-, and ZnTe-based DMS. From Sato and Katayama-Yoshida, 2002.

tems [see, for example, Figs. 11(e)–11(h)]. For ZnO-based DMSs, the deviation of the magnetic moment from the integer value is larger than in other DMS systems. This arises because of breaking of the half metallicity due to the serious underestimation of the band-gap energy of ZnO by the local-density approximation. As in the III-V DMSs, in the II-VI DMSs the TM impurity carries the main contribution to the total magnetic moment.

D. Stability of ferromagnetic state and chemical trend

In the previous section, we showed results from CPA calculations of the electronic structure of typical III-V and II-VI DMSs and discussed the chemical trend of the electronic structure of these materials. In this section, we extend the discussion to the type of magnetic ordering in DMS materials.

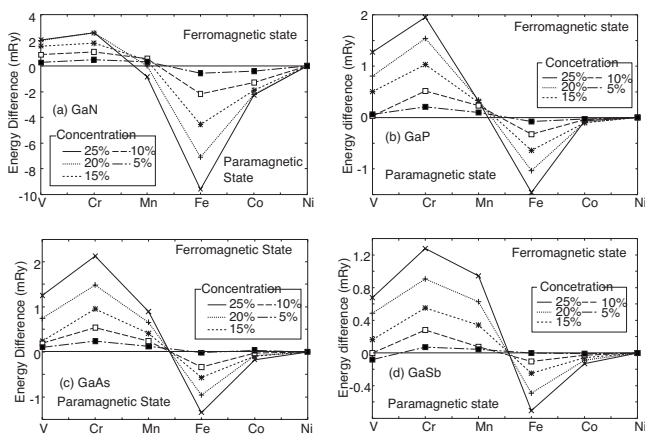Figure 12 shows the calculated total energy difference per unit cell ΔE of III-V based DMSs (Sato and

FIG. 12. Chemical trends of the energy difference (ΔE) between ferromagnetic (FM) and paramagnetic (DLM) states for GaN-, GaP-, GaAs-, and GaSb-based DMSs. From Sato and Katayama-Yoshida, 2002.
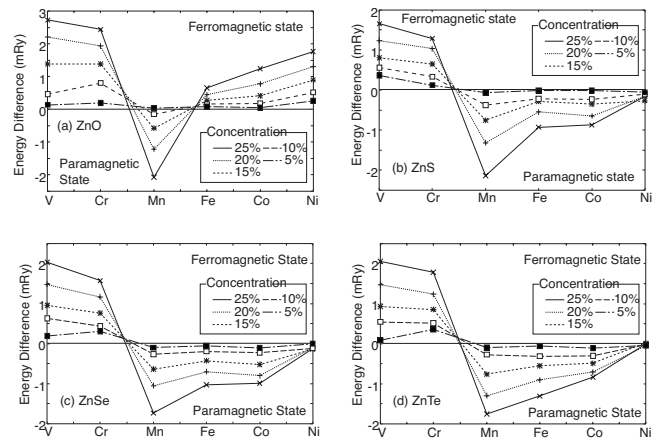
Katayama-Yoshida, 2001b, 2002), which is calculated as the difference between the total energy of the paramagnetic and ferromagnetic states, a positive energy difference indicating that the ferromagnetic state is more stable than the paramagnetic state. As shown in Fig. 12, GaN-, GaP-, GaAs-, and GaSb-based DMS show similar chemical trends, i.e., for the first half of the 3d TM series (V, Cr, and Mn) ΔE is positive and for the latter half (Fe,Co) it is negative. Ni has only a small local moment in these compounds and ΔE is negligibly small. Note that the trend in stability of the ferromagnetic state over the DLM state is independent of concentration at least in the range up to 25% impurity concentration.

Figure 13 shows the TM impurity dependence of ΔE for (II-VI)-based DMS materials (Sato and Katayama-Yoshida, 2000, 2001b, 2002). Similar calculations were recently performed by the supercell method for ZnO-based systems (Spaldin, 2004; Gopal and Spaldin, 2006; Pemmaraju *et al.*, 2008). A resemblance between II-VI and III-V DMSs is obvious. For the first half of the series, ΔE is positive and in the last half it is negative. However, the trend for II-VI DMSs is shifted to lower atomic number by 1 compared to III-V DMSs. This is because in II-VI compounds the TM impurities have a +2 charge state, leading to one more electron occupying TM d states than in III-V compounds. However, the trend in stability of the ferromagnetic state in Fig. 13 is independent of the concentration of transition metals, just like the trend shown in Fig. 12. Thus, when the population of the impurity bands is taken into consideration, the chemical trend of ΔE is universal, and this fact suggests that rather simple rules govern the magnetic state in DMS materials (Sato and Katayama-Yoshida, 2002). The origin of the ferromagnetism and the universal behavior of magnetic interactions will be discussed in the next section.

III. EXCHANGE MECHANISM

A. Exchange coupling constants and mean-field approximation

The most successful method to calculate the thermal properties of a magnetic material and in particular the Curie temperature consists of a two-step approach. First density-functional and related methods are used to calculate, the ground-state properties and in addition the exchange coupling constants (exchange integrals) providing a mapping to a Heisenberg model. In the second step the thermal properties are evaluated using wellknown statistical methods for the Heisenberg model.

The crucial first step requires a number of approximations. First is the adiabatic approximation, assuming that the time scale for fluctuations of the magnetic moments is much larger than that for hopping of the electrons. Second is the magnetic force theorem (Anderson, 1961; Oswald *et al.*, 1985; Liechtenstein *et al.*, 1987), assuming that change in the moment orientations does not cause significant change in the magnetic moments. Since in DMSs the local moments of TM impurities are large and well defined, this assumption is well satisfied (see Tables II and III). The classical Heisenberg model, assumed in our analysis, is given by

$$H = -\sum_{i \neq j} J_{ij} \mathbf{e}_i \mathbf{e}_j, \tag{8}$$

where $\vec{e}_i$ is the unit vector parallel to the local moment $\vec{M}_i$ at site i and J_{ij} are the exchange coupling constants between the local moments at sites i and j, with the absolute value of the moments included in the constants J_{ij}.

For the statistical problem the simplest approximation, in fact the work horse for most applications, is the mean-field approximation (MFA). Within the MFA the thermal behavior is determined by the Brillouin function expression, and the Curie temperature T_C^{MFA} is given by $k_B T_C^{\mathrm{MFA}} = \frac{2}{3} c \Sigma_{n \neq 0} J_{0n}$, where k_B is the Boltzmann constant and c is the concentration of magnetic impurities (Sato *et al.*, 2003). Alternatively one can show that $\Sigma_{n \neq 0} J_{0n}$ is directly related to the difference of the total energies between the ferromagnetic and the disordered local moment states $\Delta E = -E_{\mathrm{FM}} + E_{\mathrm{DLM}} = c^2 \Sigma_{n \neq 0} J_{0n}$, since in the Heisenberg model the DLM ground-state energy vanishes, while the FM ground-state energy is given by $-c^2 \Sigma_{n \neq 0} J_{0n}$. Thus, in the mean-field approximation the critical temperature can also be evaluated by the total energy difference ΔE, since $k_B T_C^{\mathrm{MFA}} = \frac{2}{3} \Delta E / c$. Note that this expression does not assume that the magnetic force theorem is valid, as long as both states are calculated self-consistently. However, the DLM state might also be calculated non-self-consistently using the "frozen" local moments of the FM state. According to the magnetic force theorem, in this case the difference between the total energies can be replaced by the difference between the single-particle energies, which are directly related to the local density of states of the magnetic impurities in the FM and DLM states. In practical applications all results usually give, up to some percent, the same values for T_C^{MFA}.

The advantage of the MFA is its simplicity and the direct relation of ΔE to the local density of states, which admits a direct and simple understanding of the underlying exchange mechanisms. We profit from this in great detail in Sec. III.B, where, based on simple models for the local density of states, we discuss the importance of three different exchange mechanisms in DMSs, i.e., Zener's double exchange and *pd* exchange, both favoring ferromagnetic coupling, and superexchange which leads to antiferromagnetic coupling.

An important disadvantage of the MFA is its limited accuracy. In homogeneous ferromagnets and disordered ferromagnetic alloys (with high concentrations) the MFA gives quite acceptable results; however, it totally fails in the dilute limit, i.e., in the typical concentration range of 5–8 % of DMS materials. The reason for this is that the MFA cannot describe the percolation effect, i.e., that a finite connected concentration region of TM atoms is necessary to obtain ferromagnetism. For zinc-blende-based DMSs like GaMnAs, the Mn atoms are on the fcc Ga sublattice. However, for a fcc lattice with nearest-neighbor interactions only, ferromagnetism cannot occur below a percolation threshold of 20%, independently of the strength of the nearest-neighbor (NN) interaction (Stauffer and Aharony, 1994). Since usually the nearest-neighbor coupling is the strongest interaction, the MFA usually predicts rather high-T_C values, while the real Curie temperatures are much lower due to the much weaker longer-ranged interactions. More reliable methods to calculate T_C are the LRPA, which is semianalytical and convenient, and the more time-consuming Monte Carlo simulations, which are numerically exact. Both methods and the T_C results for many DMS systems are discussed in Sec. IV.

These improved methods that go beyond the MFA require explicit knowledge of the distance dependence of the exchange integrals J_{ij}^{QQ} between two magnetic TM atoms of type Q (for example, Mn) at sites i and j. The standard approach to determine these exchange integrals is due to Liechtenstein *et al.* (1987) and calculates the total energy difference due to an infinitesimal change in the angle between the two moments by Lloyd's formula, with the result

$$J_{ij}^{QQ} = \frac{1}{4\pi} \mathrm{Im}\, \mathrm{Tr}_L \int_{E_F} dE\, \Delta t_i^Q(E)$$
$$\times G_{ij}^{\uparrow QQ}(E) \Delta t_j^Q(E) G_{ji}^{\downarrow QQ}(E), \tag{9}$$

where Tr_L means the sum over all angular momenta and $\Delta t_i^Q(E) = t_i^{Q\uparrow}(E) - t_i^{Q\downarrow}(E)$ is the difference between the atomic t matrices of impurity Q at site i for the majority ($\uparrow$) and minority ($\downarrow$) spin directions. $G_{ij}^{\uparrow(\downarrow)}(E)$ is the Green's function of the system describing the propagation between site i and site j for the spin-up (or spin-down) electrons.

In disordered systems we have to average J_{ij}, the exchange interactions for two impurities, say two Mn at-

oms, at sites i and j over the positional and orientational disorder of all other Mn impurities. The result is that one has to replace the Green's function G_{ij} in Eq. (9) by the conditionally averaged Green's function $\langle G_{ij}^{MnMn} \rangle$ for two Mn impurities i and j in the CPA medium (Akai, 1998). This conditional Green's function for two impurities of type Q at sites i and j is given by

$$\langle G_{ij}^{QQ} \rangle = [1 - G_{ii}^{CPA}(t_i^Q - t_i^{CPA})]^{-1}$$
$$\times G_{ij}^{CPA}[1 - G_{jj}^{CPA}(t_j^Q - t_j^{CPA})]^{-1}. \quad (10)$$

The first factor describes the scattering at impurity Q at site i, the second factor, given by the CPA Green's function G_{ij}^{CPA}, the propagation from site i to site j in the CPA medium, and the third factor the scattering at the impurity at site j. For simplicity the spin indices $\uparrow$ or $\downarrow$ are neglected; they are the same for all factors in Eq. (10). The prefactors and postfactors in Eq. (10) are particularly important for strong scattering, i.e., when a virtual bound state exists for a given energy and spin direction, where they strongly enhance the CPA Green's function. The factors are not important for weak scattering.

Recently it has been shown that the conditional average expression for $\langle G_{ij}^{QQ} \rangle$ is not optimal for small concentrations; in particular, it leads to too large an exchange coupling for near neighbors in double-exchange systems. In this case G_{ij}^{CPA} should be replaced by the exact expression for the impurity pair (Qi, Qj) in the CPA medium (Sato *et al.*, 2007b).

Quadratic averages $\langle GG \rangle$, describing vertex corrections, have been shown to vanish at first order due to the vertex-cancellation theorem (Turek *et al.*, 2006). Thus the Lichtenstein formula [Eq. (9)] has the important advantage that a direct calculation of the ensemble-averaged coupling constants J_{ij} is possible via the CPA formalism. This is very difficult to achieve by any other method. For instance, in the supercell method one has to calculate the total energy difference between a tilted and a nontilted configuration of two Mn atoms, with the other Mn atoms more or less statistically distributed. This needs large supercells and many self-consistent calculations for different Mn environments, which is an extremely time-consuming procedure (see Sec. III.D.3).

B. Concentration dependence of T_C^{MFA} and carrier doping effects

As a characteristic example of mean-field calculations we show in Fig. 14 the results for T_C^{MFA} of (Ga,Mn)N, (Ga,Mn)P, (Ga,Mn)As, and (Ga,Mn)Sb (Sato, Dederichs, *et al.*, 2004). These Mn-doped systems show dramatic changes in the concentration dependence for the different anion atoms. As shown in the figure, T_C^{MFA} increases approximately proportionally to the square root of the Mn concentration c for (Ga,Mn)N, (Ga,Mn)P, and (Ga,Mn)As. In particular, T_C^{MFA} of (Ga,Mn)N shows a sharp increase for low concentrations before it becomes reduced. As a result, T_C^{MFA} has a maximum at around
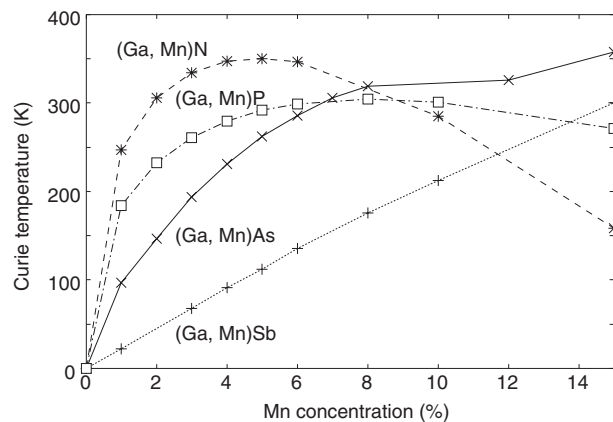

FIG. 14. Calculated T_C^{MFA} of (Ga,Mn)N, (Ga,Mn)P, (Ga,Mn)As, and (Ga,Mn)Sb as a function of Mn concentration. From Sato, Dederichs, *et al.*, 2004.

5% Mn concentration. In (Ga,Mn)P, after the sharp increase for low concentrations, T_C^{MFA} saturates at around 300 K for higher concentrations. The increase in T_C^{MFA} of (Ga,Mn)As is rather moderate compared to that in (Ga,Mn)P. Finally, (Ga,Mn)Sb shows an almost linear concentration dependence. As a whole, the increase in T_C^{MFA} with c becomes less pronounced from GaN to GaSb. This transition in the concentration dependence of T_C^{MFA} originates from a systematic change in the dominant exchange mechanism (Sato, Dederichs, *et al.*, 2004), with double exchange dominating for (Ga,Mn)N and p-d exchange determining the behavior of (Ga,Mn)Sb, while for (Ga,Mn)As both mechanisms are important.

Carrier doping effects. The magnetic properties of DMSs can be controlled by band filling effects. Although the MFA does not give an accurate prediction of T_C, we show the calculated doping dependence of T_C^{MFA} in (Ga,Mn)As and (Ga,Mn)N, in order to investigate the qualitative behavior of the dependence of T_C (Sato *et al.*, 2003).

In Fig. 15, the calculated values of T_C^{MFA} of (Ga,Mn)N and (Ga,Mn)As are shown as a function of additional carrier concentration. In both cases, additional holes are
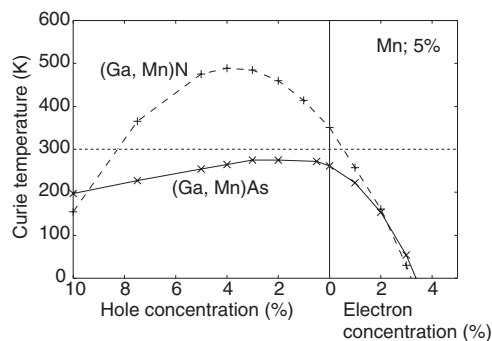

FIG. 15. T_C^{MFA} of (Ga,Mn)N (dashed line) and (Ga,Mn)As (solid line) calculated with additional donor (O for GaN and antisite As for GaAs) or acceptor doping (Mg for both compounds). From Sato *et al.*, 2003.
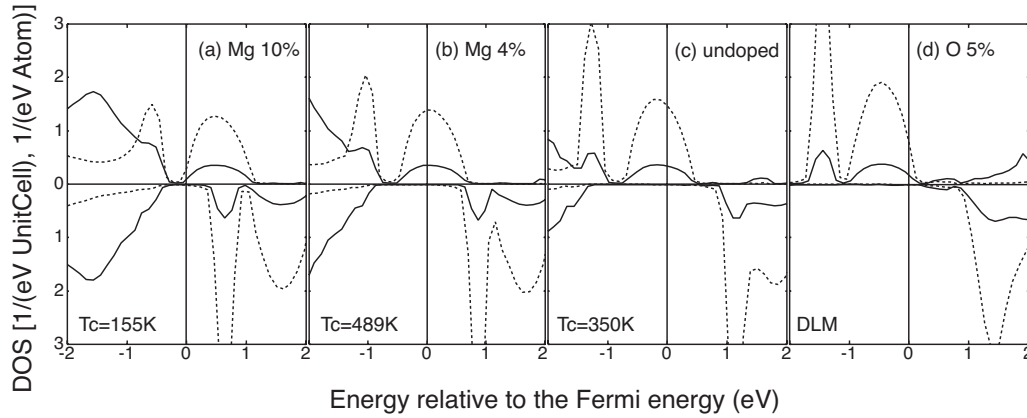
FIG. 16. Calculated total DOS (solid lines) and partial density of $3d$ states at Mn site (dotted lines) in (Ga,Mn)N for various additional carrier concentrations. From Sato *et al.*, 2003.

doped by introducing Mg impurities at Ga sites. In GaN additional electrons are introduced by substituting O for N, and in GaAs by antisite As. As shown in the figure, for both compounds the additional electron doping (i.e., compensating holes introduced by Mn) causes T_C^{MFA} to decrease sharply, and above 3% the ferromagnetism disappears. On the other hand, T_C^{MFA} of (Ga,Mn)N is increased dramatically by additional hole doping and has a maximum value at ~4%. In the case of (Ga,Mn)As, hole doping does not affect the values of T_C^{MFA} so much.

The doping effects in (Ga,Mn)N are easily understood by an analysis of the calculated DOS (Sato *et al.*, 2003). Figure 16 shows the total and partial DOSs of (Ga,Mn)N for several carrier concentrations. The Mn concentration is fixed to 5% and a ferromagnetic state is considered. As shown in the figure, the Fermi level is located in the impurity bands when no additional carriers are introduced. As discussed in Sec. II.C, approximately two-thirds of the impurity bands are occupied; therefore the Fermi level is located at the higher energy side of the peak as shown in Fig. 16(c). By introducing additional holes, the Fermi level is shifted to lower energy and approaches the center of the impurity bands. As a result, the double-exchange mechanism, discussed below, is optimized and T_C^{MFA} reaches a maximum at about 4% [Fig. 16(b)]. For higher hole concentrations, the Fermi level passes the main part of the impurity bands and the impurity t_a states become empty, as shown in Fig. 16(a). Consequently, T_C^{MFA} becomes reduced due to the weakening of the double-exchange mechanism. The system is still ferromagnetic with 10% of additional holes, where the system becomes nearly insulating, due to the ferromagnetic contribution from the superexchange interaction (see Sec. III.C.5). The hole states are fully compensated by introduction of 5% of additional electrons as shown in Fig. 16(d), and the ferromagnetism disappears. Doping effects in ZnO-based DMSs were also reported recently (Gopal and Spaldin, 2006; Pemmaraju *et al.*, 2008).

C. Exchange mechanisms in dilute magnetic semiconductors

Despite the fact that by *ab initio* calculations one can calculate the magnetic properties and their thermal behavior with reasonable accuracy, as can be seen by the results in Sec. III.C.3 for photoemission and Sec. IV for T_C values, a physical understanding of the exchange mechanism that stabilizes ferromagnetism or leads to magnetic disorder is a challenging problem. As stated already several different mechanisms exist, which can lead to ferromagnetism or antiferromagnetism, and often some of them act simultaneously. The aim of this section is to describe the three different relevant exchange mechanisms that dominate the magnetic properties of dilute magnetic semiconductors: Zener's double-exchange mechanism (Zener, 1951a; Anderson and Hasegawa, 1955; de Gennes, 1960; Akai, 1998) and Zener's *p-d* exchange mechanism (Zener, 1951b; Dietl *et al.*, 2000; Kanamori and Terakura, 2001; Sato, Dederichs, *et al.*, 2004; Dalpian *et al.*, 2006) favor the ferromagnetic coupling, while superexchange (Kramers, 1934; Anderson, 1950; Goodenough, 1955; Kanamori, 1959) usually leads to antiferromagnetic coupling. In particular, for each mechanism we discuss the concentration dependence, the dependence on the position of the Fermi level, the range of the interactions, and the effect of a Hubbard U parameter in a LDA+U calculation.

Our discussions are based on two approximations. First, we apply the frozen potential approximation or magnetic force theorem, according to which the difference in the total energy is well approximated by the difference in the single-particle energies (Andersen *et al.*, 1980; Oswald *et al.*, 1985; Liechtenstein *et al.*, 1987; Antropov *et al.*, 1999). Thus we can concentrate the discussion on the spin-polarized local DOS only, and in particular on the interaction effects in the DOS introduced by the hybridization with the wave functions of neighboring atoms. Second, we discuss only the disorder-averaged density of states, as obtained by the coherent potential approximation, which provides a mean-field description of the electronic structure.
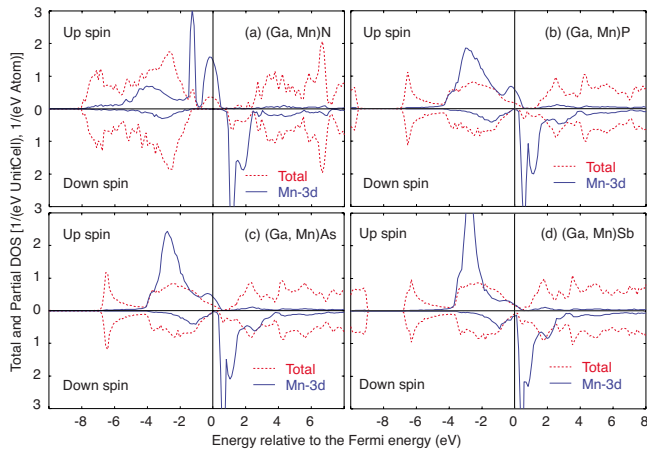
FIG. 17. (Color online) Calculated density of states in (a) (Ga,Mn)N, (b) (Ga,Mn)P, (c) (Ga,Mn)As, and (d) (Ga,Mn)Sb. Total DOS (dotted lines) and partial density of 3d states at Mn site (solid lines) are shown. The Mn concentration is 5% and a ferromagnetic configuration is assumed for all cases. Up spin (down spin) means majority (minority) spin in ferromagnetic state.

As an illustrative example for the electronic structure of DMSs we show in Fig. 17 the spin-polarized DOS of (Ga,Mn)N, (Ga,Mn)P, (Ga,Mn)As, and (Ga,Mn)Sb. The solid curves, giving the local Mn DOS for a concentration of 5% Mn, exhibit for different anions very different behavior, which has its origin in the position of the atomic p level of the anion with respect to the d level of the Mn atom. The p band of N, located within the band gap, lies well below the t_{2g} and e_g impurity bands of Mn, while the center of the p band of Sb is located above the large peak in the d DOS of Mn. (Ga,Mn)P and (Ga,Mn)As are intermediate cases with the majority d DOS showing a pronounced two-peak structure, a weaker d resonance at the Fermi level, and a large d peak at lower energies. As discussed below, the magnetic properties of (Ga,Mn)N are dominated by double exchange, while in (Ga,Mn)Sb p-d exchange is the dominant mechanism. In (Ga,Mn)P and (Ga,Mn)As both mechanisms play a role.

1. Zener's double exchange

Figure 18(a) shows schematically the spin-polarized DOS of a transition-metal impurity in a wide-band-gap semiconductor, such as Mn or Cr in GaN. The Fermi level is assumed to fall within the partially occupied majority band of the t_{2g} impurity state. The stabilization of the ferromagnetic state arises from the width of the impurity band. For instance, if the Fermi level lies in the middle of the impurity band, as is assumed in the figure, only bonding states are occupied, while the antibonding states are empty. For a molecular model with two atomic states of energies $\epsilon_1 = \epsilon_2$ and a hopping matrix element t the bonding-antibonding splitting is sketched on the right-hand side of Fig. 18. If only the bonding state is occupied, one obtains an energy gain of $|t|$ for ferromagnetically coupled impurities; otherwise, the energy gain
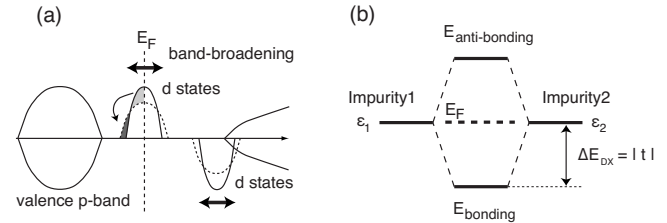

FIG. 18. Schematic diagram of the electronic structure in the case of double exchange. (a) Schematic of the spin-polarized DOS of a transition-metal impurity in a wide-gap semiconductor. The d level is located in the band gap for the spin-up states. The full lines show the spin-up and spin-down impurity bands for a small concentration, the dashed lines for a larger concentration. The gray areas indicate that more energy can be gained by band broadening, since states are transferred to lower energies. (b) Schematic representation of the hybridization-induced energy gain ΔE_{DX} for a diatomic system with unperturbed levels $\epsilon_1 = \epsilon_2$.

is zero. For an impurity band as shown in Fig. 18(a) the bandwidth scales linearly with the hopping matrix element t between neighboring impurities and as the square root $\sqrt{c}$ of the impurity concentration c. This is then the energy gain caused by the double-exchange mechanism, leading to a lowering in energy of the ferromagnetic state which can be expressed as

$$\Delta E_{DX} \sim \sqrt{c}|t|. \tag{11}$$

As a function of E_F, the energy gain is largest if the Fermi level lies in the middle of the band and vanishes if E_F lies at the band edge. For a rectangular DOS model, this behavior is given by an inverted parabola with its maximum in the center of the band. Thus no energy is gained for ferromagnetically coupled impurities if the impurity band is completely filled (both bonding and antibonding states are occupied) or completely empty. The $\sqrt{c}$ dependence of the bandwidth is well reproduced (Sato, Dederichs, *et al.*, 2004) in CPA calculations. It can be derived from a tight-binding description of the impurity band (Sato, Dederichs, *et al.*, 2004). The bandwidth W, defined as the variance of the energy eigenvalues E from the mean value $\bar{E}$, obeys the relation (Harrison, 1989)

$$W^2 = \langle (E - \bar{E})^2 \rangle = \sum_{m \neq 0} |H_{0m}|^2, \tag{12}$$

where H_{0m} denotes the hopping matrix element between the sites 0 and m. Suppose that in a certain configuration of Mn atoms in GaN one of the Mn atoms is at site 0. In this configuration, H_{0m} has a finite value, say, t_{0m}, if another Mn atom is at site m; otherwise, $H_{0m}=0$. In the CPA, we make a configurational average over all sites $m \neq 0$. The probability for finding a Mn atom at site m is given by c, the atomic concentration of Mn. Thus the configurational average gives $\langle W^2 \rangle_{\text{conf}} = c\sum_{m \neq 0}|t_{0m}|^2$. Therefore the effective bandwidth W is proportional to $\sqrt{c}$ (Sato, Dederichs, *et al.*, 2004) and the energy gain by double exchange [Eq. (11)] scales as $\sqrt{c}|t|$.
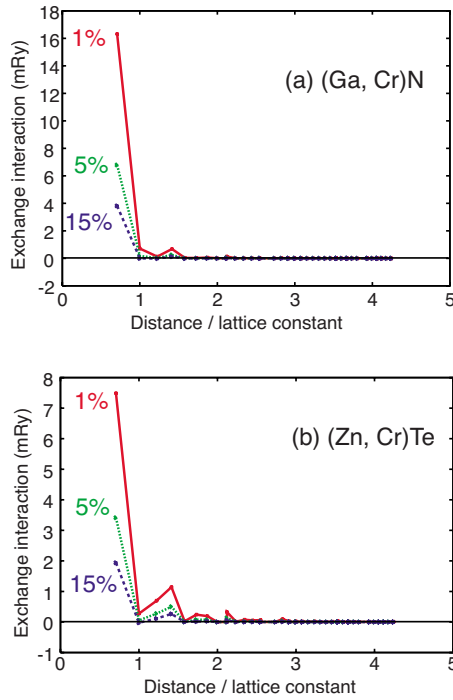
FIG. 19. (Color online) Calculated exchange interactions between Cr impurities in (a) (Ga,Cr)N and (b) (Zn,Cr)Te.

The $\sqrt{c}$ dependence of the double-exchange interaction, obtained in the mean-field (CPA) description, distinguishes this mechanism strongly from all other exchange mechanisms which are discussed in the following sections. Since, as discussed in Sec. III.A, the Curie temperature in the mean-field approximation is given by

$$k_B T_c^{\mathrm{MFA}} = \frac{2}{3}\Delta\epsilon, \tag{13}$$

where $\Delta\epsilon$ is the energy difference per Mn atom between the ferromagnetic and DLM phases. Thus, if double exchange is dominant, T_C^{MFA} scales as $\sqrt{c}$, which is shown in Fig. 14 for (Ga,Mn)N, but also for (Ga,Mn)P and (Ga,Mn)As although for these systems the value of $|t|$ is naturally different, due to differences in the electronic structure. Only (Ga,Mn)Sb shows a strictly linear behavior (typical for *p-d* exchange; see below).

The double-exchange mechanism can be very strong. Thus, when the Fermi level lies within the impurity band, double exchange usually dominates other exchange mechanisms (for example, the antiferromagnetic superexchange) and it stabilizes the ferromagnetic configuration. Since in wide-gap semiconductors the deep-impurity level wave functions are well localized and the host Green's function decays exponentially for energies in the gap, this kind of double-exchange interaction is very short ranged. This is shown in Fig. 19 for the exchange coupling constants J_{ij} calculated by Eq. (9). We show distance and concentration dependences of J_{ij} between Cr in (Ga,Cr)N [Fig. 19(a)] and in (Zn, Cr)Te [Fig. 19(b)]. In both cases we observe a short-ranged interaction, more pronounced in GaN. As discussed in Sec. III.D, this is due to the presence of a gap in one of the spin channels. Because of the strong localization of the
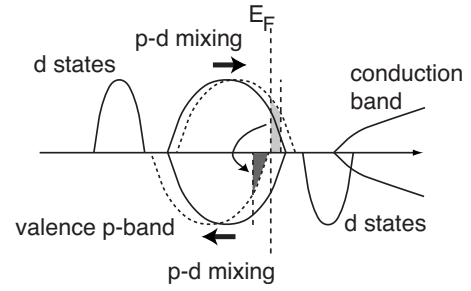

FIG. 20. Schematic diagram of the spin-polarized DOS in the case of *p-d* exchange, when the majority-spin *d* level lies below the valence *p* band and the minority level above. The dashed curve represents the valence band after interaction with the magnetic impurities (*p-d* mixing).

interaction, in the dilute limit the ferromagnetic interactions cannot percolate through the crystal and the Curie temperatures are vanishingly low, in contrast to the large mean-field values T_C^{MFA} for T_C.

The mean-field-like description of the electronic structure by the CPA leads to an unphysical artifact in the calculated J_{01} values for the double-exchange case. The energy difference $\Delta\epsilon$ between the ferromagnetic and the DLM phases is given in the mean-field approximation by

$$\Delta\epsilon = c\sum_{j\neq 0} J_{0j} \cong 12cJ_{01}. \tag{14}$$

In this equation we have taken only the dominant coupling J_{01} with the 12 nearest neighbors (for example, in the fcc Ga sublattice) into account. Since in the case of double exchange $\Delta\epsilon \sim \sqrt{c}$, we find that $J_{01} \sim 1/\sqrt{c}$ should diverge for very small concentrations. This is indeed found in calculations for very small concentrations. See, for example, the results shown in Fig. 19 (and also in Fig. 36, below) for small Mn concentrations in (Ga,Mn)As. This problem can be dealt with only by replacing the single-site CPA by a two-center treatment of the interaction as described by Sato *et al.* (2007b). (For the calculated Curie temperature this is not important, since in the dilute limit the nearest-neighbor interactions are not important because of the percolation effect.)

2. Zener's *p-d* exchange

Figure 20 shows the physical situation for Zener's *p-d* exchange interaction. In narrow-gap semiconductors like GaSb or InSb the Mn *d* majority level lies below or at the lower edge of the Sb *p* band, while the minority *d* level lies well above E_F. This means that Mn has a local moment of about $5\mu_B$, well localized at the Mn site. In the neutral state due to charge neutrality one electron per Mn atom is missing in the valence band as indicated by the position of E_F in Fig. 20. The full curve illustrates the situation where 1/2 electron per Mn impurity is missing in both spin-up and spin-down valence bands. However, since the impurity *d* wave functions hybridize with the *p* wave functions of the neighboring *p* elements,

the majority-spin p band is shifted to higher energies, while the minority-spin p band is shifted to lower energies due to hybridization with the higher-lying minority-spin d state (both bands, spin up and spin down, are indicated by the dashed lines in Fig. 20) (Kanamori and Terakura, 2001; Sato, Dederichs, *et al.*, 2004). If the hybridization is sufficiently strong, the minority p band becomes completely occupied, while one electron per Mn atom is missing in the majority p band, leading to a half-metallic density of states. As a result the Sb atoms carry small total moments of $1\mu_B/$Mn, antiparallel to the local moment of Mn, such that the total effective moment per Mn atom is $4\mu_B$. Thus the hybridization with the occupied majority- and unoccupied minority-spin d states of Mn acts like a magnetic field on the valence band states, which induces a spin polarization in the host.

To quantify this discussion, we consider a simple molecular model of a spin-polarized (nondegenerate) d state with a single non-spin-polarized p state. For the amplitudes $c_d^\uparrow$, $c_d^\downarrow$ and $c_p^\uparrow$, $c_p^\downarrow$ of the wave functions we obtain for the two spin directions

$$(\epsilon_d^{0\uparrow} - \epsilon)c_d^\uparrow + V_{dp}^\uparrow c_p^\uparrow = 0, \quad (\epsilon_p^0 - \epsilon)c_p^\uparrow + V_{dp}^\uparrow c_d^\uparrow = 0,$$
$$(\epsilon_d^{0\downarrow} - \epsilon)c_d^\downarrow + V_{dp}^\downarrow c_p^\downarrow = 0, \quad (\epsilon_p^0 - \epsilon)c_p^\downarrow + V_{dp}^\downarrow c_d^\downarrow = 0. \quad (15)$$

Here $\epsilon_d^{0\uparrow}$ and $\epsilon_d^{0\downarrow}$ are the unperturbed majority ($\uparrow$) and minority ($\downarrow$) d levels and ϵ_p^0 denotes the spin-degenerate, unperturbed p level. $V_{dp}^\uparrow$ describes the hybridization between the low-lying $d^\uparrow$ state and the p state and $V_{dp}^\downarrow$ that with the high-lying $d^\downarrow$ level.

In second order with respect to V_{dp} the changes in the p levels are given by

$$\epsilon_p^\uparrow = \epsilon_p^0 + \frac{|V_{dp}^\uparrow|^2}{\epsilon_p^0 - \epsilon_d^{0\uparrow}}, \quad \epsilon_p^\downarrow = \epsilon_p^0 + \frac{|V_{dp}^\downarrow|^2}{\epsilon_p^0 - \epsilon_d^{0\downarrow}}. \quad (16)$$

Thus the majority level $\epsilon_p^\uparrow$ is shifted upward and becomes partially unoccupied and the minority level $\epsilon_p^\downarrow$ is shifted downward and is filled, as is qualitatively indicated for the p bands in Fig. 20. The difference

$$H_{dp} = \frac{1}{2}(\epsilon_p^\uparrow - \epsilon_p^\downarrow) = \frac{1}{2}\left(\frac{|V_{dp}^\uparrow|^2}{\epsilon_p^0 - \epsilon_d^{0\uparrow}} + \frac{|V_{dp}^\downarrow|^2}{\epsilon_d^{0\downarrow} - \epsilon_p^0}\right) = J_0 \quad (17)$$

can be considered as an effective magnetic field, induced by the hybridization of the localized d states with the p band in the vicinity of the impurity. Note that H_{dp} changes its sign if the moment is inverted.

Based on this result the antiferromagnetic coupling between the Mn spins S_i at position i and the host polarization $\vec{s}(\mathbf{R}_i)$ can be described by an isotropic Hamiltonian (S_i is a direction vector)

$$H_k = J_0 \sum_i \vec{S}_i \cdot \vec{s}(\mathbf{R}_i). \quad (18)$$

Thus the host polarization $\vec{s}(\mathbf{R}_i)$ induced by other local moments tends to align the moments $\vec{S}_i$ antiparallel to $\vec{s}(\mathbf{R}_i)$ (and parallel to the other Mn moments). Since for the ferromagnetic state the average host polarization is given by the concentration c but vanishes for the DLM state, this favors the ferromagnetic state by an energy of $-cJ_0$ per Mn atom. Thus in this p-d exchange model the mean-field Curie temperature is given by

$$T^{\text{MFA}} = c\frac{2}{3}J_0. \quad (19)$$

The important point is that, due to the large extension of the p-wave functions, representing the hole state, the p-d exchange coupling is relatively weak, but more long ranged. In the dilute limit it is therefore not as strongly affected by percolation effects as is the double-exchange mechanism.

For the situation described in Fig. 20 there exists, in addition to the ferromagnetic p-d exchange, an antiferromagnetic superexchange (see Sec. III.C.4) resulting from the hybridization of the low-lying majority d orbitals with the unoccupied minority d orbital. Because of the large splitting of these levels this effect is rather small, although in general antiferromagnetic superexchange can be quite strong.

3. Competition between double and *p-d* exchange in (Ga,Mn)As

The double-exchange and p-d exchange mechanisms are extreme cases of a more general type of interaction, where both mechanisms can occur simultaneously. However, contributions of the double-exchange and p-d exchange mechanisms can be distinguished by the concentration dependence of the mean-field estimate of the Curie temperature T_C^{MFA}, which varies as $\sqrt{c}$ for the double exchange and c for the p-d exchange. *Ab initio* calculations show that, in (Ga,Mn)N the d level is deep in the band gap, so that the behavior should be dominated by double exchange (Sato, Dederichs, *et al.*, 2004) (see also Sec. III.B). Indeed, in Fig. 14 for small concentrations the MFA Curie temperature shows a pronounced $\sqrt{c}$ dependence. On the other hand, (Ga,Mn)Sb is dominated by p-d exchange and shows a linear c dependence for T_C^{MFA} in Fig. 14 (Sato, Dederichs, *et al.*, 2004). On the other hand, (Ga,Mn)P and (Ga,Mn)As are transition cases, as shown in Fig. 14. LDA calculations yield a $\sqrt{c}$ concentration dependence, although the prefactor is considerably smaller than for (Ga,Mn)N or (Ga,Mn)P. In LDA+U calculations for (Ga,Mn)As the Mn majority level is shifted to lower energies by 1.5 eV if a U value of 4 eV is used. The location of the d peak at -4.2 eV below E_F (see inset in Fig. 21) is then in good agreement with the photoemission measurements (see below). In line with this the mean-field T_C^{MFA} value shows a more pronounced linear c dependence (see Fig. 21), indicating that the double-exchange mechanism is reduced and that the p-d exchange is now more important. As is shown in Fig. 37, the coupling is then slightly reduced but somewhat more long ranged. At this point it is worthwhile to point out that a recent self-interaction-corrected LSDA calculation results in a more localized behavior of the Mn d states, which results in an exchange that is almost entirely of p-d char-
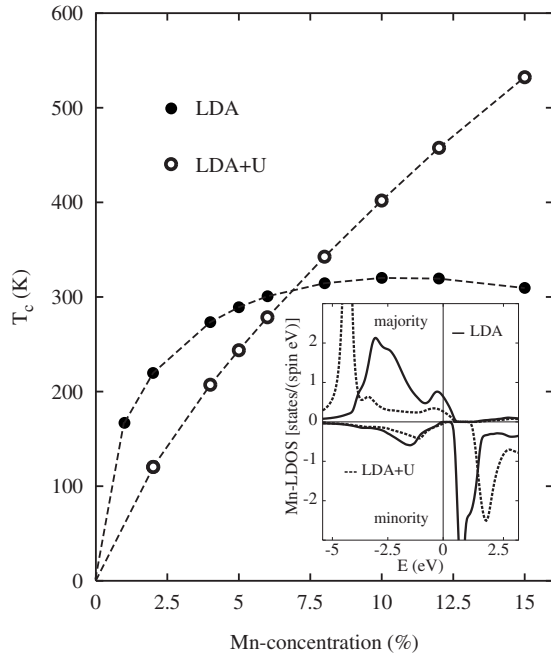
FIG. 21. T_C^{MFA} values of (Ga,Mn)As calculated within the LDA (closed circles) and the LDA+U (open circles). The inset shows partial DOS of Mn d states in 5% Mn-doped GaAs calculated by use of the LDA (solid lines) and the LDA+U (dotted lines). For the LDA+U calculations a value $U=4$ eV is assumed. From Sato, Dederichs, *et al.*, 2004.
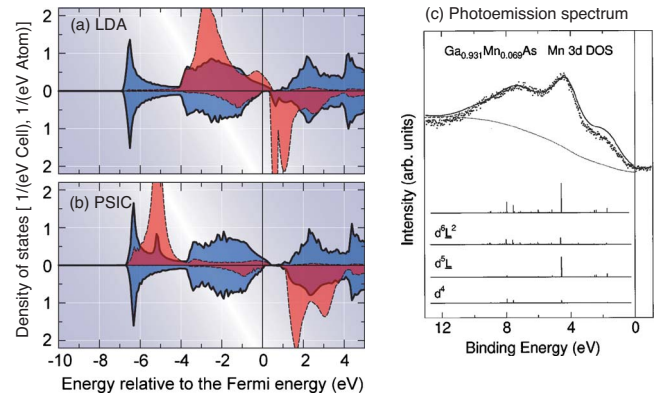

FIG. 22. (Color online) Calculated total and partial DOSs of (Ga,Mn)As by (a) the LDA and (b) the PSIC method. In the calculations, Mn concentrations are fixed to 5%. Light part indicates Mn 3d components and dark part indicates total density of states. (c) Experimental photoemission spectrum of (Ga,Mn)As (Okabayashi *et al.*, 1999). The experimental Mn concentration is 6.9%.

acter. In order to evaluate which approximation to the effective potential of Eq. (2) is the most accurate one, it is vital to compare the resulting electronic structure to experimental values. Hence an accurate experimental determination of the degree of correlation or localization of the Mn d states is crucial in order to understand the true nature of the interatomic exchange interaction (Schulthess *et al.*, 2007). It is characteristic for both interactions, i.e., double and p-d exchange, that the Fermi level lies within the valence band. If the Fermi level lies above the valence band the hybridization effects are the same, but no energy can be gained to favor ferromagnetism.

Thus, we have shown that the relative importance of the p-d exchange and the double-exchange mechanisms depends on the detailed electronic structure of the DMS, particularly on the position of the d states of the magnetic impurities. Therefore, it is important to know how accurately the LDA describes the electronic structure of DMS systems. For this purpose we compare calculated electronic structures of (Ga,Mn)As and (Zn,Cr)Te to experimental photoemission spectra. We picked these systems because the fabrication technique and the ferromagnetism of these materials seems to be well established and confirmed (Matsukura *et al.*, 2002). Moreover, calculated mixing energies (see Fig. 53) of these compounds are positive but rather small, indicating only a relatively small tendency for clustering. One reason why the LDA predicts occupied d states at too high energy is the spurious self-interactions. A scheme to correct the self-interaction was proposed by Perdew

and Zunger (1981), and applied to the III-V DMS systems by Schulthess *et al.* (2005). Recently, Filippetti and Spaldin (2003) proposed a pseudo-self-interaction correction (PSIC) method and succeeded in reproducing electronic structures of strongly correlated systems with a minimal increase in computing cost. In order to be compatible with the SIC total energies, the resulting SIC single-particle potential is reduced by a factor of 1/2. We have implemented the PSIC method into the KKR-CPA package (Toyoda *et al.*, 2006). For a comparison, we compare the DOSs calculated by the LDA and PSIC to the experimental photoemission spectra (Okabayashi *et al.*, 1999) in Fig. 22.

In the experiment, the resonance technique was used to extract Mn d states. As shown in Fig. 22(c) the main peak of the Mn d states was observed at ≈ 4.5 eV below E_F. On the other hand, the LDA predicts the Mn d states at -2.7 eV and this is much higher than the observed position. The above LDA+U calculations give the peak at -4.2 eV. To a large extent this discrepancy is also corrected by the PSIC method, as shown in Fig. 22(b) where the Mn d states are located at -5.2 eV. Calculations of Schulthess *et al.* (2007) using a SIC-based optimized effective potential (OEP) method give the Mn peak at -3.7 eV. Thus all these methods, PSIC, OEP-SIC, and LDA+U with $U=4$ eV, improve the LDA results and yield better agreement with experiment. Similar results are obtained in (Zn,Cr)Te as shown in Fig. 23. In the experiment, the Cr d and Zn d components were observed at -3 and -11 eV, respectively (Kobayashi *et al.*, 2007). These energy positions are well reproduced by the PSIC method [Fig. 23(b)] but not by the LDA [Fig. 23(c)]. As explained, the SIC treatment shifts the occupied d states to lower energy. Due to this shift, the amplitude of d states at E_F is reduced, and the importance of the double exchange is diminished, but still dominates the exchange coupling in (Zn,Cr)Te. Another effect is the enhancement of the exchange splitting as shown in
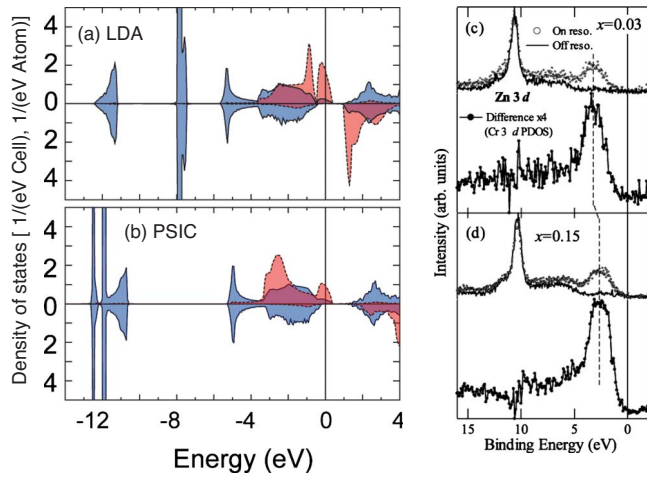
FIG. 23. (Color online) Calculated total and partial DOSs of (Zn,Cr)Te by (a) the LDA and (b) the PSIC method. In the calculations, Cr concentrations are fixed to 5%. Light part indicates Cr 3*d* components and dark part indicates total density of states. (c) and (d) Experimental photoemission spectra of (Zn,Cr)Te (Kobayashi *et al.*, 2007) and the experimental Cr concentrations are 3% and 15%, respectively.
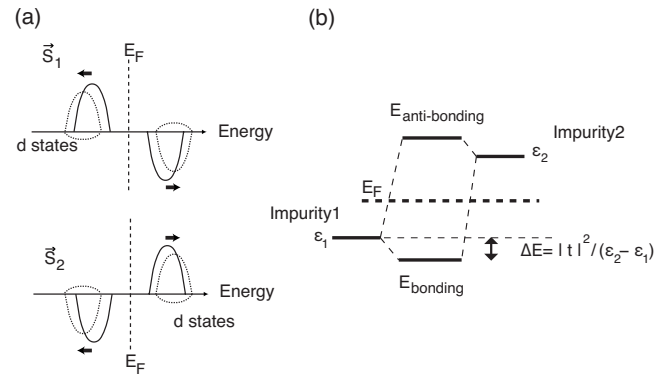

FIG. 24. Schematic diagram of the electronic structure in the case of superexchange. (a) Schematic diagram of the DOSs of two antiparallel-aligned impurity systems 1 and 2 with equal concentrations $c/2$. The full lines show the LDOS without hybridization between the antiparallel-aligned impurity systems; the dotted lines refers to the LDOS that includes the hybridization effects. (b) Schematic of the hybridization-induced energy gain ΔE of Eq. (21) for a diatomic system with unperturbed levels $\epsilon_1 < \epsilon_2$. t is the hopping matrix element between the impurity states.

Figs. 22 and 23, resulting in the suppression of the superexchange interaction. This point will be discussed in the next section.

4. Superexchange mechanism

Superexchange (Goodenough, 1955; Kanamori, 1959) is different from the two mechanisms discussed above, since it does not require a finite density of states at E_F, i.e., it can also occur in an insulator. As a matter of fact, it is most often observed in insulating magnets. The reason for this is that it is related to the hybridization of two types of state, one energetically localized well below and the other one well above E_F. Note that superexchange is usually explained by magnetic coupling transferred by ligands, i.e., the *p* orbitals of the anions. In DMS materials the situation is considerably simplified if we take the impurity gap states as elementary units which hybridize with each other and transfer the coupling. Of course, these states themselves are hybrids between impurity *d* states and anion *p* states, but for understanding the coupling this is of secondary importance.

An illustrative example is plotted in Fig. 24(a) and shows the schematic density of states for two impurity systems with moments $\mathbf{S}_1$ and $\mathbf{S}_2$ that are antiparallel aligned and have equal concentrations $c/2$. Since the electronic states with the same spin direction hybridize with each other, the lower, occupied, energy peaks are shifted to lower energies and the higher, empty, ones to higher energies as indicated by the dotted bands. Because of the downward shift of the lower occupied level, band energy is gained which stabilizes the antiferromagnetic coupling.

The basic mechanism can be understood from a molecular model with two atomic states with different energies $\epsilon_1 < \epsilon_2$ and a hopping matrix element t; this situation is shown in Fig. 24(b). Due to hybridization the molecular levels are given by

$$\epsilon_\pm = \tfrac{1}{2}(\epsilon_1 + \epsilon_2) \pm \sqrt{\left[\tfrac{1}{2}(\epsilon_1 - \epsilon_2)\right]^2 + |t|^2}. \tag{20}$$

If only the lower level ϵ_1 is occupied and moreover $|t| \ll \tfrac{1}{2}(\epsilon_1 - \epsilon_2)$, the binding energy $\Delta E = \epsilon_+ - \epsilon_1$ is given by

$$\Delta E \cong |t|^2/(\epsilon_2 - \epsilon_1). \tag{21}$$

When applied to the above two impurity systems with opposite moments and concentrations $c/2$ the energy gain per Mn atom for antiferromagnetic coupling is given by

$$\Delta E_{\mathrm{SX}} \cong c|t|^2/(\epsilon_{t_{2g}}^\uparrow - \epsilon_{t_{2g}}^\downarrow), \tag{22}$$

where t refers to the hopping element between the impurity t_{2g} states on neighboring sites and the denominator gives the splitting between the majority and minority t_{2g} levels. The linear c factor arises from the fact that the effects of several impurities, coupled antiferromagnetically to the aligned one, are superimposed on each other. Since there are $c/2$ such impurities, and since the energy is gained in both spin directions, a prefactor c appears.

The superexchange interaction is independent of the position of the Fermi level, as long as this lies between the two impurity bands in Fig. 24(a). If it enters these bands, for example, the lower one, it decreases, roughly by a factor of 2 if the Fermi level lies in the middle of the band, and it vanishes if E_F lies below this band. Thus, if the Fermi level lies in the band, there is a competition between double exchange and superexchange, which is usually dominated by the double exchange, resulting in ferromagnetism [see the discussion of (Ga,Mn)N below], except when E_F approaches the up-
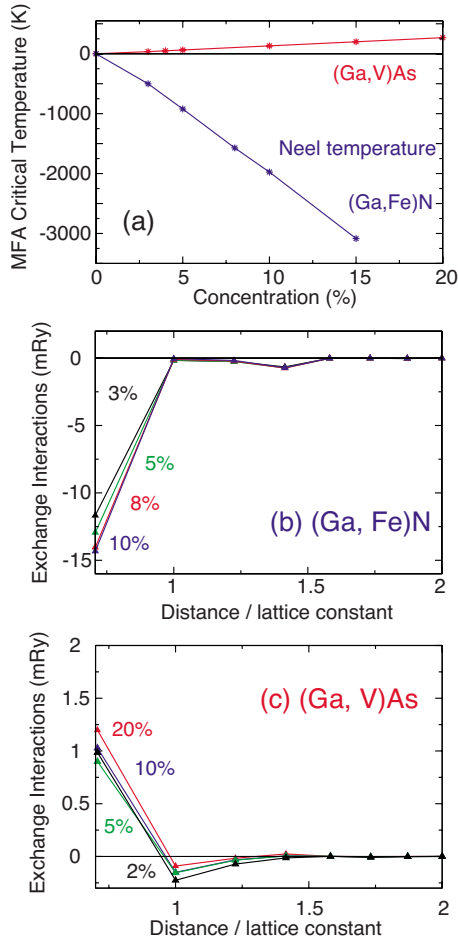
FIG. 25. (Color online) Mean-field Curie temperature T_C^{MFA} and exchange coupling constants J_{ij} for (Ga,Fe)N and (Ga, V)As. (a) T_C^{MFA} as a function of impurity concentration c. (b) J_{ij} for the Fe-Fe coupling in (Ga,Fe)N for various concentrations as a function of distance. (c) J_{ij} for the V-V interaction in (Ga,V)As. From Belhadji *et al.*, 2007.

per band for example, where superexchange takes over, destroying the ferromagnetism. Examples for magnetically disordered DMS materials due to superexchange are Mn in II-VI compounds such as ZnSe or CdTe and Fe in III-V compound semiconductors.

Superexchange represents a rather strong interaction since the t_{2g}-t_{2g} overlap can be rather large. This is also true for wide-gap semiconductors, where the interaction is very short ranged, similar to double exchange. A typical feature for superexchange is that it strongly depends on the exchange splitting $\epsilon_{t_{2g}}^{\uparrow}$-$\epsilon_{t_{2g}}^{\downarrow}$. While in LDA this is given by IM_{loc}, i.e., the exchange integral I times the local moment M_{loc}, in LDA+U this is given by the, usually considerably larger, Hubbard U parameter. Hence the large U enters the denominator of Eq. (22). For materials where the effect of U is important it is clear that the LDA can seriously overestimate the superexchange mechanism, as demonstrated below.

In the mean-field approximation the Curie temperature is given by Eq. (13) where $\Delta\epsilon$ is the energy difference per Mn impurity between the DLM and the ferro-
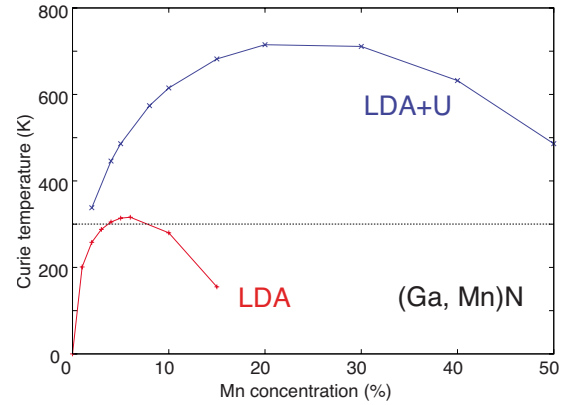

FIG. 26. (Color online) Curie temperature of (Ga,Mn)N in the mean-field approximation calculated using the LDA and the LDA+U method.

magnetic phases. Due to Eq. (22) for superexchange, we expect for (Ga,Fe)As or (Ga,Fe)N a linear dependence of T_c^{MFA} on concentration c with a negative slope, a behavior which is indeed found in *ab initio* calculations [see Fig. 25(a)] for (Ga,Fe)N. Negative values of the ordering temperature from Eq. (13) can be interpreted as positive Néel temperatures. The calculated exchange coupling constants J_{ij} obtained with Eq. (9) are plotted in Fig. 25(b) for Fe-Fe interactions in (Ga,Fe)N with an Fe concentration of 5%. One observes that the interaction is restricted to the nearest neighbors, and that, moreover, the interaction is to a good approximation independent of concentration, which is different from the case of double or p-d exchange. This can be understood from Eq. (14). Since $\Delta\epsilon$ is linear in c and given by $cJ_0=c\Sigma_{j\neq 0}J_{0j}\cong 12cJ_{01}$, where J_{01} is the nearest-neighbor coupling constant in the fcc Ga-sublattice of zinc-blende GaN, the coupling constant J_{01} should be independent of concentration. Physically, the decisive occupied majority $t_{2g}^{\uparrow}$ band is broadened by concentration, which, however, does not affect the energy gain, since the state is fully occupied. For the same reason, in calculations for disordered systems, where we do not make the CPA, one finds a much weaker dependence of the nearest-neighbor coupling J_{01} on disorder effects compared to double-exchange systems (Sato *et al.*, 2007b).

As an illustrative example we discuss the importance of superexchange for a system that is otherwise dominated by double exchange, namely, (Ga,Mn)N. Even for undoped samples superexchange plays a role here, since the responsible majority t_{2g} band is only 2/3 filled, such that superexchange has about 2/3 of its maximal value. The calculated Curie temperatures T_C in MFA are plotted in Fig. 26, based on both LDA and LDA+U calculations (for U=4 eV). In the LDA-case for small concentrations double exchange dominates T_C^{MFA} due to the $\sqrt{c}$ dependence; however, for larger concentrations the linear c dependence of superexchange strongly reduces the MFA values, which become negative for $c\gtrsim 20\%$, indicating a DLM state for large concentrations (Sato *et al.*, 2006). Thus, because of the $\sqrt{c}$-behavior, the bandwidth
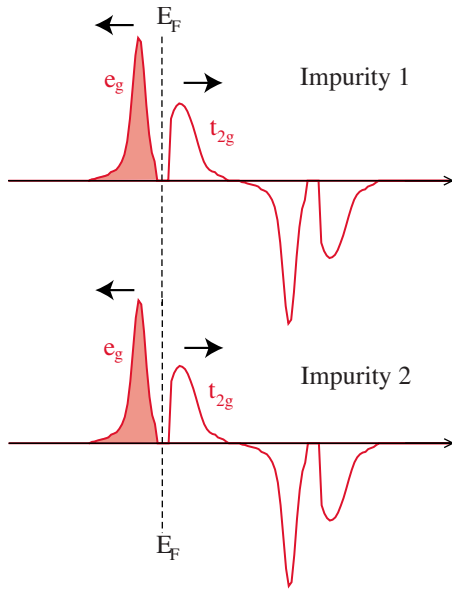
FIG. 27. (Color online) Schematic diagram of the spin-polarized DOS of two V impurities in ferromagnetic (Ga,V)As. From Belhadji *et al.*, 2007.

cannot grow for larger concentrations strongly enough to overcome superexchange. However, in the LDA+U calculation superexchange is strongly reduced and ferromagnetism also dominates for larger concentrations. Thus, the effect of the Hubbard U is quite dramatic in this case. However, these large changes refer only to the MFA. More realistic Monte Carlo calculations give much smaller differences.

5. Ferromagnetic superexchange

Superexchange, as discussed in the last section on a density-functional basis, can also favor ferromagnetism. A general discussion about when to find ferromagnetism or antiferromagnetism, from the superexchange interaction, is summarized in the Kanamori-Goodenough rules. A discussion of these rules can, be found in Goodenough (1955) and Kanamori (1959). For the present discussion we consider the case when the Fermi level falls between the majority $e_g^\uparrow$ state and the majority $t_{2g}^\uparrow$ state, which is the case for (Ga,V)As or, in the case of minority states, for (Zn,Co)O. The first case is shown in Fig. 27. Here the orbitals of the occupied majority $e_g^\uparrow$ level of the first impurity atom, which we call impurity 1, hybridize with empty majority $t_{2g}^\uparrow$ orbitals of the neighboring impurity atom, which we call impurity 2, and vice versa. As a result of the hybridization the occupied $e_g^\uparrow$ orbitals are slightly shifted to lower energies, in this way stabilizing ferromagnetism by superexchange. Quite analogous to the previous result [Eq. (22)], for ferromagnetic superexchange the energy gain is given by

$$\Delta E_{SX} = 2c|t|^2/(\epsilon_{t_{2g}}^\uparrow - \epsilon_{e_g}^\uparrow), \qquad (23)$$

where t is the hopping matrix element between the $e_g^\uparrow$ state and the $t_{2g}^\uparrow$ state on the neighboring impurity, which

is expected to be considerably smaller than the t_{2g}-t_{2g} hopping, since the e_g orbitals are more localized. (For the same reason, double exchange resulting from the broadening of the e_g band, i.e., the e_g-e_g hopping, is very weak and practically negligible.) However, the smallness of the e_g-t_{2g} hopping element is partially balanced by the denominator $\epsilon_{t_{2g}}^\uparrow$-$\epsilon_{eg}^\uparrow$, representing the relatively small crystal field splitting, and by the factor of 2 in Eq. (23). For the case of (Ga,V)As the mean-field Curie temperatures are shown in Fig. 25(a), demonstrating that in DMS systems ferromagnetic superexchange is indeed considerably smaller than antiferromagnetic superexchange, which is relevant, for (Ga,Fe)N. The ferromagnetic coupling constants corresponding to the V-V interaction in (Ga,V)As are shown in Fig. 25(c). The interactions are rather weak and short ranged. For the same reason as for the Fe-Fe interactions in (Ga,Fe)N they depend only slightly on concentration. Another analogy to antiferromagnetic superexchange is the strong dependence on Hubbard U effects. Since the occupied states are pushed to lower energies and unoccupied states to higher energies with increasing U, the crystal field splitting will increase and ferromagnetic superexchange will decrease dramatically.

6. Universal behavior of exchange interactions in DMSs

In the past, self-consistent *ab initio* calculations of the exchange coupling constants have been performed for a large number of DMS systems using the LMTO-CPA or KKR-CPA method in connection with Eq. (9) for the coupling constants (Bergqvist *et al.*, 2004; Fukushima *et al.*, 2004; Kudrnovský *et al.*, 2004; Sato, Schweika, *et al.*, 2004; Sato *et al.*, 2007a). Calculations show, however, that the trends of the exchange interactions can be seen more clearly if the integrand in Eq. (9) is evaluated self-consistently, while the Fermi level is varied artificially over the band-gap region.

To some extent, this is a good approximation for the electronic structure for doped materials. Unfortunately, this approximation cannot be justified with the magnetic force theorem, since the charge is changed by the change in E_F. On the other hand, the topology of the impurity states, i.e., the sequence of e_g states lying below the t_{2g} states and that majority states are below the minority states is always the same, basically determines the exchange mechanisms, and therefore this approximation is justified. This is also shown by the similarity of the results obtained on the basis of self-consistent calculations for different DMS systems. Figures 28(a)–28(c) show the results obtained for (a) (Ga,Mn)N, (b) (Ga,Mn)As, and (c) (Ga,Fe)N. While these results are based on LDA calculations, Fig. 28(d) shows in addition the (Ga,Fe)N results as obtained by the LDA+U method with $U=4$ eV. In all cases an impurity concentration of 5% is assumed. The dashed line shows the local density of states of the impurity, while the full line denotes the exchange integral $J_{01}(E_F^*)$ for the first-nearest neighbors as a function of the artificially varied Fermi level E_F^*. First we see that the structures of
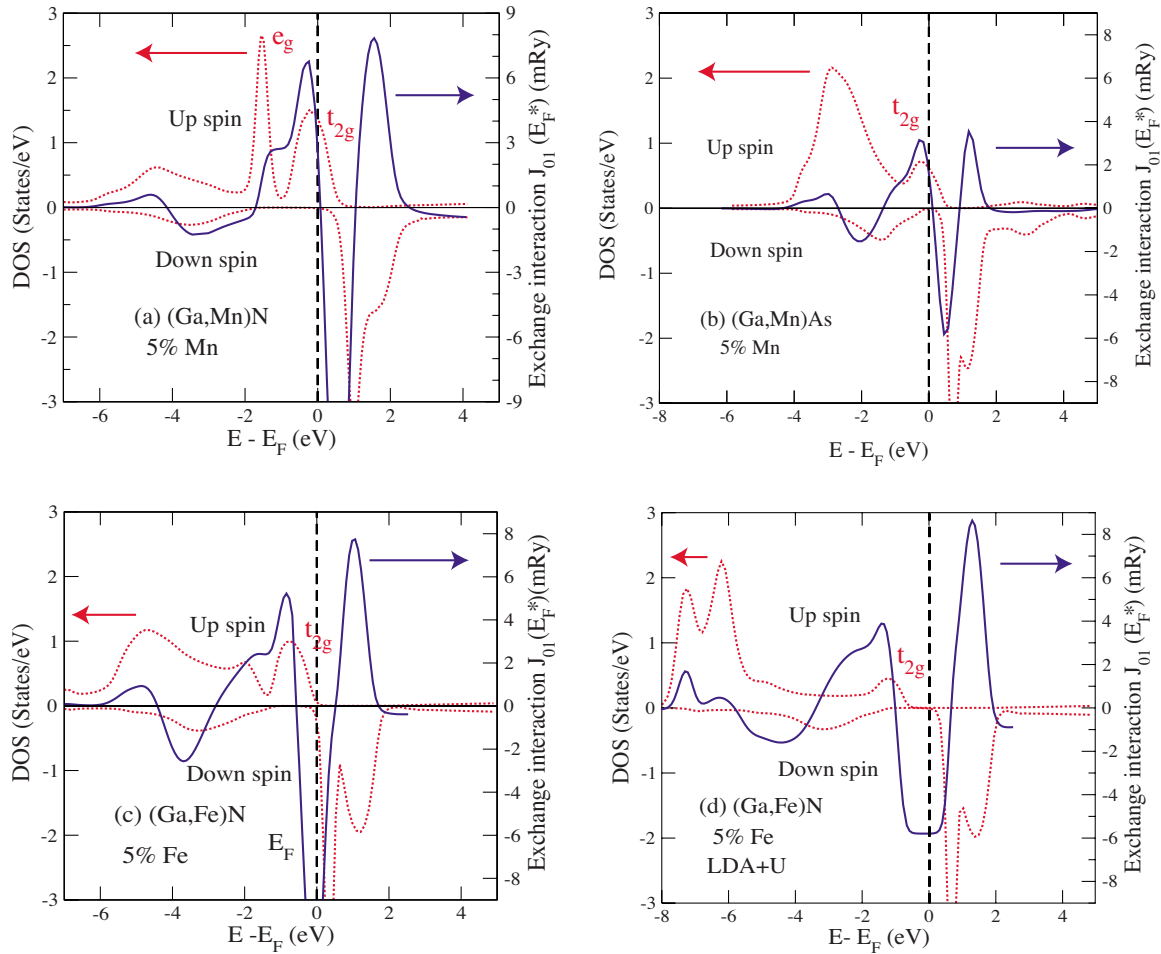
FIG. 28. (Color online) Spin-polarized local DOS of an impurity in a DMS material (dashed curves, left scale) as a function of $E-E_F$. Exchange coupling constant $J_{01}(E_F^*)$ for nearest-neighbor impurities (full curve, right scale) as a function of an arbitrary change in E_F^*. (a) 5% Mn in (Ga,Mn)N, (b) 5% Mn in (Ga,Mn)As, (c) 5% Fe in (Ga,Fe)N (LDA method), and (d) 5% Fe in (Ga,Fe)N (LDA+U with $U=4$ eV). From Belhadji *et al.*, 2007.

the impurity bands are in all cases similar and that the same is also true for the $J_{01}(E_F^*)$ curves, which basically follow the DOS structures. Of course, we should expect this from the previous discussions, since, double exchange should dominate in the t_{2g} bands, while antiferromagnetic superexchange should prevail between the majority and minority t_{2g} states.

Starting with (Ga,Mn)N we obtain a small positive (ferromagnetic) contribution from the bottom of the valence p band and small negative values in the upper part of the band. At the bottom of the conduction band we have small negative values. However, all these values are small compared to the values from the impurity bands. Within the lowest of these, the majority $e_g^\uparrow$ band, the exchange interaction is ferromagnetic and strongly increases to a maximum at the upper edge of this impurity band and a plateau value between the $e_g^\uparrow$ and $t_{2g}^\uparrow$ states. These interactions are due to ferromagnetic superexchange, arising from the hybridization of the $e_g^\uparrow$ states with the $t_{2g}^\uparrow$ states on the neighboring sites. Within the $t_{2g}^\uparrow$ band we obtain a strong double-exchange contribution stabilizing ferromagnetism due to the hybridization-

induced broadening of the $t_{2g}^\uparrow$ band. However, in the middle of the $t_{2g}^\uparrow$ band the ferromagnetic exchange coupling already decreases as a result of the strong superexchange resulting from the hybridization of the $t_{2g}^\uparrow$ and $e_g^\downarrow$ states on neighboring sites. The maximum of the antiferromagnetic coupling occurs between the centers of the $t_{2g}^\uparrow$ and $e_g^\downarrow$ bands.

The curve then increases due to ferromagnetic superexchange between the $e_g^\downarrow$ and $t_{2g}^\downarrow$ orbitals and becomes positive due to double exchange in the t_{2g} bands, reducing to small negative values when the t_{2g} band is filled. The trends for Fe in GaN [Fig. 28(c)] are much the same. For (Ga,Mn)As we observe an interesting variation arising from the downward shift of the $e_g^\uparrow$ and $t_{2g}^\uparrow$ levels into the valence band. Below the $t_{2g}^\uparrow$ double-exchange peak we see a small shoulder, reminiscent of the $e_g^\uparrow$-$t_{2g}^\uparrow$ ferromagnetic superexchange mechanism. This shoulder is more clearly seen in (Ga,Fe)N, where the $e_g^\uparrow$ peak can still be seen in the DOS.

Finally, Fig. 28(d) shows the resulting DOS curve and the exchange interactions for (Ga,Fe)N calculated in the LDA+U with a U value of 4 eV. One observes a much

larger exchange splitting of the spin-polarized DOS accompanied by a strong reduction of antiferromagnetic superexchange, as discussed in Sec. III.C.4. In fact the self-consistent $J_{01}(E_F)$ value for the Fe–Fe nearest neighbors is reduced from -13 to -6 mRy, a quite remarkable effect.

Thus we see that the exchange interaction curve follows the DOS curves closely and therefore shows a universal behavior for all wide-gap DMSs with zinc-blende structure. Realistic calculations for a given material can be difficult and depend on correlation properties like the value of the band gap and the Hubbard U parameter; however, the trends of the exchange interactions are universal and can be explained by the simple description of the exchange interactions presented here (Belhadji *et al.*, 2007).

D. Exchange integrals and Curie temperature in dilute magnetic semiconductors

The pair exchange interaction between two different magnetic ions is a relevant characteristic of the magnetic state. Knowledge of this interaction allows one to estimate such important quantities as Curie temperature, spin stiffness, or magnon spectra. In addition, interatomic exchange or exchange integrals allow one to draw important conclusions concerning the stability of the magnetic state. The exchange interactions can also be obtained by fitting to experimental data, for example, the magnon spectra. Here we describe how they are determined on the basis of a parameter-free approach with a predictive potential.

It is important to note that in real systems, depending on the symmetry of the lattice, the lattice constant, the electronic character of the magnetic atoms, and other impurities doping the host and their concentrations, several of the mechanisms discussed above may play a role. The advantage of first-principles theory is that the mechanisms are included in the calculated exchange interactions in a mixture dictated by the calculation. The advantage of a first-principles calculation of the materials properties of a DMS is, at the same time, also its disadvantage, as it is difficult to identify the particular contribution of any of the relevant mechanisms of the exchange interactions discussed above. In this sense the role of models is indispensable.

The Anderson Hamiltonian (Anderson, 1961), in particular its two-impurity version (Shi *et al.*, 1994), is suitable for a qualitative discussion of the character of exchange interactions obtained from first principles for systems with low-impurity concentrations. In the framework of a Green's function approach, hybridization of local moments with host electrons is included to all orders of the perturbation theory with respect to the strength of the hybridization, thus going beyond the weak-coupling (RKKY) theory. One of the novel, relevant features is the influence of impurity perturbation on the host band structure, which is neglected in the conventional RKKY model. This influence is particularly strong if there is a virtual bound state close to the

Fermi energy of the host material. The main result of such a model study (Shi *et al.*, 1994) is that the exchange interaction has RKKY-like and superexchange contributions. The former is related to the host Fermi surface and the main difference from the conventional model (for example, Mn impurities in a fcc Cu host) is the small size of the host Fermi surface (due to the small carrier concentration), which results in a large period of the damped oscillations of exchange interactions as a function of the distance between impurities. Nevertheless, the ferromagnetic coupling can extend over distances comparable to or even larger than the distance between Mn impurities and thus it stabilizes the ferromagnetism in some of these systems. It should be noted that there is a pronounced anisotropy of the exchange interactions due to the lattice structure. In real systems the oscillatory character of the exchange interactions is usually strongly suppressed by finite impurity concentrations and, most importantly, by developing half-metallic behavior of the DMS alloy. This, in turn, is a direct consequence of the presence of a band gap in the host alloy.

The last point opens naturally a question concerning the relevance of the size of the band gap for the evaluation of exchange integrals, as its value is underestimated in the LDA, typically by $\sim 0.5-1$ eV. The superexchange interaction is particularly sensitive to the actual size of the band gap, as is obvious from its microscopic mechanism, discussed above (with no free carriers). It is, however, interesting to note that the superexchange mechanism can also influence exchange interactions in DMS alloys like Mn-doped GaAs with a finite free-carrier concentration. One important qualitative conclusion of Shi *et al.* (1994) is that superexchange becomes increasingly important if there are empty impurity states available close to the Fermi energy. Because the superexchange interaction is short ranged and antiferromagetic, it will mostly influence the nearest-neighbor exchange interactions which, in turn, only have a weak influence on the Curie temperature because of percolation effects. This effect is seen in Fig. 29: an increased concentration of As antisites moves the Fermi energy toward the available empty minority Mn impurity subband and thus predominantly reduces the nearest-neighbor $J_1^{\mathrm{Mn,Mn}}$ ferromagnetic exchange interaction as explained above. One can thus conclude that the size of the band gap has a weaker effect on exchange interactions when free carriers are present, whose increasing concentration pushes the Fermi energy deeper into the valence band.

It should be noted that the picture drawn from a simple two-site Anderson model gives an indication of the relevance of various mechanisms (here the indirect exchange and superexchange) as estimated by the first-principles calculation. A more quantitative way of identifying various contributions from calculated exchange integrals still remains a challenge for first-principles theory (see also Sec. III.C).

In principle, all relevant quantities could be obtained from knowledge of the temperature-dependent dynamical susceptibility of the system but calculations of this
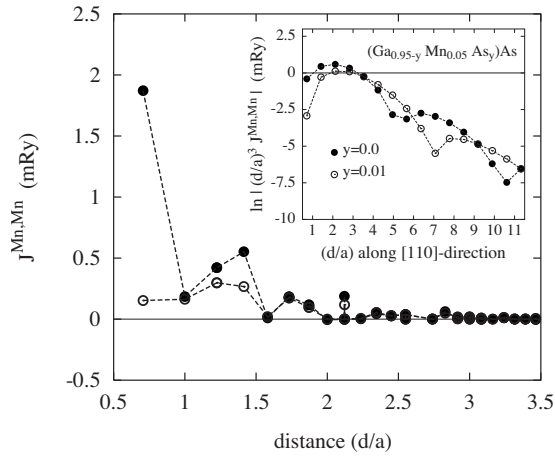
FIG. 29. Exchange interactions in $(Ga_{0.95-y},Mn_{0.05},As_y)As$ without ($y=0$) and with As antisites ($y=0.01$). The exponential decay of these interactions with distance along the dominating [110] direction is shown in the inset (see text).

property from first-principles theory and for diluted random systems are not feasible at the moment. Instead, a two-step approach originally proposed by Liechtenstein *et al.* (1987) and Antropov *et al.* (1999) is often employed and we discuss its generalization to random systems. The reliability of such an approach for a broad class of magnetic systems, namely, the transition-metal ferromagnets, *f* magnets, ordered Heusler alloys, random transition-metal alloys, diluted magnetic systems, magnetic overlayers on nonmagnetic substrates, and magnetic surfaces has been demonstrated recently (Turek *et al.*, 2006).

1. General considerations

In the framework of the two-step approach, one may obtain an explicit expression for the averaged exchange interaction $\bar{J}_{ij}^{Q,Q'}$ between two magnetic ions Q and Q' located at lattice sites i and j. As pointed out in Sec. III.A, the calculations of J_{ij} are based on a number of approximations, which we discuss here in more detail.

(i)   The adiabatic approximation is based on the fact that the time scale of transverse fluctuations (magnons) is much slower than that for electron hopping so that the electron system can relax in the presence of magnons. Usually the density of low-lying magnon excitations is much higher than that of longitudinal ones (Stoner excitations) and the former are thus responsible for the reduction of magnetization with temperature. This is true in particular for systems with well-defined magnetic moments such as Mn, Fe, or Cr.

(ii) The magnetic force theorem (Oswald *et al.*, 1985; Liechtenstein *et al.*, 1987; Antropov *et al.*, 1999), which is based on the variational character of the local-density approximation, allows one to estimate changes of the total energy connected with small (rigid) rotations of magnetic moments from

the known properties of the ground state, typically from the ferromagnetic state or the disordered local moment state. The change in the total energy is then equal to the corresponding change in one-particle energies.

(iii) The change in one-particle energies due to a localized perturbation (for example, small rotations of spins at sites i and j) can be effectively evaluated in the framework of the Green's function approach (Liechtenstein *et al.*, 1987; Antropov *et al.*, 1999; Turek *et al.*, 2006) by a Friedel-sum-rule type of expression well known in the solid-state physics community (Kittel, 1987), which has been generalized to the case of two perturbations (also known as the Lloyd formula).

(iv) The CPA performs a proper configurational average and one can obtain configurationally averaged exchange interactions. The averaging is significantly simplified using the vertex-cancellation theorem which is based on the variational property of the CPA (Bruno *et al.*, 1996) and which allows us to neglect the disorder-induced vertex corrections occurring during the evaluation of exchange integrals in random systems [see Bruno *et al.* (1996) for more details].

(v)   The exchange integrals used for estimating the Curie temperature T_C should be optimally evaluated at this same temperature while calculations in practice are usually performed for $T=0$ K. This introduces some error to the estimate of T_C; this is negligible, however, at least for calculations of ordering temperatures close to room temperature. The electron correlations can also influence the values of exchange integrals (Katsnelson and Lichtenstein, 2000), and we estimate their possible effect in the framework of the LDA+U approach (Dudarev *et al.*, 1998; Sandratskii *et al.*, 2004; Shick *et al.*, 2004; Wierzbowska *et al.*, 2004). Finally, using the Heisenberg model, higher-order interactions, for example, four-spin interactions like biquadratic coupling, are neglected.

The procedure described above allows us, as a first step, to construct an effective classical random Heisenberg Hamiltonian which, in a second step, is studied by methods of statistical physics. The separate treatments of the electron and statistical degrees of freedom form in fact the main advantage of this approach, as sophisticated treatments of both spin fluctuations and the randomness of the system are possible, both of which are features of key importance for a reliable estimate of the Curie temperature.

2. Formalism

Here and in Sec. III.D.4 we discuss in some detail the asymptotic behavior of the exchange interactions for large distances R_{ij} between two impurities. While in the previous section we discussed the mean-field behavior of

DMSs, which is determined by the sum $\Sigma_j J_{ij}$ of the exchange integrals, the asymptotic behavior is another charcateristic property of the interaction that can be studied semianalytically. The resulting formula, given below, is usually valid qualitatively also in the preasymptotic region.

In the limit of large distances R_{ij} between atoms i and i, Eq. (9) can be evaluated analytically by means of the stationary phase approximation. We obtain (Pajda *et al.*, 2001; Kudrnovský *et al.*, 2004; Turek *et al.*, 2006)

$$\bar{J}_{ij}^{\mathrm{Mn,Mn}} \propto \exp(-\boldsymbol{\lambda}_{ij}^{\uparrow} \cdot \mathbf{R}_{ij})\exp(-\boldsymbol{\kappa}_F^{\downarrow} \cdot \mathbf{R}_{ij})$$
$$\times \frac{\sin(\mathbf{k}_F^{\downarrow} \cdot \mathbf{R}_{ij} + \Phi^{\uparrow} + \Phi^{\downarrow})}{R_{ij}^3}. \tag{24}$$

The quantity $\mathbf{k}_F^{\sigma}$, which characterizes the period of oscillations, is the Fermi wave vector, which points in such a direction that the associated group velocity $\nabla_{\mathbf{k}} \bar{E}^{\sigma}(\mathbf{k}_F)$ is parallel to $\mathbf{R}_{ij}$. Because of the disorder, the band energy $\bar{E}^{\sigma}(\mathbf{k})$ consists of a real part corresponding to the spin-dependent self-energy at the Fermi energy (determined within the CPA) and an imaginary part characterizing the damping $\boldsymbol{\lambda}_{ij}^{\sigma}$ in (typically) majority spin bands. The damping due to disorder in realistic systems is anisotropic inside the Brillouin zone (Turek *et al.*, 1997), the factor $\boldsymbol{\lambda}_{ij}^{\uparrow}$ therefore depends on the directions of $\mathbf{R}_{ij}$ and $\mathbf{k}$. Such a damping also determines the carrier lifetime which enters the corresponding transport equations. The effect of disorder on both the exchange interactions and the resulting thermodynamic properties, as well as on the transport properties, is thus described by the same unified approach. This feature is missing in most model approaches as well in the supercell description, discussed below. Due to the half-metallic character of typical DMS alloys, the corresponding critical Fermi wave vector $\mathbf{k}_F^{\downarrow}$ of the minority states is complex (here purely imaginary), i.e., $\boldsymbol{\kappa}_F^{\downarrow} = \mathrm{Im}\, \mathbf{k}_F^{\downarrow}$. This situation is similar to that studied by Pajda *et al.* (2001) for strong ferromagnets with a fully occupied majority band. Finally, $\Phi^{\uparrow}$ and $\Phi^{\downarrow}$ phase factors arise from the scattering at the impurities. For the alloy case we thus find an exponential decrease in $\bar{J}^{\mathrm{Mn,Mn}}$ with distance, arising from (i) a damping due to substitutional disorder which was predicted by de Gennes (1962), and (ii) an additional damping due to the half-metallic character of the DMS alloys. The damping due to disorder involves configurationally averaged exchange interactions whereby exchange interactions for given alloy configuration can exhibit a slower decay with distance (Levy *et al.*, 1998). The large size of the experimental samples leads to a self-averaging effect, such that the averaged interactions directly determine, for example, Curie temperatures, spin stiffness, or spin-wave spectra.

It is interesting to consider the low concentration or the RKKY limit of the general expression, i.e., for two magnetic impurities in a nonmagnetic host. Due to the weak scattering assumed in the RKKY expression the prefactors and postfactors in Eq. (8) are neglected and

the spin-dependent CPA Green's function is replaced by the spin-independent Green's function of the nonmagnetic host crystal. Thus the renormalization of the host Green's function due to impurity scattering is twofold: (i) it introduces a phase factor and modifies the amplitude of the oscillations as compared to the conventional RKKY formula (Blackman and Elliott, 1969), and (ii) it leads, as mentioned, to significant modifications of the values of the exchange integrals (Shi *et al.*, 1994; Bouzerar, Bouzerar, and Ziman, 2006) in the preasymptotic regime, relevant in the present case.

Thus, the qualitative properties of exchange integrals in diluted magnetic systems can be characterized as follows: (i) the exchange interactions are exponentially damped with distance due to the presence of disorder and the half-metallic character of these alloys; (ii) because of the presence of lattice and anisotropic properties of the alloy damping, the exchange integrals exhibit a strong directional character; (iii) the basic properties of exchange interactions are due to the Fermi surface topology, which in turn depends on the carrier number, a robust quantity in the CPA; and (iv) individual exchange interactions could depend strongly on the local environment. Such fluctuations are, however, strongly suppressed when each configuration is properly weighted by its probability in random alloys. Properly averaged interactions are quite close to their CPA counterparts (Ruban *et al.*, 2005).

3. Alternative approaches

We mention here alternative approaches to evaluating exchange interactions, which are based on the supercell geometry, simulating the random alloy. There are essentially two ways in which to model the small but finite impurity concentration of magnetic defects in DMS alloys using supercells. The first approach considers a single magnetic impurity inside a cell whose dimensions are varied to fit a given concentration (for example, a supercell of 64 atoms, of which 32 are Ga atoms, with a single Mn impurity replacing a Ga atom, simulates an effective Mn concentration of 3.125%). One then applies the frozen magnon (spin-spiral) approach generalized to supercells while the exchange interactions are obtained by an inverse Fourier transformation from the calculated magnon spectra (Sandratskii and Bruno, 2002). In this way, one can determine a subset of all possible exchange interactions among magnetic impurities which are on positions corresponding to the average distance between them in the alloy. This has some advantages for the mean-field (MF) treatment of the Curie temperature, because the dominating first-nearest-neighbor interactions are avoided. On the other hand, disorder effects are completely neglected.

As an alternative, one can employ supercells of a fixed size but with a few impurity atoms distributed inside a large supercell (Mahadevan *et al.*, 2004; Yu *et al.*, 2005). There are two variants of this approach. The first considers a supercell with two atoms, where the size of the supercell simulates a chosen concentration of magnetic
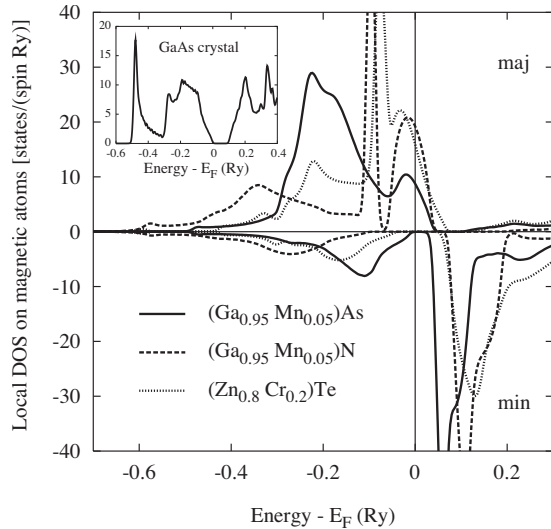
FIG. 30. Local density of states on Mn atoms in $(Ga_{0.95},Mn_{0.05})As$ alloy for majority and minority states. In the inset the host GaAs density of states is shown. For comparison, local densities of states on Mn atoms in $(Ga_{0.95},Mn_{0.05})N$ and on Cr atoms in $(Zn_{0.8},Cr_{0.2})Te$ are also shown.

impurities (Mahadevan *et al.*, 2004). One impurity is placed in the center and the other in different positions inside the supercell. In this way, the first few nearest-neighbor interactions can be extracted by identifying
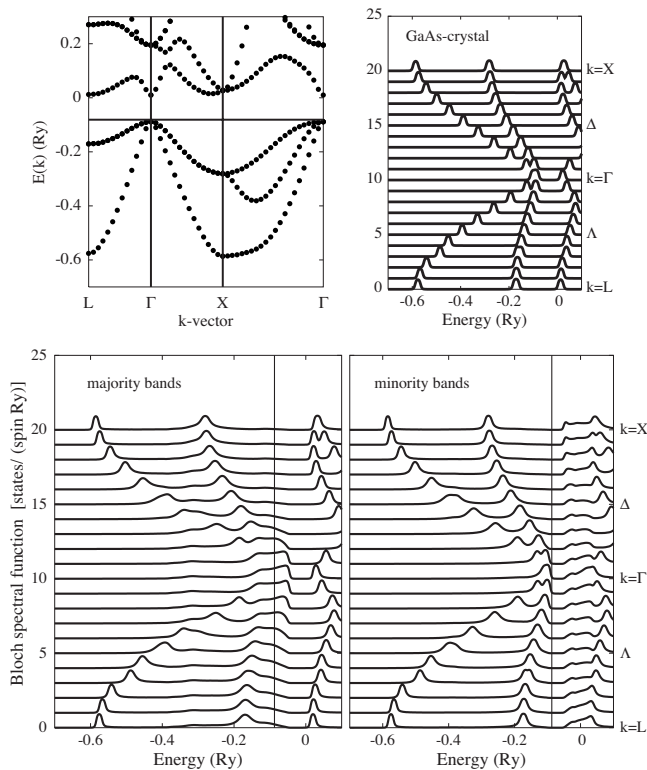

FIG. 31. Bloch spectral functions for majority and minority bands in $(Ga_{0.95},Mn_{0.05})As$ (lower panels). For comparison the host GaAs band structure (left upper panel) and the corresponding Bloch spectral function (right upper panel; a small broadening is used) are shown. In the lower figures, the vertical lines denote the Fermi energy.

them with the energy differences between the parallel and antiparallel impurity spin orientations. In general, a larger number of exchange interactions can be extracted for larger supercells. As an alternative, a large supercell with fewer atoms is used in so-called special quasirandom structures (Yu *et al.*, 2005), i.e., special superlattices designed to reproduce the average occupation of the first few nearest-neighbor shells in an alloy, similar to that found in a random alloy (Zunger *et al.*, 1990). Of course, one can also employ any other set of impurities inside a supercell which can simulate, possible clustering. Instead of one exchange interaction for a given coordination shell, as in the previously discussed approach, one obtains a distribution of interactions for each distance depending on the supercell size and number of impurities. The exchange interactions thus fluctuate around some value, with a magnitude of fluctuations that depends on the supercell size. It is important that this approach requires some kind of configurational averaging of the exchange integrals (Yu *et al.*, 2005). Properly averaged sets can be quite close to the exchange integrals as obtained from the CPA approach described above (Ruban *et al.*, 2005).

4. Examples of first-principles calculations of exchange interactions

In describing results from first-principles calculations, we concentrate mostly on the (Ga,Mn)As alloy, which has been studied most intensively, both theoretically and experimentally. We first discuss the strong influence of disorder due to the TM atoms. We show in Fig. 30 the Mn-projected local density of states for $(Ga_{0.95},Mn_{0.05})As$ and compare it (see inset) with the host GaAs DOS. Note the different shapes of the majority and minority DOSs and the half-metallic behavior of the alloy (the Fermi energy E_F lies in the gap of the minority states). The Mn-projected DOS curves exhibit a virtual bound state behavior and differ strongly in their shape from the host DOS. As explained, this signals a strong disorder in the host introduced by Mn impurities. Similar behavior is observed (see Fig. 30 again) for other typical alloys, namely, $(Ga_{0.95},Mn_{0.05})N$ and $(Zn_{0.8},Cr_{0.1})Te$ (Bergqvist *et al.*, 2005).

Due to disorder the wave vector is no longer a good quantum number and bands as such do not exist. Their function is replaced by the Bloch spectral functions (BSFs), which provide detailed insight into the nature of electron states in disordered alloys (Gonis, 2000). We show as an example the BSF of Mn-doped GaAs in Fig. 31. For a reference, we also show the BSF of pure GaAs together with the corresponding band structure. The alloy BSF clearly exhibits a strong disorder in the minority states above E_F. This is shown by the broad dispersionless bands, as contrasted with sharp peaks moving with the wave vector, which correspond to weakly perturbed bands. Similar behavior is also found close to the top of the valence band in the majority states which demonstrates a strong effect of alloy disorder on the host band structure around the Γ point and the alloy Fermi sur-
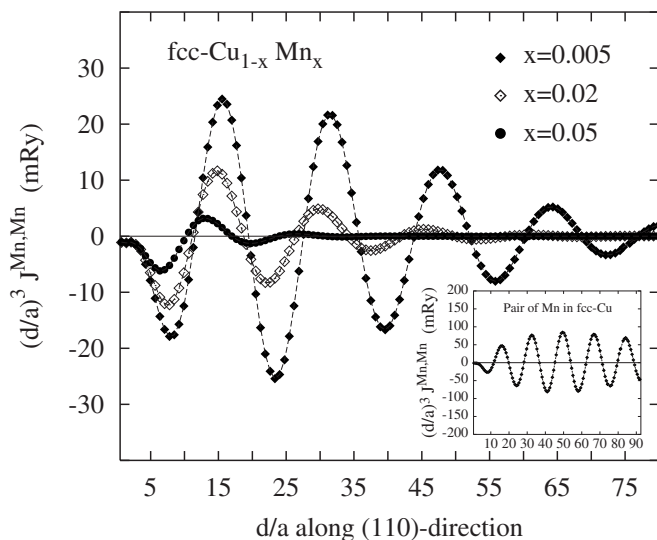
FIG. 32. Exchange interactions along the dominating [110] direction in $Cu_{1-x}Mn_x$ alloys for $x=0.005$, 0.02, and 0.05. Interactions are multiplied by the RKKY-like factor $(d/a)^3$, where d is the distance between two Mn atoms and a is the lattice constant. Corresponding exchange interactions between two isolated impurities in a Cu host are shown in the inset.

face, both of which are relevant to the strengths and values of the exchange couplings.

We have pointed out the combined effect of alloy disorder and half-metallicity on the exchange interactions. We demonstrate their effects separately, taking as examples conventional CuMn and Heusler alloys, as shown in Figs. 32 and 33, respectively. We plot in these figures $(d/a)^3 J^{Mn,Mn}(d/a)$ rather than the bare exchange interactions $J^{Mn,Mn}(d/a)$, in order to demonstrate explicitly their RKKY character as well as the damping with distance due to disorder and the presence of the gap. The reference case of two Mn impurities in Cu in the inset of Fig. 32 shows RKKY-like asymptotic behavior for large distances (up to 90 lattice constants) along the dominating [110] direction as well as strong preasymptotic behavior due to impurity disorder (Blackman and
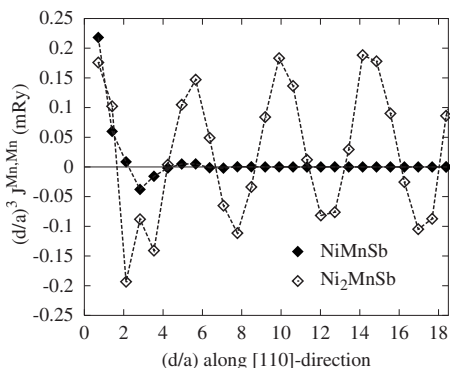

FIG. 33. Exchange interactions along the dominating [110] direction in semi-Heusler (NiMnSb) and Heusler (Ni_2MnSb) alloys, illustrating the effect of half metallicity. Interactions are multiplied by the RKKY-like factor $(d/a)^3$, where d is the distance between two Mn atoms and a is the lattice constant.

Elliott, 1969; Shi *et al.*, 1994; Bouzerar, Bouzerar, and Ziman, 2006). We also observe an exponential damping of oscillations due to alloy disorder [see Eq. (24)], clearly seen in Fig. 32 by comparing the curves for 0.5% and 5% Mn concentration. The calculated periods of oscillation in Fig. 32 agree well with those found in the experiment for interlayer exchange couplings in [110] CoCuCo multilayers (Bruno, 1995). The half-metallicity, i.e., the presence of the Fermi level in the gap of one of the spin subbands, also leads to an exponential damping as seen from Eq. (24). This is shown in Fig. 33 for the half-metallic half-Heusler alloy NiMnSb, where the damping is very strong, while ordinary undamped RKKY-like oscillations are observed for the metallic Heusler alloy Ni_2MnSb (Rusz *et al.*, 2006).

The behavior of exchange interactions as a function of distance between Mn atoms in $(Ga_{0.95-y}, Mn_{0.05}, As_y)As$ alloy without ($y=0$) and with ($y=0.01$) As antisites is shown in Fig. 29. Ferromagnetic (FM) pair interactions are found over rather large distances, comparable to the averaged distance between Mn atoms, which stabilizes the FM state. The presence of As antisites reduces first the dominating first-nearest-neighbor interactions which, for a slightly larger value of y, become antiferromagnetic, leading thus to frustration and the loss of FM order. The number of carriers is also reduced and the smaller size of the Fermi surface leads to a larger period of damped oscillations (as compared to the case $y=0$) which is shown in the inset. We plot in the inset the logarithm of the exchange interaction $|\ln (d/a)^3 J^{Mn,Mn}(d/a)|$ to demonstrate explicitly the exponential damping of exchange interactions with distance, which is due both to the half-metallic character of the alloy (the presence of the gap) and to the disorder.

We now discuss some specific features of exchange interactions in DMS alloys (Kudrnovský *et al.*, 2004), namely, their anisotropy in space, the limited spatial extent, and their concentration dependence. A pronounced directional character of exchange interactions in (Ga,Mn)As alloys is shown in Fig. 34 and it is seen that the [110] direction dominates [which was also found in the related supercell approach (Mahadevan *et al.*, 2004)]. The dominating character of exchange interactions along the [110] direction is even more pronounced in (Ga,Mn)N alloys (see inset).

The spatial extent of exchange interactions of some typical DMS alloys is shown in Fig. 35. We observe a significantly larger spatial extent in (Ga,Mn)As as compared to (Ga,Mn)N, while the (Zn,Cr)Te alloy (Bouzerar, Bouzerar, *et al.*, 2006) is intermediate. Clearly, a localized character of interactions requires a correct treatment of atomic disorder when the Curie temperature is estimated.

The concentration dependence of the exchange interactions in (Ga,Mn)As along the dominating [110] direction is shown as an example in Fig. 36. For larger distances, the observed reduction of the size of the exchange interaction with increasing Mn concentration has essentially two causes (Kudrnovský *et al.*, 2004): (i) a conventional, RKKY-like behavior results in amplitudes
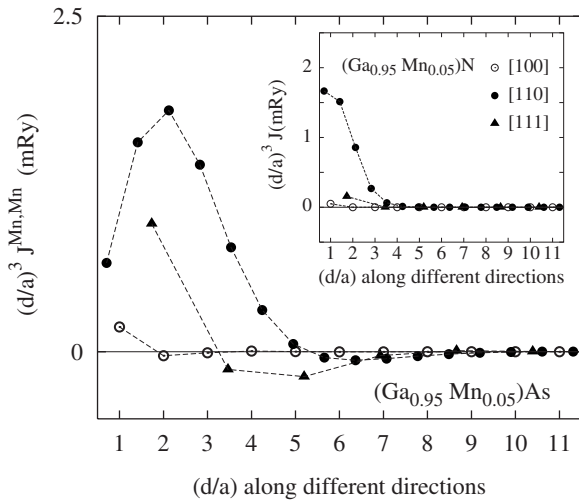
FIG. 34. Exchange interactions in $(Ga_{0.95}, Mn_{0.05})As$ along various directions in real space. A similar dependence for $(Ga_{0.95}, Mn_{0.05})N$ is shown in the inset for comparison.

of oscillations that are inversely proportional to the size of the Fermi surface and hence to the Mn concentration; and (ii) the disorder and half-metallic character of the host semiconductor alloy becomes more pronounced with increasing concentration of Mn impurities, which reduces the size of the exchange interaction. For short distances a strong increase in the coupling with decreasing concentration is observed, which has a different origin and which we attribute to a failure of the CPA; i.e., the neglect of the multiple impurity-impurity scattering events. Clearly, for $x \rightarrow 0$ the impurity interaction should level off to the value in pure GaAs.

The presence of a narrow Mn virtual bound state in (Ga,Mn)As and, in particular, the Mn impurity bands localized inside the gap of the GaN host invoke naturally the question of relevance of electron correlations in such bands and their influence on the exchange interactions. There are few studies of electronic properties of (Ga,Mn)As and (Ga,Mn)N alloys in the framework of the LDA+U approach, employing both supercell (Dudarev *et al.*, 1998; Sandratskii *et al.*, 2004; Shick *et al.*,
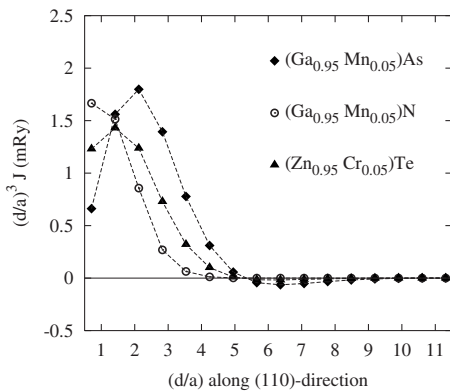

FIG. 35. Exchange interactions for various DMS alloys as a function of the distance d between magnetic impurities (a denotes the lattice constant).
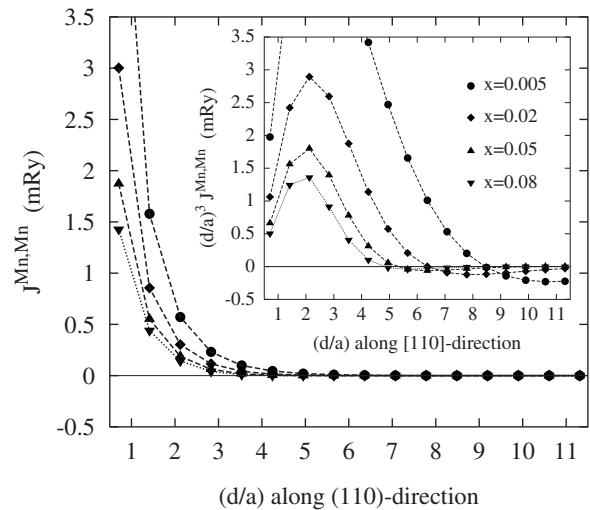

FIG. 36. Concentration dependence of exchange interactions in $(Ga_{0.95}, Mn_{0.05})As$ along the dominating [110] direction. In the inset we show the same dependence but here it is scaled by a RKKY-like factor $(d/a)^3$.

2004) and Green's function methods (Sandratskii *et al.*, 2004; Sato, Dederichs, *et al.*, 2004; Shick *et al.*, 2004). The method of self-interaction corrections (Filippetti and Spaldin, 2003), which avoids the use of empirical parameters (for example, the Hubbard interaction parameter U), was also used but its application seems to be better justified for well-localized impurity subbands [for example, (Ga,Mn)N] (Shick *et al.*, 2004; Schulthess *et al.*, 2007). On the other hand, corresponding estimates of exchange integrals are still rather rare and limited to the LDA+U approach (Sandratskii *et al.*, 2004; Sato, Dederichs, *et al.*, 2004; Kudrnovský *et al.*, 2004).

The dependence of exchange interactions on electron correlations was studied in the framework of the LDA+U method (Kudrnovský *et al.*, 2004; Sandratskii *et al.*, 2004; Sato, Dederichs, *et al.*, 2004) Results for (Ga,Mn)As are shown in Fig. 37 where they are compared to their corresponding LDA counterparts. For Mn a U value of 4.1 eV (with J=1.1 eV) has been used. Electron correlations shift the majority Mn d band to higher binding energies (Sandratskii *et al.*, 2004; Shick *et al.*, 2004), thus weakening the effect of disorder at the Fermi energy. As a result, the damping at E_F is smaller and the half-metallic character weakens, which leads to spatially slightly more extended interactions with better pronounced oscillations (Kudrnovský *et al.*, 2004). This is seen more clearly in Fig. 37(b), where this effect is magnified by multiplication of the exchange interactions by the RKKY factor $(d/a)^3$. On the other hand, the overall character of the exchange interactions remains seemingly unchanged: the exchange interactions are somewhat reduced for smaller distances, but are enhanced and longer ranged for larger distances. As discussed in Sec. III.C.3, these changes result from an important change in the underlying exchange mechanism, which changes from dominating double exchange in the LDA to an increasing degree of *p-d* exchange in the LDA
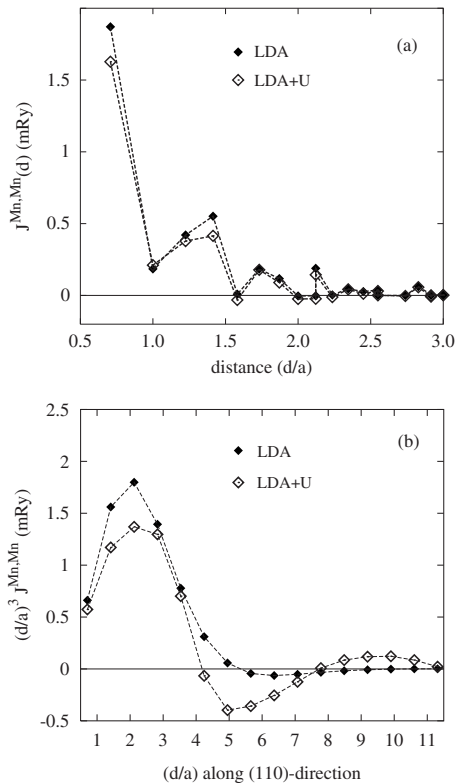
FIG. 37. The effect of electron correlations on exchange interactions in $(Ga_{0.95}, Mn_{0.05})As$. (a) Corresponding exchange interactions evaluated in the framework of the LDA and LDA $+U$ approaches are shown as functions of the distance between Mn atoms. (b) Along the dominating [110] direction the exchange interactions scaled by the RKKY-like factor $(d/a)^3$ are shown. The first four d/a values in (b) correspond to the four maxima at d/a=0.71, 1.41, 2.12, and 2.83 in (a).

FIG. 38. The stability of the ferromagnetic state in $(Ga_{0.95-y}, Mn_{0.05}, As_y)As$ as a function of As antisite concentration y: (a) total energy picture and (b) the lattice Fourier transform of exchange interactions between Mn atoms (see text). The order parameter r characterizes the fraction of spins pointing in a direction opposite to that of the majority of the atoms: values $r=0$ and 0.5 correspond to the ferromagnetic and DLM states, respectively. Other values of r characterize various possible uncompensated DLM states.

$+U$ calculation. Electron correlations in a partly filled Mn impurity band inside the broad gap of (Ga,Mn)N keep the spatial extent of the wave functions localized (Kudrnovský *et al.*, 2004; Sandratskii *et al.*, 2004) and the influence of the percolation effect on the Curie temperature is thus very small.

Until now we have discussed materials with holes in the valence band (*p*-type ferromagnetism). It is therefore interesting to mention the possibility for *n*-type ferromagnetism in DMS alloys which is due to electrons in the conduction band. This problem was recently addressed (Mašek *et al.*, 2007) and it was shown that a possible candidate is the direct-gap Li-rich Li(Zn,Mn)As alloy, where the extra Li atoms act like donors, thus forming an *n*-type alloy.

Knowledge of the exchange interactions also allows one to draw qualitative conclusions concerning the character and the stability of the magnetic state. We illustrate this point for the case of an uncompensated disordered local moment (UDLM) state, which was found to be the ground state in (Ga,Mn)As alloys containing As antisites (Korzhavyi *et al.*, 2002). In the framework of the DLM model (Sato and Katayama-Yoshida, 2002) it is assumed that local atomic moments are randomly oriented in space with an equal probability for each direc-
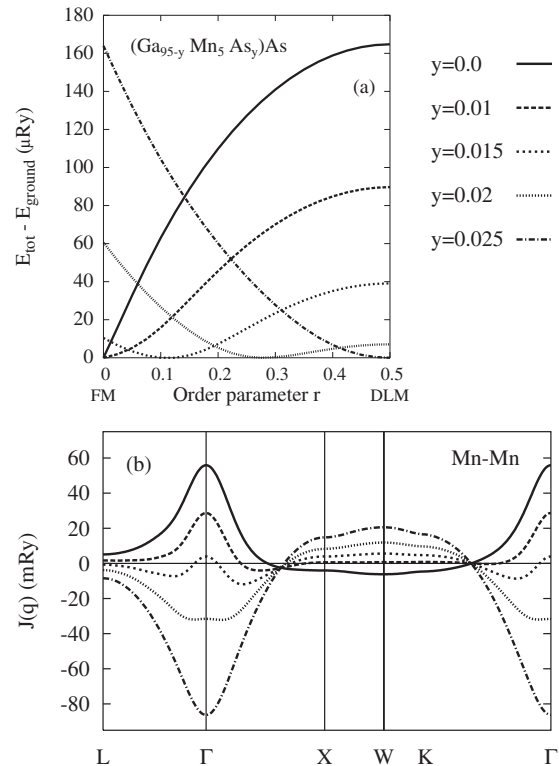
tion. This problem can formally be mapped exactly to the problem of a random "alloy" of collinear spins with antiferromagnetic alignments. This kind of problem can be naturally studied in the framework of the LDA-CPA formalism (Sato and Katayama-Yoshida, 2002). In the UDLM model the numbers of atomic moments pointing in the two directions can be different (Korzhavyi *et al.*, 2002), so that there is a dominance of moments aligned in one particular direction. The UDLM state can be characterized by the fraction of spins which are pointing in the opposite direction, hence defining the order parameter r in Fig. 38(a). We note that the ground state for As antisite concentrations, $y>0.15$, is the UDLM with a reduced total magnetic moment (Korzhavyi *et al.*, 2002). This fact also coincides with the loss of ferromagnetism in this system, leading to a spin-glass-like state for even higher values of y.

One can study the magnetic stability of this system using an approach similar in spirit to the study of the phase stability of random alloys in the framework of the generalized perturbation method (GPM) (Ducastelle, 1991). One may hence consider the stability of the system with respect to periodic perturbations, i.e., magnons with a given wave vector in the present case, as com-

pared to the method of concentration waves in the GPM.

The same conclusions as obtained from the total energy study of the UDLM state above can be obtained using the lattice Fourier transformation of the exchange integrals

$$J^{\mathrm{Mn,Mn}}(\mathbf{q}) = \sum_{i \neq 0} J_{0i}^{\mathrm{Mn,Mn}} \exp(-i\mathbf{q} \cdot \mathbf{R}_i) \qquad (25)$$

from the Heisenberg model (8), where $\mathbf{R}_i$ is the distance between Mn impurities at sites 0 and i. The corresponding maximum for a given $\mathbf{q}$ vector then characterizes the ground state. In close agreement with total energy calculations we find that for a small As concentration the ground state is ferromagnetic (the maximum lies at $\mathbf{q} = \Gamma$) but for $y = 0.015$ the ferromagnetic state strongly competes with a number of other spin-wave states, which have almost the same energy.

This indicates that a realistic picture is more complex than the one following from the total energy calculations, which assume a collinear magnetic structure (UDLM). For $y > 0.015$ we thus observe a transition to a complex magnetic state whose energy is below the ferromagnetic state: the presence of many configurations with similar energies together with the disorder due to low impurity concentrations is a precursor of the spin-glass state. It should also be noted that the results above were obtained from the reference ferromagnetic state without the need to invoke calculations of a UDLM configuration. The present simple approach is thus suitable as a first rough insight into the magnetic structure of the system based on the reference ferromagnetic state, even if this state is not a ground state.

We end this section by noting that, despite the fact that periodic spin perturbations studied above bear a close similarity to magnons excited in the system, an accurate evaluation of the magnon spectra in DMS alloys represents a much more delicate task (Bouzerar, 2007).

IV. CURIE TEMPERATURE AND MAGNETIC PERCOLATION

A. Some preliminary considerations given by a toy model

In order to obtain finite-temperature properties, such as the Curie temperature T_C, we have to rely on statistical methods and solve the classical Heisenberg model that describes the magnetic ordering in the system. If for simplicity we consider only interactions between the substituted magnetic atoms on the same sublattice (extensions to this approximation are straightforward), the Heisenberg Hamiltonian takes the form of Eq. (8). The simplest solution to this Hamiltonian is to treat the spins as classical quantities, which is expected to be a reasonable approximation giving the typically large moment of the substituted magnetic atom, i.e., $S = 5/2$ for Mn in GaAs.

In order to illustrate disorder effects and magnetic percolation in disordered spin systems in the framework of the random Heisenberg model, we first study a simple
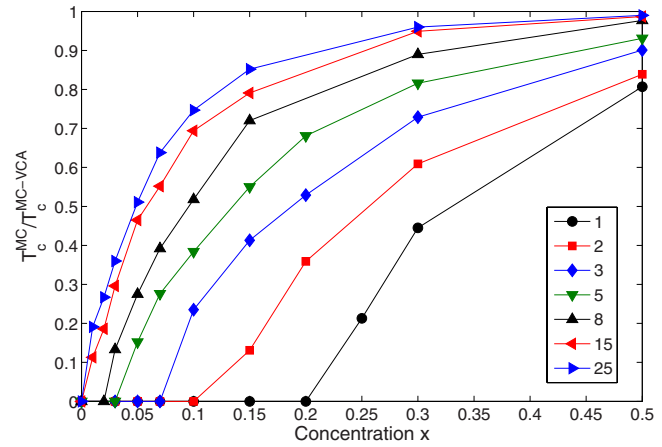

FIG. 39. (Color online) Critical temperatures for a toy model (see text) as a function of concentration and range of the exchange interactions. Results from nearest-neighbor interactions are indexed with a 1 (black dots), while results from nearest and next-nearest interactions are indexed with a 2 (squares), etc. The calculated results from Monte Carlo (MC) simulations are normalized with the corresponding values from the virtual crystal approximation (VCA).

toy model, which is an extension to a similar study by Bergqvist *et al.* (2005). For this simple model, we parametrize the exchange interactions in the Heisenberg model on the fcc lattice as

$$J_{ij}^{(n)} = \begin{cases} \dfrac{C}{\sqrt{x}} \dfrac{1}{d_{ij}^3} \exp\left(-\dfrac{d_{ij}}{\lambda}\right) & \text{if } d_{ij} \leq d_{(n)} \\ 0 & \text{otherwise,} \end{cases} \qquad (26)$$

where C is a constant, x is the concentration of magnetic atoms, $d_{ij} = |\mathbf{r}_i - \mathbf{r}_j|$, n is the shell number, and d_n is the cutoff in the interaction range. λ is a screening parameter for the exchange interactions and is chosen as $3a$ (a is the value of the lattice constant) for all concentrations. The exponential dependence on distance describes qualitatively the screening due to disorder and half metallicity, while the prefactor $1/\sqrt{x}$ is typical for double-exchange systems [see Eq. (14) and the subsequent discussion]. The parametrization is then used to calculate the critical temperatures by Monte Carlo simulations (as explained in Sec. IV.C) for several concentrations and ranges of the interactions n (up to 25 shells in the fcc lattice, which corresponds to a distance of $3.24a$). We compare results using a random distribution of the magnetic atoms (MC) with the result from the average lattice model or the virtual crystal approximation (MC-VCA). The results are shown in Fig. 39. The first fact we observe is that, with only nearest-neighbor interactions ($n = 1$), the percolation threshold for the fcc lattice is 20%, in agreement with earlier results (Kirkpatrick, 1973; Sato, Schweika, *et al.*, 2004; Bergqvist *et al.*, 2005). For smaller concentrations the magnetic atoms cannot form a percolation path throughout the system and thus there is no long-range ferromagnetic order. If the range of the interactions is increased, the percolation threshold occurs at smaller and smaller concentrations. As

an example, we note that in order to have any ferromagnetic order for a concentration of 7%, which is a typical concentration for III-V systems, the exchange interactions must extend to at least five coordination shells. If we increase the range of the exchange interactions, the MC-VCA becomes better but there is still a large modification of the exact results (MC) compared to the MC-VCA results for very dilute systems. Naturally, the MC-VCA approximation works fine for larger concentrations and systems with extended exchange interactions. However, it does not work for localized exchange interactions. One of the reasons that the MC-VCA description does not work for dilute systems is that the average separation between magnetic impurities is much larger than the range for which the exchange interaction is non-negligible. For example, on a fcc lattice with 5% magnetic atoms, the average separation is slightly larger than two lattice constants. Therefore the thermodynamic quantities (T_C) are mainly determined by the exchange interactions around the average separation and the nearest-neighbor interactions do not carry much weight. On the contrary, in the MC-VCA, all exchange interactions have the same weight, giving the first exchange interactions an unphysically large importance in the dilute limit, and therefore represent a bad approximation in this limit. Effects of disorder on the magnetic properties of DMS systems were discussed by Timm (2003). A further study of the validity of the VCA in realistic DMS systems is discussed in Sec. IV.E.3.

B. Evaluation of the Curie temperature: Self-consistent local random-phase approximation

We now describe the second step of the two-step approach, namely, the statistical treatment of the Heisenberg Hamiltonian (8), and in particular the determination of the Curie temperature (T_C). Reliable estimates of the Curie temperature in DMSs require one to go beyond the simple mean-field approximation used in the early studies. Indeed, the often used mean-field combined with virtual crystal approximation (MFA-VCA) led to overestimated Curie temperatures or overestimated stability of the ferromagnetic phase. There are several reasons for these shortcomings. The first is that it relies on the fact that the couplings are of RKKY form (the host material is weakly perturbed by the impurity and long ranged), which is inconsistent with results of *ab initio* studies. The second problem is a treatment of the thermal fluctuations within a mean-field approximation, which is particularly inappropriate in disordered materials. The third and the most drastic approximation is to neglect the dilution or disorder within the virtual crystal approximation (Bouzerar, Bouzerar, and Ziman, 2006; Bouzerar, Bouzerar, and Cepas, 2007). It is now well established that the low concentration of magnetic impurities combined with the short-range character of exchange interactions will lead to the effect of magnetic percolation (Bergqvist *et al.*, 2004, 2005; Sato, Schweika, *et al.*, 2004; Bouzerar *et al.*, 2005a). The magnetic percolation effects can be treated properly with the Monte Carlo approach (Sec. IV.C), in which both spin fluctuations and disorder are treated on the same footing (Bergqvist *et al.*, 2004; Sato, Schweika, *et al.*, 2004). Here we describe an alternative approach, in which spin fluctuations are treated in the framework of the random-phase approximation (RPA) but applied in real space (Bouzerar *et al.*, 2005a), so that effects of disorder or dilution can be treated nearly as accurately as in the Monte Carlo approach while the computational requirement are much less.

In the case of ordered materials and compounds, the RPA procedure was shown to be accurate and leads to calculated Curie temperatures in good agreement with the measured ones. We refer the interested reader to a recent review where a number of such examples can be found (Turek *et al.*, 2006). The advantage of ordered systems is that within standard RPA calculations the Curie temperature is straightforwardly obtained. It reads

$$k_B T_C = \frac{2}{3} S(S+1) \left(\frac{1}{N} \sum_{\mathbf{q}} \frac{1}{E(\mathbf{q})} \right)^{-1}, \tag{27}$$

where $E(\mathbf{q}) = J(\mathbf{0}) - J(\mathbf{q})$ and $J(\mathbf{q})$ is the Fourier transform of the magnetic couplings. Note that in the case of classical spins the couplings $J_{ij}S^2$ are replaced by J_{ij}^{cl}, which are the couplings derived using Eq. (9). The problem that appears for disordered and dilute magnetic materials is that thermal fluctuations and disorder should be treated simultaneously. Indeed, calculations that treat the disorder within the VCA and fluctuations within the RPA are known to overestimate the value of the critical temperature. The same limitation is found even if one combines a Monte Carlo treatment of spin fluctuations and the VCA treatment of alloy disorder (Bouzerar *et al.*, 2003). As can be understood intuitively, the overestimation strongly increases as we approach the percolation threshold. To be able to use a RPA-type treatment of the effective Heisenberg model, it is thus necessary to treat the effects of the disorder properly.

1. Summary of the self-consistent local RPA procedure

Consider N_{imp} interacting (classical or quantum) spins S_i of amplitude S distributed randomly on a subset of sites of a given lattice. The exchange couplings J_{ij} are assumed to be given by means of first-principles theory, and they normally depend on the impurity concentration $x = N_{\mathrm{imp}}/N$. For a given configuration of disorder, for example, as given by the coordinates of the magnetic impurities, we define the retarded spin Green's function $G_{ij}(\omega) = \int_{-\infty}^{+\infty} G_{ij}(t) e^{i\omega t} dt = \langle\langle S_i^+; S_j^- \rangle\rangle$ where $G_{ij}(t) = -i\theta(t)\langle [S_i^+(t), S_j^-(0)] \rangle$, which describes the transverse spin fluctuations.

The exact equation of motion of $G_{ij}(\omega)$ in real space is

$$\omega G_{ij} = 2\langle S_i^z \rangle \delta_{ij} + \langle\langle [S_i^+, H]; S_j^- \rangle\rangle. \tag{28}$$

The term $\langle\langle [S_i^+, H]; S_j^- \rangle\rangle$ gives rise to higher-order Green's functions such as $\langle\langle S_i^+ S_j^z; S_j^- \rangle\rangle$, which we decouple using the random-phase approximation or Tyablicov decoupling. Within this procedure the Green's

function $\langle\langle S_i^+ S_i^z ; S_j^- \rangle\rangle$ is replaced by $\langle S_i^z \rangle \langle\langle S_i^+ ; S_j^- \rangle\rangle$. The equation of motion [Eq. (28)] then becomes

$$(\omega \mathbf{I} - \mathbf{H}_{\text{eff}}) \mathbf{G} = \mathbf{D}, \tag{29}$$

where $\mathbf{H}_{\text{eff}}$, $\mathbf{G}$, and $\mathbf{D}$ are $N_{\text{imp}} \times N_{\text{imp}}$ matrices. The index i runs only over the sites occupied by a localized spin. The effective Hamiltonian matrix element is $(\mathbf{H}_{\text{eff}})_{ij} = -\langle S_i^z \rangle J_{ij} + \delta_{ij} \Sigma_l \langle S_i^z \rangle J_{lj}$ and $D_{ij} = 2\langle S_i^z \rangle \delta_{ij}$. The set of local magnetizations $\{\langle S_i^z \rangle\}_{i=1,2,\ldots,N_{\text{imp}}}$ has to be calculated *self-consistently* at each temperature. Note also that the condition $\Sigma_j (\mathbf{H}_{\text{eff}})_{ij} = 0$ is satisfied and implies that zero (the Goldstone mode) is an eigenvalue of $\mathbf{H}_{\text{eff}}$. Thus, the self-consistent local RPA (SC-LRPA) treatment is consistent with the Goldstone theorem. The reason is that both local and environmental disorder terms are treated properly and on equal footings. It is worth noting that, although the matrix is non-Hermitian (real and nonsymmetric), in the ferromagnetic phase the spectrum is real and positive at each temperature. If a negative eigenvalue appears in the excitation spectrum, this indicates an instability of the ferromagnetic phase, as, for example, in the case where frustration is included or superexchange dominates the short-range couplings (Bouzerar, Bouzerar, and Ziman, 2007). As mentioned, for a given temperature and fixed disorder configuration, the local magnetization $\langle S_i^z \rangle$ has to be determined self-consistently at each impurity site using the following expression (Callen, 1963):

$$\langle S_i^z \rangle = \frac{(S - \Phi_i)(1 + \Phi_i)^{2S+1} + (S + 1 + \Phi_i)\Phi_i^{2S+1}}{(1 + \Phi_i)^{2S+1} - \Phi_i^{2S+1}}. \tag{30}$$

The local effective magnon occupation number reads as

$$\Phi_i = \frac{-1}{2\pi \langle S_i^z \rangle} \int_{-\infty}^{+\infty} \frac{\text{Im } G_{ii}(\omega)}{\exp(\omega/kT) - 1} d\omega. \tag{31}$$

To derive the expression for the Curie temperature we expand Eq. (30) in the limit $\langle S_i^z \rangle \rightarrow 0$. We also introduce the variable $E = \omega/m$, where $m = (1/N_{\text{imp}})\Sigma_i \langle S_i^z \rangle$ is the averaged magnetization. We then obtain

$$k_B T_C = \frac{2}{3} S(S+1) \frac{1}{N_{\text{imp}}} \sum_i \frac{1}{F_i}, \tag{32}$$

where

$$F_i = \int_{-\infty}^{+\infty} \frac{A_{ii}(E)}{E} dE. \tag{33}$$

The local spectral function can be written as $A_{ii}(E) = -(1/2\pi)\text{Im}[G_{ii}(E)/\lambda_i]$. Note that the set of parameters $\lambda_i = \lim_{T \rightarrow T_C} (\langle S_i^z \rangle / m)$ are calculated self-consistently. To estimate T_C, Eq. (32) should be estimated for a large number of disorder configurations and the configuration average of these values should be evaluated.

It is interesting to reexpress the Curie temperature in terms of the eigenfunctions and eigenvalues of the effective Hamiltonian $\mathbf{H}_{\text{eff}}$ [see Eq. (29)],

$$F_i = \sum_{\alpha \neq 0} \frac{\langle i | \Psi_\alpha^R \rangle \langle \Psi_\alpha^L | i \rangle}{E_\alpha}, \tag{34}$$

where $E_\alpha = \omega_\alpha / m$ and $E_0 = 0$ for the Goldstone mode. We obtain

$$T_C^{\text{LRPA}} = \frac{2}{3N_{\text{imp}}} S(S+1) \sum_i \left(\sum_{\alpha \neq 0} \frac{\langle i | \Psi_\alpha^R \rangle \langle \Psi_\alpha^L | i \rangle}{E_\alpha} \right)^{-1}. \tag{35}$$

This expression is the extension of Eq. (27), derived for ordered systems, to systems with disorder. Equation (35) shows that the Curie temperature depends both on the excitation spectrum and on the nature of the magnetic excitations. Both localized and extended states contribute to the Curie temperature. For extended states the matrix element $\langle i | \Psi_\alpha^R \rangle \langle \Psi_\alpha^L | i \rangle$ is of the order $1/N_{\text{imp}}$ while for the localized states there is a fraction of sites for which it is of the order $1/\xi_\alpha^3$, where ξ_α is the localization length of the state. Thus it is not simple to estimate the weight of each type of excitation to the magnitude of the Curie temperature. If we neglect the real nature of the excitations and assume that all magnon states are extended, then the Curie temperature becomes

$$T_C^* = \frac{2}{3} S(S+1) \left(\sum_{\alpha \neq 0} \frac{1}{E_\alpha} \right)^{-1}. \tag{36}$$

This approximation is, however, not very accurate. In the particular case of GaMnAs, at sufficiently low impurity concentration, below 5–6 % Mn concentration this value appears to be two to three times smaller than the true LRPA Curie temperature. Therefore, a proper account of the nature of the magnon excitations is crucial to provide a quantitatively correct value of the Curie temperature.

C. Evaluation of the Curie temperature: Monte Carlo simulations

Monte Carlo (MC) simulations represent a versatile method that can be applied in many different areas. Here we discuss the use of MC simulations in statistical methods and more specifically applied to spin systems. The order parameter of such a system is the magnetization and the phase transition is of second order from a ferromagnet at low temperatures to a disordered magnet at higher temperatures. Since the total number of states of the partition function (phase space) in realistic cases is much too large to handle on any computer we need a recipe to reduce the number of states while still keeping the most important information about the system. This can be realized by employing *importance sampling* after the ideas of Metropolis *et al.* (1953). The most common algorithms for importance sampling are the single-flip Metropolis algorithm, where the transition probabilities are based on energy differences between different states, and the heat bath method. Both the heat bath method and the Metropolis algorithm are rather simple algorithms and work well on parallel computers due to local spin updates which make it straightforward to

implement domain decomposition of the lattice. The main drawback of these algorithms is the so-called *critical slowing down*, i.e., the relaxation time of the system diverges at the critical point. Therefore more advanced algorithms have been proposed which change not one spin at a time but a whole cluster of spins (Swendsen and Wang, 1987; Wolff, 1989; Wang and Landau, 2001), and as a result these algorithms are rather complicated. In order to extract any physical information from a MC simulation, one needs to perform finite-size scaling of the data. In principle it is possible to extract the information, for example, the Curie temperature T_C, from the peak of regular thermodynamic quantities like the specific heat and the susceptibility. However, this method is not always suitable for several reasons. Most importantly, the positions of the peaks change with the size of the system. The change is proportional to some critical exponents that needs to be estimated. All this together requires many additional calculations with high statistical accuracy, a time-demanding procedure. If we are interested only in the estimation of the Curie point, there is a much easier way to extract this using the cumulant crossing method, introduced by Binder (Landau and Binder, 2000). In this method, the fourth-order cumulant U_L of the order parameter

$$U_L = 1 - \langle M^4 \rangle / 3 \langle M^2 \rangle^2 \qquad (37)$$

is calculated and U_L has a size-independent universal fixed point U^* at $k_B T_C$, i.e., all $U_L(T)$ curves for different sizes L cross at the Curie temperature T_C. In this way, T_C is extracted from the unique intersection point U^* when U_L is calculated for a number of different lattice sizes (usually three) as a function of temperature.

The most appealing feature of the Monte Carlo simulation is that it provides a numerically exact solution to the classical Heisenberg model. Not only the spin fluctuation part but also the disorder is treated without approximations through configurational averaging over several disorder configurations.

D. Summary of the different methods for calculating T_C

Here we give a summary of the different computational methods used for calculating the Curie temperature in the next sections. First, it is important to realize that the different methods consider two problems, namely, the spin fluctuation problem and the treatment of the substitutional disorder. In Table IV we summarize the different methods according to their treatments of spin fluctuation and disorder. We have used three different methods for the spin fluctuation part, namely, the MFA, the RPA, and MC simulations. For the disorder treatment, two different methods have been applied, namely, the VCA (sometimes called the average lattice model or continuous media approximation) and explicit configurational averaging over different disorder configurations. The latter method does not involve any approximation and is exact, provided that a sufficiently large number of configurations is included in the averag-

TABLE IV. A summary of all the methods used in the present article for calculating Curie temperatures.

Method	Spin fluctuation	Disorder
MFA-VCA	MFA	VCA
RPA-VCA	RPA	VCA
MC-VCA	MC	VCA
AMFA	MFA	Approx.
SC-LRPA	RPA	Configuration average
MC	MC	Configuration average

ing. Note that in the average mean-field approximation (AMFA) method the disorder is treated in an approximate *ad hoc* fashion (see Sec. IV.E.2).

Since it has been proven in many DMS systems and also in model calculations that the VCA is a poor approximation for diluted systems, it is clear that the SC-LRPA (Sec. IV.B) and MC simulation (Sec. IV.C) are the two superior methods for calculating Curie temperatures in DMS systems.

E. Curie temperature in diluted magnetic materials: Case studies

In this section we illustrate the evaluation of T_C for several diluted magnetic semiconductor systems.

1. III-V-based DMS materials Mn-doped GaAs

GaMnAs is the material that has been studied in greatest detail. At low concentration, GaMnAs exhibits the highest known Curie temperature among DMS alloys. Recent nonperturbative model-based studies have demonstrated that among III-V materials GaMnAs is in fact close to optimal doping conditions (Bouzerar, Bouzerar, and Ziman, 2007).

In Fig. 40 we show the calculated Curie temperature [from Eq. (35)] in GaMnAs as a function of Mn concentration. The couplings which enter the disordered Heisenberg Hamiltonian have been calculated in the framework of the TB-LMTO-CPA methods using the LDA as described above. Note also that the calculations were done by assuming no compensating defects as As antisites and Mn interstitials [Mn(I)]. In other words, the calculation of the Curie temperature was done by assuming one hole or carrier per Mn atom, which corresponds to the optimally annealed and neutral samples. We observe good agreement between the calculated values and the Curie temperature measured in well-annealed samples. Here we show only the values calculated using the LRPA but we obtain similar results also with the MC method. The deviation observed at high concentration may indicate that the annealed sample still contains compensating defects or a secondary phase. If the same calculation is performed using exchange interactions from the LDA+U approximation, the calculated critical temperatures change by around 10%. These small changes between LDA and LDA+U results
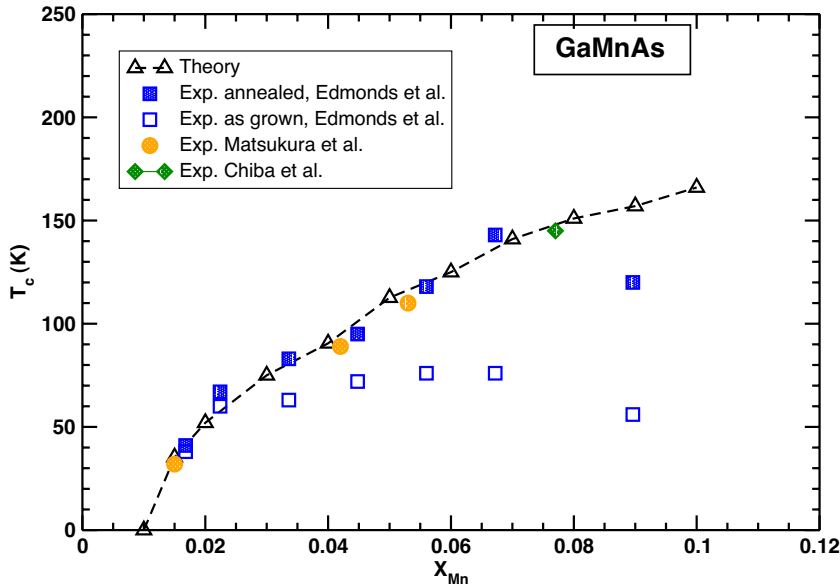
FIG. 40. (Color online) Curie temperature in $Ga_{1-x}Mn_xAs$ as a function of x. The triangles denote the calculated values within the SC-LRPA. The other symbols are the measured values for as-grown (Edmonds *et al.*, 2002a) and annealed samples (Edmonds *et al.*, 2004, 2002b). The experimental values observed by Matsukura *et al.* (1998) and by Chiba *et al.* (2003) are also indicated.

are somewhat surprising when compared with the relatively large differences between the two methods in the mean-field approximation, as shown in Fig. 21 and discussed in Sec. III.C. The reason is that there are two compensating effects shown in Fig. 37. In LDA+U the main interactions for small distances are smaller, which lowers the Curie temperature somewhat, but the interactions are more long ranged, which diminishes the effect of reduction due to percolation. In total LDA and LDA+U give similar results for small concentrations.

In a recent study (Bouzerar *et al.*, 2005b) it was shown that the present two-step approach also allows samples to be studied that contain compensating defects. Indeed, the variation of the Curie temperature in samples with a fixed nominal Mn concentration were reproduced but had different annealing treatment. It was shown that the calculated results were consistent only with the assumption that the dominant mechanism for compensation is

the presence of Mn interstitials. The assumption that As antisites dominate is inconsistent with recent experimental data (Edmonds *et al.*, 2002a; Glas *et al.*, 2004; Tuomisto *et al.*, 2004). The problem of calculating the Curie temperature of a sample that contains both Mn atoms substituting for Ga atoms, denoted here as Mn(Ga), and Mn at interstitial positions, Mn(I), is mapped onto an effective model where the substitutional Mn spins coupled to Mn(I) were removed. Microscopic calculations indicate that the Mn(I) exist preferentially on interstitial sites adjacent to occupied Mn(Ga) sites, and that the coupling between interstitials and adjacent moment is strongly antiferromagnetic (Mašek and Máca, 2004; Mikkelsen *et al.*, 2004). Thus a pair of Mn(I)-Mn(Ga) atoms is stable and magnetically inactive and can thus be removed. We denote by x_{eff} the density of remaining active Mn atoms. For each sample we have
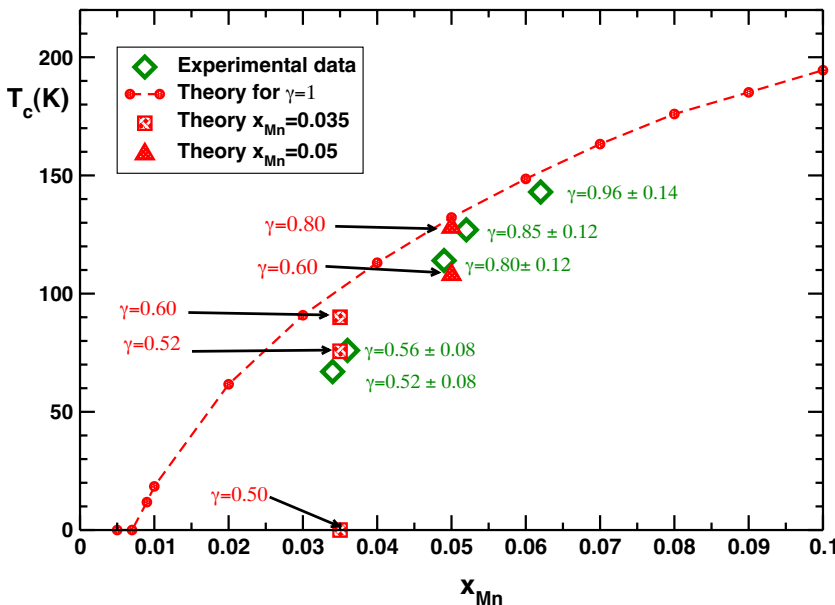

FIG. 41. (Color online) Curie temperature in GaMnAs as a function of the concentration of the magnetically active Mn. Note that the experimental data corresponding to a fixed nominal Mn concentration are plotted as a function of x_{eff}. The values of $\gamma = n_h/x_{eff}$ are also shown.

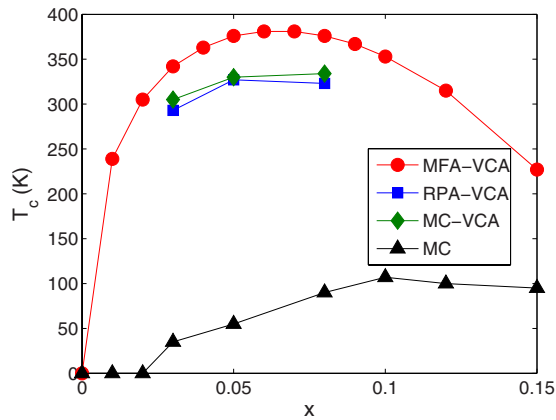FIG. 42. (Color online) Critical temperatures of Mn-doped GaN as function of Mn concentration x. See text for details.
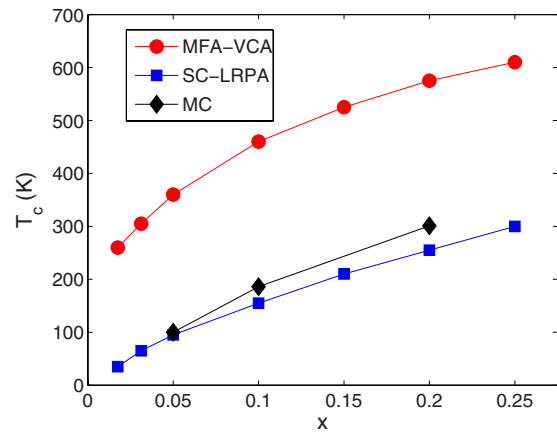

FIG. 43. (Color online) Curie temperature in ZnCrTe as a function of Cr concentration. We compare the Curie temperature calculated within MFA-VCA SC-LRPA (Bergqvist *et al.*, 2005), and MC simulations.

calculated x_{eff} and the number of holes per active Mn atom (denoted by γ). In Fig. 41 we show both the Curie temperature calculated within the SC-LRPA corresponding to different pairs of parameters (x_{eff}, γ) and the experimental values as a function of x_{eff}. Note that each measured sample has a fixed nominal concentration $x_{tot}=0.067$. We observe that the agreement between measurements and calculations corresponding to the same set (x_{eff}, γ) is good. These results demonstrate the scenario that Mn interstitials are the dominant compensating defects for Mn-doped GaAs.

Mn-doped GaN. We now discuss GaMnN. This DMS is interesting since it has been suggested as among the best candidates for room-temperature ferromagnetism (Fig. 3). This prediction triggered several experimental studies (Dietl *et al.*, 2000). However, the results for GaMnN are controversial. Some claim a very high T_C for this material (above the room temperature) while other studies reported that the material is nonmagnetic (Bonanni, 2007). We observe in Fig. 42 that all methods that employ the virtual crystal approximation (MFA-VCA, RPA-VCA, and MC-VCA) strongly overestimate T_C, while exact treatment of disorder using MC simulation (and the LRPA, not shown in figure) gives much smaller T_C. The reason for this strong suppression of the Curie temperature is the very short range of the exchange couplings (see Figs. 34 and 35). Because the Fermi level in GaMnN lies in the impurity band which is located in the middle of the gap (see Fig. 30), the couplings are of a double-exchange type and are quickly damped so that nearest-neighbor interactions are very large. However, due to the percolation effect they do not lead to high T_C values in accordance with the model calculations in Fig. 39. A recent experimental study has demonstrated that in the absence of secondary phases the Curie temperatures are indeed very low (Sarigiannidou *et al.*, 2006), which agrees with the present calculations.

T_C calculations for (Ga,Mn)N based on LDA+U coupling parameters give slightly larger T_C values for small concentrations, for example, 130 K for 10% Mn. The T_C increase becomes larger with increasing concentration,

for example, for 15% Mn a T_C value of 230 K is obtained (Sato *et al.*, 2006). This strong effect arises from the dramatic decrease in the antiferromagnetic superexchange in a LDA+U treatment, which was discussed in Sec. III.C. Since the superexchange coupling is very short ranged, the corresponding changes influence the T_C values only for larger concentrations.

2. II-VI-based DMS materials: Cr-doped ZnTe

ZnCrTe is interesting for several reasons. First, in contrast to GaAs or GaN a large amount of magnetic impurities can be introduced into ZnTe. Indeed, the solubility in II-VI materials is in general very high compared to that in III-V materials. Another reason is that the couplings in ZnCrTe are ferromagnetic, in contrast to widely studied materials such as ZnMnTe and CdMnTe for which the superexchange couplings are antiferromagnetic. The reason for the ferromagnetic Cr-Cr couplings is that the electronic configuration of Cr^{2+} is d^4 and the d bands are thus away from half filling while they are half filled (d^5) for Mn^{2+} in ZnMnTe. Thus, in contrast to ZnMnTe, which due to antiferromagnetic interactions is in a spin-glass phase (in the absence of hole doping) or a material with slow spin dynamics (Hellsvik *et al.*, 2008) at low Mn concentration, ferromagnetism is possible without hole doping in ZnCrTe. We note that even in the presence of hole doping (for example, with nitrogen) the Curie temperature in ZnMnTe and CdMnTe does not exceed a few Kelvin. In Fig. 43 we plot the Curie temperature of ZnCrTe as function of Cr concentration. We first observe that the mean-field estimate of the Curie temperature is always above room temperature (except for the lowest Cr concentrations). Within the SC-LRPA and Monte Carlo simulations the Curie temperatures are strongly reduced. As we reduce the concentration of Cr impurities the ratio $T_C^{MF}/T_C^{SC-LRPA}$ increases: for example, this ratio is close to 4 for $x=0.05$. The reason for this strong reduction compared to the mean-field value is the approach of the percolation

regime. Note that the calculated Curie temperature is also close to the measured value; for $x \approx 0.2$ it was found to be $T_C^{\text{expt}} = 300 \pm 10$ K (Saito *et al.*, 2003; Ozaki *et al.*, 2004), while we find $T_C \approx 300$ K by MC simulation and ≈ 270 K by the SC-LRPA, in good agreement with the experiment. To realize a T_C well above room temperature, the Cr concentration should be increased much more.

Mn-doped ZnO. The doping limit of transition metals into III-V semiconductors is quite low (around 10%) and there is little hope that these systems can be used for practical technological applications in the future. In II-VI semiconductors, transition metals can be doped in much higher concentrations, for example, 20% for Cr in ZnTe and 35% for Co in ZnO, and ferromagnetic order can be achieved (Coey *et al.*, 2005). This opens up the possibility of the fabrication of new materials with desired properties. But it is fair to say that until now these particular systems, especially oxide DMSs, are poorly characterized, and controversial experimental results have been published concerning the occurrence of high-temperature ferromagnetism.

In particular, several contradictory results for the magnetic properties of Mn-doped ZnO have been reported: paramagnetism, spin-glass behavior, ferromagnetism at low temperatures or even ferromagnetism at room temperature (Fukumura *et al.*, 2001; Jung *et al.*, 2002; Cheng and Chien, 2003; Sharma *et al.*, 2003; Kolesnik and Dabrowski, 2004; Kundaliya *et al.*, 2004; Kunisu *et al.*, 2005; Zhang *et al.*, 2005). Coey *et al.* (2005) suggested that high Curie temperatures can be obtained if the impurity bands hybridize with the 3*d* bands of the transition metal at the Fermi level. Electronic structure calculations based on local spin density or gradient-corrected approximations generally indicate that the dominant exchange interactions are antiferromagnetic among the Mn atoms (Janisch *et al.*, 2005; Sluiter *et al.*, 2005; Petit *et al.*, 2006; Sandratskii and Bruno, 2006).

When Mn is doped in ZnO, it replaces a Zn atom to attain a +2 charge state. This means that the electronic configuration of Mn remains almost in an atomic state, where the *d* states are half filled. The calculated nearest-neighbor magnetic interaction is strongly antiferromagnetic since the dominating exchange is superexchange resulting from the hybridization between occupied and empty states of neighboring Mn atoms (see Fig. 24). This interaction becomes stronger with increasing Mn concentration. The distant interactions are extremely weak and become exponentially damped with distance. All this is in agreement with typical superexchange properties as discussed in Sec. III.C.

Several defects or defect complexes can form during the growth of ZnO. Among these, the most common donor defects are oxygen vacancies (V_O) and zinc interstitials (Zn_I) leading to *n*-type ZnO. Other defects that can be found are zinc vacancies (V_{Zn}) and oxygen interstitials. Zinc vacancies and also oxygen substituted by nitrogen lead to a *p*-type material. Recent magnetization measurements of Mn-doped ZnO in the dilute limit

(Kittilstved *et al.*, 2005) provide a clear indication that ferromagnetism is increased by *p*-type doping, and decreased by *n*-type doping and this is one of the motivations for studying the defects theoretically. The calculated dependence of the exchange parameters between the Mn atoms on distance and concentration of Zn interstitials reveals a dominant antiferromagnetic nearest-neighbor interaction. The antiferromagnetic interactions can be very strong, on the order of 4–5 mRy (Iuşan *et al.*, 2006). Various theoretical and experimental work concluded that oxygen vacancies are the predominant native defects acting as donors in *n*-type ZnO. Calculations for the exchange parameters for different Mn-Mn separations in $Mn_{0.05}Zn_{0.95}O$ for different concentrations of oxygen vacancies (Iuşan *et al.*, 2006) indicated that the interactions among the Mn atoms are short ranged and rather small, ~ -1 mRy for the nearest-neighbor interaction, reflecting a typical situation in DMS systems, as discussed in previous sections.

Among the native defects leading to *p*-type ZnO, zinc vacancies are thought to be predominant (Janotti and Van de Walle, 2007). First-principles calculations showed that *p*-type doping due to Zn vacancies (V_{Zn}) causes the interactions to become ferromagnetic due to an increased importance of double exchange. The interaction is again heavily dominated by nearest-neighbor interactions. For some concentrations this exchange interaction becomes as high as 5.5 mRy, which must be considered as a very strong ferromagnetic interaction. For *p*-type doping by substituting some O atoms with N, it has been found (Iuşan *et al.*, 2006) that initially the nearest-neighbor interaction increases as function of N concentration, a maximum is found at $\sim 10\%$ N and then the exchange interaction decreases with increasing N concentration.

As discussed, due to the strong nearest-neighbor interaction, a mean-field estimate of the ordering temperature yields a too high value (Bergqvist *et al.*, 2004; Sato, Schweika, *et al.*, 2004) of the ordering temperature. For defects as Zn vacancies and N substituting O, which make Mn-doped ZnO ferromagnetic, simplified calculations of the ordering temperature have been performed. We note that the local RPA is probably the best alternative to Monte Carlo simulations, but an even more simple estimate yielding a rather good value of the ordering temperature is an approach called the AMFA. In this approximation, T_C is calculated by use of the value of the exchange parameter corresponding to the average distance between Mn spins in the expression for the mean-field solution of the Heisenberg model,

$$T_C^{\text{MFA}} = (2/3k_B)J_{\langle 0j \rangle}, \tag{38}$$

where $\langle 0j \rangle$ corresponds to the average distance between the Mn atoms.

The results of this calculation are compared to Monte Carlo simulations in Fig. 44. The AMFA curves are found to be qualitatively similar to those calculated by MC simulation (MCS), including peak positions and order of magnitude of the critical temperature. It should
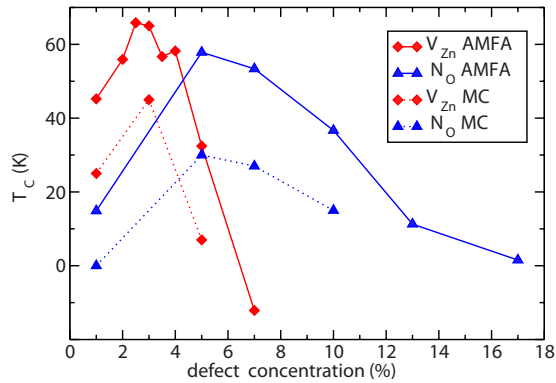
FIG. 44. (Color online) Ordering temperature calculated as a function of defect concentration by MFA and MCS for two different types of defect, zinc vacancies (V_{Zn}) and N substituting O (N_O), for $Mn_{0.05}Zn_{0.95}O$-based systems.

be noted that the conventional mean-field expression gives values of the ordering temperature that are too large by one order of magnitude. The quantitative difference is expected as MCS is a much more accurate method. It is also seen that the calculation with Zn vacancies yields a Curie temperature between 10 and 50 K, with a maximum for $\sim 3\%$ defects. For N replacing O one finds ordering temperatures reaching up to 30 K for a N concentration of 5%. Since 5% Mn is below the percolation limit for a nearest-neighbor model, it is not surprising that the calculated ordering temperatures are low. In Fig. 45 we show the calculated values of T_C from Monte Carlo simulations, for a range of Mn concentrations and for different concentrations of other defects. A nonzero T_C indicates the existence of magnetic percolation in the presence of these defects. For a delicate balance of Mn and defect concentration, it is possible to obtain a T_C as high as 135 K, for example, in the case of 15% Mn and 10% N substituting O atoms.

As mentioned, the nearest-neighbor Mn-Mn interactions become more and more antiferromagnetic as the concentration of Mn increases. However, this effect is
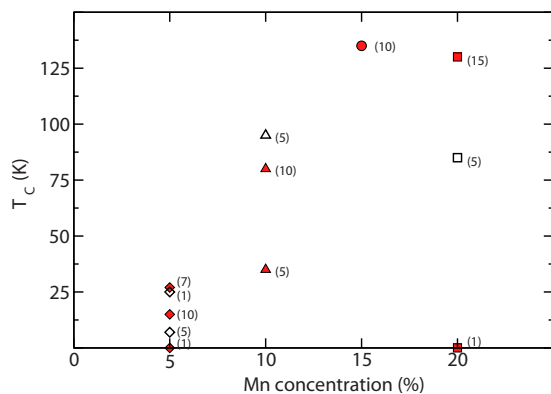

FIG. 45. (Color online) Calculated Curie temperatures with Monte Carlo simulations for $Zn_{1-x}Mn_xO$ systems. Filled symbols correspond to N substitution, while empty symbols are for V_{Zn}. In parentheses the concentration of the defect is given.
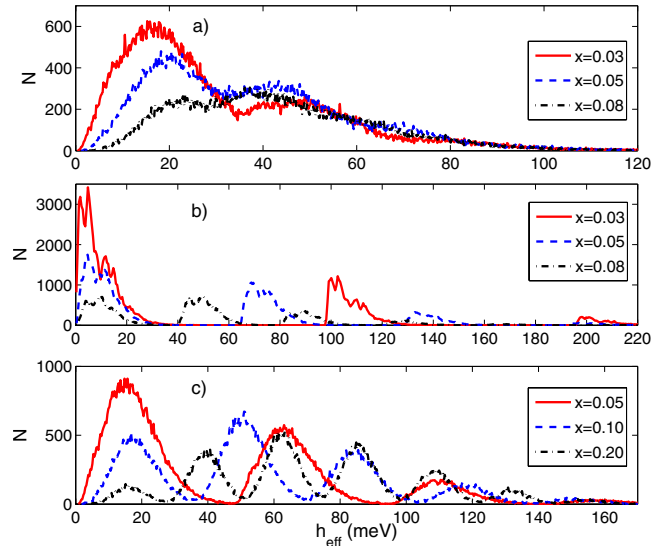
FIG. 46. (Color online) Distributions of local magnetic fields for (a) Mn-doped GaAs, (b) Mn-doped GaN, and (c) Cr-doped ZnTe for different concentrations x of the magnetic impurities.

counteracted in the presence of codoping and as a result a relatively high T_C is obtained.

3. Local effective magnetic fields

In order to get a more complete explanation of why the mean-field approximation together with the virtual crystal approximation sometimes completely fails whereas at other times it gives reasonable results, we performed an analysis of the local effective magnetic fields h^{eff} in DMS materials. To be more specific, h_i^{eff} is defined as

$$h_i^{eff} = \sum_j J_{ij} \langle S_j^z \rangle \qquad (39)$$

for each magnetic site i and at $T=0$ K, $\langle S_j^z \rangle = 1$. In a nonrandom system, each site i has the same value of h^{eff}. However, for random systems like DMS materials each site has a different local environment and one obtains a distribution of local effective magnetic fields as shown in Fig. 46 for Mn-doped GaAs, Mn-doped GaN, and Cr-doped ZnTe. These distributions were obtained for large systems with around 10^5 magnetic impurities to make sure that basically all local environments are included. The MFA-VCA estimate of T_C is directly proportional to the (arithmetic) mean average of the h_i^{eff} fields. In ordered systems the MFA typically gives quite a good estimate of T_C, around 15–20 % too large. The same can be true for nonrandom systems if the distribution of h_i^{eff} values is rather narrow, like a narrow Gaussian or a narrow potential well. The broader the distribution becomes, the more the mean-field value will overestimate the correct Curie temperature. One might guess that under these conditions a more appropriate average than the arithmetic average $\langle h_i^{eff} \rangle$ would be the harmonic mean average $\langle 1/h_i^{eff} \rangle^{-1}$. Indeed, one can also derive such an approximation from the local RPA given by

Eqs. (34)–(37). In practice, one could estimate the amount of disorder in the system by taking the ratio between the harmonic and arithmetic averages of the local magnetic fields. Figure 46 shows the distribution of the effective field h_i^{eff} for (Ga,Mn)As, (Ga,Mn)N, and (Zn,Cr)Te, each for three concentrations. First we see that for (Ga,Mn)As the distribution is relatively broad, but still reasonably compact, so that the differences between $\langle h_i^{\mathrm{eff}} \rangle$ and $\langle 1/h_i^{\mathrm{eff}} \rangle^{-1}$ are of the order of a factor of 2. However, for (Ga,Mn)N and (Zn,Cr)Te the distribution splits up into several subpeaks. For instance, for (Ga,Mn)N with 3% Mn we have one strong peak at around 0–20 meV, another weaker peak at 100 meV, and a third peak at 200 meV. The latter two correspond to the situation with one (100 meV) or two impurities (200 meV) on the neighboring sites, which increase the field strongly, but have a relatively low weight (for a concentration of 3%). Clearly the harmonic average is determined by the first peak, the width of which is completely determined by the longer-ranged interactions. The behavior for higher concentrations can be most clearly seen for (Zn,Cr)Te, where for a concentration of 20% a series of peaks become important, partly due to the larger statistical weight of dimer, trimer, and tetramer configurations.

V. OTHER DMS SYSTEMS

A. SiO$_2$-based DMSs

In this section we consider TM elements, such as V, Cr, Mn, and Co, as dopants in SiO$_2$ in α-quartz structure. SiO$_2$ has attracted much attention because of its application potential in ceramic and glass industries, in optical fibers, catalysis, and microelectronics. First-principles investigations of the electronic structure of SiO$_2$ suggest that this material might be useful for spintronic applications. Among spintronics materials based on oxides, TiO$_2$-based DMS systems have recently been studied extensively (Pearton *et al.*, 2004), and some *ab initio* studies have been reported by Sullivan and Erwin (2003) and Janisch and Spaldin (2006).

At ambient conditions the stable phase of SiO$_2$ is the α-quartz structure with space group $D_3^4(P3_121)$ and a hexagonal primitive unit cell which contains three SiO$_2$ formula units (Wyckoff, 1963). The experimental lattice constants are $a=4.916$ Å and $c=5.4054$ Å (Levien *et al.*, 1980). The atomic positions in the unit cell are determined by four internal cell parameters x, y, z, and u: O($x=0.4135$ Å), O($y=0.2669$ Å), O($z=0.1466$ Å), and Si($u=0.4697$ Å) (Levien *et al.*, 1980). The electronic structure, total energies, and magnetic moments of various SiO$_2$-based DMSs were calculated using the KKR-CPA-LDA method (Akai, 2002).

The DOS in Fig. 47 shows the half-metallic behavior for all Si$_{1-x}$TM$_x$O$_2$ systems considered (TM=V, Cr, Mn, and Co) at $x=0.05$. However, the exchange mechanism causing the ferromagnetism is different. Figure 47(a) shows the stabilization of the d^1 spin configuration of a
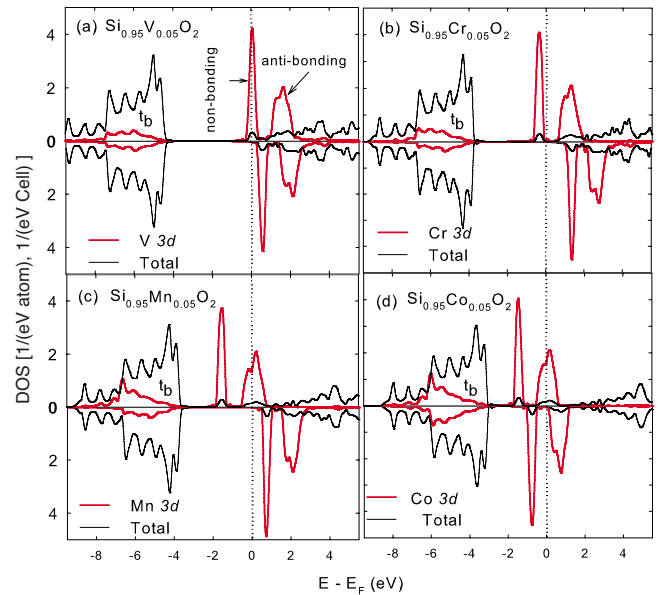

FIG. 47. (Color online) Total DOS (thin line) and PDOS of $3d$ states per impurity atom at Si sites (bold line) for four cases of a substitutional TM: (a) Si$_{1-x}$V$_x$O$_2$, (b) Si$_{1-x}$Cr$_x$O$_2$, (c) Si$_{1-x}$Mn$_x$O$_2$, and (d) Si$_{1-x}$Co$_x$O$_2$, at $x=0.05$.

V^{4+} ion. The antibonding V $3d$ states overlap in energy with the conduction band of SiO$_2$, resulting in a widening of the conduction band and a corresponding narrower band gap. The Fermi level intersects the nonbonding spin-up states which are half filled. Thus, Zener's ferromagnetic double-exchange interaction is dominant in this material. Because of the narrow band the ferromagnetism is expected to be weak. With the d^2 spin configuration of Cr^{4+}, the Fermi level lies between the nonbonding and antibonding states of the $3d$ spin-up states [Fig. 47(b)]. As in V-doped nitrides (Dinh and Katayama-Yoshida, 2005), the ferromagnetic superexchange mechanism should be dominant in this case (see Sec. III.C.5). A different behavior than for V and Cr doping is found for Si$_{1-x}$Mn$_x$O$_2$ [Fig. 47(c)] and Si$_{1-x}$Co$_x$O$_2$ [Fig. 47(d)], where the Fermi level falls into the impurity band formed by the $3d$ antibonding spin-up states. Since one-third of these states is occupied, Zener's ferromagnetic double exchange mechanism is dominant.

While the nonbonding states are localized, the $3d$ antibonding states hybridize with the $2p$ states of the O ions, resulting in a broadened impurity band in the band gap. Hence, the ferromagnetic interactions for Si$_{1-x}$Mn$_x$O$_2$ and Si$_{1-x}$Co$_x$O$_2$ are expected to be stronger than for Si$_{1-x}$V$_x$O$_2$ and Si$_{1-x}$Cr$_x$O$_2$. However, unlike Mn, Co atoms form a d^5 low-spin configuration and the exchange splitting in Si$_{1-x}$Co$_x$O$_2$ is therefore smaller than in Si$_{1-x}$Mn$_x$O$_2$. In fact, the ferromagnetism disappears due to the appearance of the antiferromagnetic superexchange mechanism when the Co concentration increases. Therefore, the ferromagnetism induced by Mn ions in SiO$_2$ is the most stable of all the dopants considered here. From simple state counting we find that the

total moments per impurity atom are $1\mu_B$ for V, $2\mu_B$ for Cr, $3\mu_B$ for Mn, and $1\mu_B$ for Co. Since interactions arising from double exchange and superexchange are short ranged, the real Curie temperatures will be strongly reduced for small concentrations. For higher concentrations of Mn quite sizable values could be obtained, provided that the solubility is sufficiently large to realize these random systems (Dinh *et al.*, 2005).

B. CuAlO$_2$-based DMSs

In this section, we review a proposal for oxide spintronics, ferromagnetic DMSs based on transparent semiconducting CuAlO$_2$ doped with TM impurities (Fukumura *et al.*, 2004). CuAlO$_2$ has a wide band gap of about 3.5 eV (direct) and 1.8 eV (indirect) (Kawazoe *et al.*, 1997) and the hexagonal delafossite structure with $a = 2.86$ Å and $c = 16.96$ Å (Kawazoe *et al.*, 1997). The material is in space group $R\bar{3}m$ (Wyckoff, 1963). The characteristic physical property of CuAlO$_2$ is its *p*-type conductivity in as-grown samples (Epicier and Esnouf, 1990). This feature distinguishes CuAlO$_2$ from the other oxides, which normally show *n*-type conductivity. This makes CuAlO$_2$ an interesting host material for oxide spintronics.

The delafossite CuAlO$_2$ has two cation sites, Cu^{1+} and Al^{3+}, and both of them can be substituted by magnetic TM impurities. The Cu site is coordinated by two O atoms and makes a O-Cu-O dumbbell structure, on the other hand, the Al site is coordinated nearly octahedrally by six O atoms. Both atoms make layer structures perpendicular to the *c* axis in CuAlO$_2$. Because of the differences in coordination number, local symmetry, and charge state between the two sites, we have much freedom in doping treatment. For example, we can introduce magnetic impurities in the Cu layer and control the carrier density by dopants in the Al layer. Here we discuss only the chemical trend of ferromagnetism in (Cu,TM)AlO$_2$ and calculate the T_C values using the mean-field approximation and Monte Carlo simulation to investigate these new DMS systems based on oxide materials (Kizaki *et al.*, 2005).

The calculated energy difference between ferromagnetic and paramagnetic states obtained by the KKR-CPA-LDA method (Akai, 1989, 2002; Akai and Dederichs, 1993) is shown for (Cu,TM)AlO$_2$ in Fig. 48 (Kizaki *et al.*, 2005). As shown in the figure, the ferromagnetic state is more stable than the paramagnetic state for the last half of the 3*d* TM series (i.e., for Mn, Fe, Co, and Ni dopings); on the other hand, the paramagnetic state is more stable for the first part of the series (i.e., for V and Cr dopings). The energy difference shows its maximum around (Cu,Fe)AlO$_2$ and (Cu,Co)AlO$_2$. This chemical trend is opposite of that in II-VI and III-V DMSs, where elements of the first half of the 3*d* TM series exhibit ferromagnetism (see Sec. II.D). The trend in Fig. 48 can be understood by consideration of the O-Cu-O dumbbell-like configuration and the +1 charge state of TM impurities at the Cu site in CuAlO$_2$. In order to
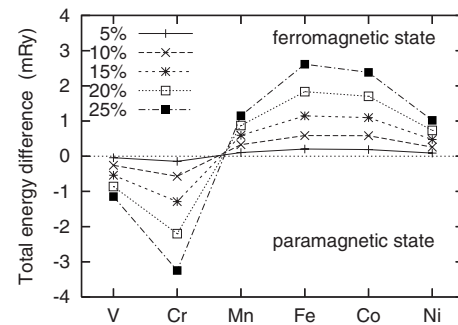

FIG. 48. Stability of the ferromagnetic states in (Cu,TM)AlO$_2$. The total energy difference per unit cell between ferromagnetic and paramagnetic states in V-, Cr-, Mn-, Fe-, Co-, and Ni-doped CuAlO$_2$ is plotted for 5%, 10%, 15%, 20%, and 25% concentration of TM atoms. A positive difference indicates that the ferromagnetic state is more stable than the paramagnetic state. From Kizaki *et al.*, 2005.

discuss the chemical trend, we analyze the calculated DOSs of the (Cu,TM)AlO$_2$ systems.

Figure 49 shows the DOS in a 5% TM-doped CuAlO$_2$-based DMS in the ferromagnetic state (Kizaki *et al.*, 2005). One sees that the impurity bands appear in the band gap and in this DMS the double-exchange mechanism stabilizes the ferromagnetism. Because of the low coordination number, the hybridization between *d* states and host valence bands is weak, leading to a small crystal field splitting. Consequently, all DMS systems shown in Fig. 49 have a high-spin state leading to a half-metallic electronic structure. Moreover, the band broadening caused by disorder is always larger than the crystal field splitting; therefore the impurity bands are merged into one peak which accommodates five *d* electrons.
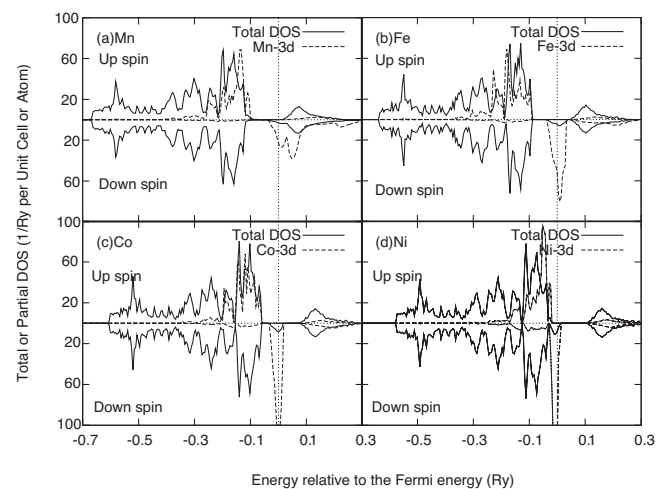

FIG. 49. Total density of states per unit cell (solid line) and local density of *d* states at TM site per atom (dashed line) in (a) Mn-, (b) Fe-, (c) Co-, and (d) Ni-doped CuAlO$_2$ in a ferromagnetic state. The TM atoms occupy Cu substitutional sites. The TM concentration is 5% for each case. The horizontal axis is the energy relative to the Fermi energy.
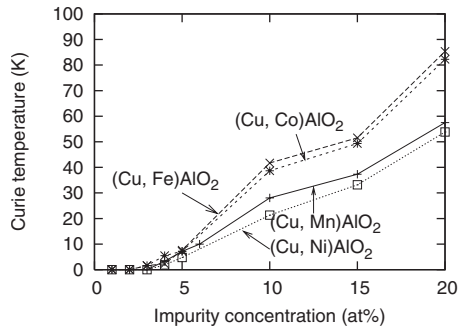
FIG. 50. Calculated T_C of $(Cu,Mn)AlO_2$, $(Cu,Fe)AlO_2$, $(Cu,Co)AlO_2$, and $(Cu,Ni)AlO_2$ using the MCS as a function of concentration.

Taking the +1 charge state of the TM impurities into account, Mn, Fe, Co, and Ni should have d^6, d^7, d^8, and d^9 electron configurations, respectively. This is confirmed in the calculated DOSs (Fig. 49). As shown in the figure, the impurity bands are partially occupied and double-exchange stabilizes ferromagnetism. The double-exchange interaction is particularly efficient when the Fermi level is located at the center of the impurity band, and this is why the energy difference has a maximum for Fe and Co doping.

For accurate T_C calculations the effective exchange interactions between TM ions in the $(Cu,TM)AlO_2$ host have been determined (Kizaki *et al.*, 2005). As expected for double exchange and superexchange, the J_{ij} values are very large for nearest neighbors, but decay strongly for more distant neighbors. Due to this short-ranged nature, the exchange interactions between magnetic impurities on different Cu layers are very weak. Because of the percolation effect, ferromagnetism is weak and the T_C values calculated by MC simulation are very low in these DMS systems as shown in Fig. 50 (Kizaki *et al.*, 2006). The highest value in Fig. 50 is below 100 K, which obviously is far from room temperature.

An alternative doping, namely, TM doping at the Al site, can be considered. However, the exchange coupling constants between TM impurities in $Cu(Al,TM)O_2$ are short ranged. Therefore, the magnetic percolation results in low T_C values. For $Cu(Al,Mn)O_2$, T_C exceeds 100 K when Mn is doped up to 20% (Kizaki *et al.*, 2006). This is the material with the largest T_C among the $CuAlO_2$-based DMS systems for the concentration range considered.

C. DMSs based on half-Heusler alloys

The crystal structure of half-Heusler alloys ($C1_b$ structure), which we describe with the chemical formula XYZ, consists of three fcc sublattices with basis atoms X at the origin, Y at $(\frac{1}{4}\frac{1}{4}\frac{1}{4})$, and Z at $(\frac{3}{4}\frac{3}{4}\frac{3}{4})$. In the half-Heusler-based DMSs, Y sites are randomly substituted with Mn atoms. If the Z atomic positions are empty, the crystal structure is equivalent to the zinc-blende structure. Because the crystal structure and lattice constants
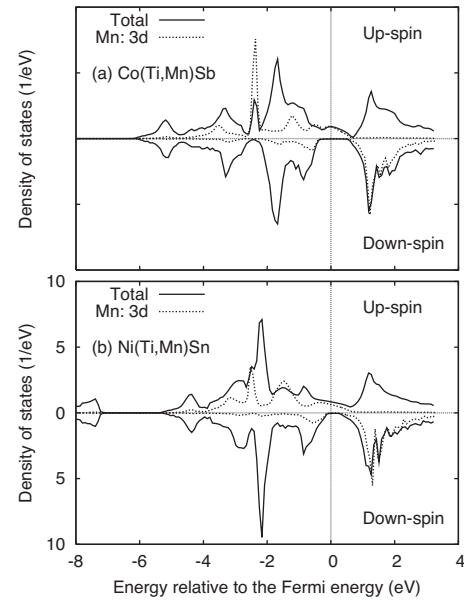

FIG. 51. Density of states as a function of energy relative to the Fermi energy for 20% Mn doped in (a) CoTiSb and (b) NiTiSn calculated by use of the KKR-CPA method. The solid and dotted lines indicate total and partial Mn d densities of states.

of half-Heusler compounds are similar to those of III-V and II-VI compounds, which are often used in present semiconductor technology, half-Heusler compounds are attractive candidates for spintronic applications. If high-T_C DMSs are to be created, heavy magnetic impurity doping above the percolation threshold is needed. In half-Heusler compounds, the solubility of magnetic impurities should be much higher than in the III-V semiconductors, since many ordered compounds exist and no major problems with compensation defects are expected for these metallic systems. Additionally, we can expect strong magnetic interactions between the doped Mn atoms in the half-Heusler systems, because the valence and conduction bands consist of the d states of X and Y atoms, respectively, so that there is strong d_{Mn}-d_X hybridization. In the following, based upon *ab initio* results, we analyze the electronic structure, exchange coupling constants, and ordering temperatures of Mn-doped Co(Ti,Mn)Sb and Ni(Ti,Mn)Sn (Fukushima *et al.*, 2007).

The first point discussed is the electronic structure of Mn-doped half-Heusler compounds, which is fundamental for the understanding of their magnetic properties. Galanakis and Dederichs (2005) and Galanakis *et al.* (2006) showed that the total spin magnetic moment per unit cell M_t scales linearly as $M_t = Z_t - 18$ with Z_t the number of valence electrons. According to the sum rule for the total magnetic moment per unit cell, proposed by Galanakis and Dederichs (2005) and Galanakis *et al.* (2006), we can use half-Heusler compounds with 18 valence electrons as host materials; they exhibit semiconducting behavior with a band gap arising from strong hybridization between the d states of the higher- and lower-valent transition-metal atoms. In Fig. 51, the den-

sity of states of 20% Mn doped in (a) CoTiSb and (b) NiTiSn, calculated by the KKR-CPA method (Akai and Dederichs, 1993; Akai, 2002), is plotted as a function of energy relative to the Fermi level (E_F). In our calculations, lattice distortions due to impurity doping are neglected and experimental lattice constants of host half-Heusler compounds are used (Webster and Ziebeck, 1988).

The Mn-doped half-Heusler systems, as shown in Fig. 51, have half-metallicity with a band gap at E_F in the spin-down state and a metallic DOS at E_F in the spin-up state. As in transition-metal-doped II-VI or III-V semiconductors, the Mn atoms in half-Heusler systems are tetrahedrally coordinated, so that the fivefold-degenerate Mn d states are divided into t_{2g} states, which strongly hybridize with the valence d states of Fe, Co, or Ni, and e_g states, which lie energetically below the t_{2g} states. As shown in Fig. 51, in Co(Ti,Mn)Sb and Ni(Ti,Mn)Sn, due to Mn doping at Ti sites, the extra three electrons occupy not only the Mn e_g states completely, but also one of the three Mn t_{2g} states, and the total magnetic moment per unit cell can be estimated to be $3\mu_B$. The Fermi energy is located in the t_{2g} states in Co(Ti,Mn)Sb and Ni(Ti,Mn)Sn. In this situation, the energy gain is caused by broadening of the Mn t_{2g} band with increasing Mn concentration, i.e., it is due to double exchange (Akai, 1998; Sato and Katayama-Yoshida, 2002).

The next point of analysis is the dependence of the magnetic interaction on the distance between Mn atoms. Figure 52(a) shows the exchange coupling constant of Ni(Ti, Mn)Sn calculated with Eq. (9). The horizontal axis indicates the distance between two Mn atoms normalized by the lattice constant. Mn 10%, 20%, and 30% cases are shown in Fig. 52(a). The distance dependence of the exchange coupling constant is strongly affected by the electronic structure; an observation that is important since the mechanism stabilizing the ferromagnetic state in DMS systems relies heavily on the distance dependence. The exchange coupling constants of Ni(Ti,Mn)Sn are strong only for the nearest neighbors and decay exponentially with the distance between two Mn atoms. This short range of the exchange interaction is affected by the electronic structure of Ni(Ti,Mn)Sn which has deep impurity bands in the band gap, because the wave functions for deep impurity states in the band gap decay exponentially.

It is worthwhile to compared the exchange coupling constants of Mn-doped half-Heusler compound and those of transition-metal-doped III-V and II-VI semiconductors. The interaction range in Ni(Ti,Mn)Sn is much smaller than in (In,Mn)As and (Ga,Mn)As, where the ferromagnetic state is stabilized by the double- or p-d exchange interaction (Bergqvist *et al.*, 2004; Sato, Schweika, *et al.*, 2004; Sato *et al.*, 2007a). However, since the nearest-neighbor interactions of Ni(Ti,Mn)Sn are larger than those of (Zn,Cr)Te, in which room-temperature ferromagnetism was observed (Saito *et al.*, 2003; Fukushima *et al.*, 2004; Ozaki *et al.*, 2004), we may
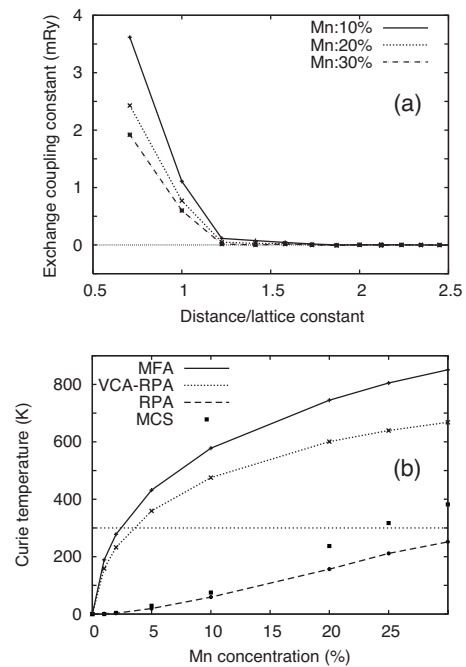

FIG. 52. Magnetic properties of Ni(Ti,Mn)Sn. (a) Calculated exchange coupling constants between Mn atoms in Ni(Ti, Mn)Sn as a function of distance between two Mn atoms. Mn 10%, 20%, and 30% cases are indicated by solid, dotted, and dashed lines. (b) Calculated Curie temperature of Mn-doped NiTiSn as a function of Mn concentration. The Curie temperature is calculated with the mean-field approximation (MFA, solid lines), random-phase approximation in the virtual crystal approximation (RPA-VCA, dotted lines), random-phase approximation (RPA, dashed lines), and Monte Carlo simulation (MCS, filled squares).

expect Ni(Ti,Mn)Sn to have high T_C values when the Mn concentration is high.

Figure 52(b) shows calculated values of T_C for Ni(Ti,Mn)Sn obtained with the mean-field approximation (Sato *et al.*, 2003), the random-phase approximation with the virtual crystal approximation (Pajda *et al.*, 2001; Bouzerar *et al.*, 2003), the random-phase approximation (Bouzerar *et al.*, 2002, 2004, 2005a; Hilbert and Nolting, 2004, 2005), and Monte Carlo simulations (Binder and Heermann, 2002). As pointed out previously, we need to take into account the magnetic percolation effect for accurate estimation of T_C for DMSs. As shown in Fig 52(b) the RPA and MC simulations predict that all systems become paramagnetic below the percolation threshold. In the high-concentration region (25–30 %) for Ni(Ti,Mn)Sn it is possible to reach ordering temperatures above room temperature. Therefore, if high-concentration doping is possible, DMS materials based on Ni(Ti,Mn)Sn may be suitable for semiconductor spintronics applications. Similar results were obtained in Co(Ti,Mn)Sb systems (Fukushima *et al.*, 2007).

VI. INHOMOGENEITY IN DMSs

In the preceding sections, we discussed magnetic properties of homogeneous DMS systems with TM im-
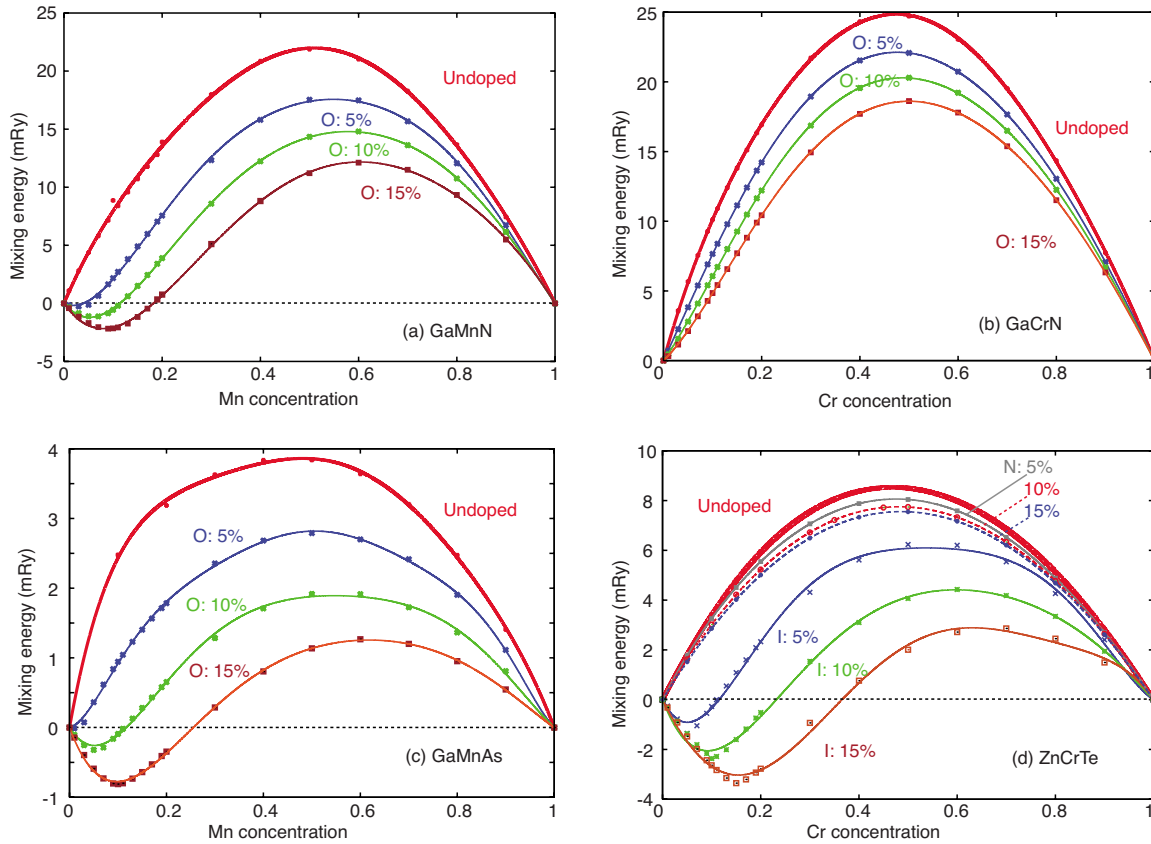
FIG. 53. (Color online) Calculated mixing energy of (a) Mn in GaN, (b) Cr in GaN, (c) Mn in GaAs, and (d) Cr in ZnTe. From Sato *et al.*, 2007.

purities distributed randomly at cation sites. However, the assumption of homogeneity can be unrealistic in many cases. For example, rather inhomogeneous TM distributions have been observed in several DMS systems such as (Ga,Mn)N (Ploog *et al.*, 2003; Bonanni, 2007), (Al,Cr)N (Gu *et al.*, 2005), and (Zn,Cr)Te (Kuroda *et al.*, 2007), and the relationship between inhomogeneity and the ferromagnetic behavior of DMSs was pointed out. By careful tuning of crystal growth conditions, inhomogeneity can be suppressed more or less, but because of the strong attractive chemical interactions between TM impurities it is difficult to realize a completely random distribution. Thus, for realistic materials design, the inhomogeneity effects should be considered. In this section, we first discuss the calculated mixing energies of TM impurities in compound semiconductors and show that in general DMSs have a strong tendency toward spinodal decomposition, resulting in an inhomogeneous distribution of TM impurities. Next, calculated effective pair interactions between TM impurities in DMSs are analyzed and an inhomogeneous distribution in DMS materials is simulated within the Monte Carlo method to assess how the magnetic properties of DMSs are changed by the inhomogeneity (Sato *et al.*, 2005; Fukushima *et al.*, 2006a; Sato, Fukushima, and Katayama-Yoshida, 2007a). The effects of clustering are also studied for a model Hamiltonian based on classical Heisenberg spins with RKKY-type interactions (Priour and Sarma, 2006).

A. Mixing energy of 3*d*-TM impurities in semiconductors

The mixing energy of a two-component alloy $A_{1-x}B_x$, where x is the concentration of the component B, is defined as $\Delta E = E_{tot}(A_{1-x}B_x) - (1-x)E_{tot}(A) - xE_{tot}(B)$, where E_{tot} denotes the total energy. Thus, ΔE compares the total energy of a homogeneous alloy and the averaged total energy of the components. For (Ga, Mn)As, ΔE is calculated as $E_{tot}(Ga_{1-x}Mn_xAs) - (1-x)E_{tot}(GaAs) - xE_{tot}(MnAs)$. Note that we consider the zinc-blende structure for all compounds in the equation, i.e., we suppose that the crystal structure is always coherent. This structural coherence is actually observed in experiments (Gu *et al.*, 2005; Jamet *et al.*, 2006; Kuroda *et al.*, 2007). Moreover, DMS systems can be grown only on substrates of the host semiconductor and the lattice parameter is more or less fixed by the substrate. By definition, a positive ΔE indicates that the system has a tendency toward phase separation into GaAs and MnAs (Sato *et al.*, 2005). In the present calculations, we deal with the mixing energy only to describe the general chemical trend of DMS systems. The second derivative of the free energy indicates if the phase separation occurs via spinodal decomposition or nucleation.

In Fig. 53, the calculated mixing energies of (Ga,Mn)N, (Ga,Cr)N, (Ga,Mn)As, and (Zn,Cr)Te are shown. We also show the effects of additional *n*- and *p*-type carrier doping on the mixing energy (Bergqvist *et*

al., 2003; Sato, Fukushima, and Katayama-Yoshida, 2007b). As donor impurity, we consider O at N and As sites in GaN and GaAs, respectively. In the case of ZnTe, we substitute Te by I for *n*-type doping and by N for *p*-type doping. As shown in Fig. 53, the investigated DMS materials have a convex concentration dependence of the mixing energy, and ΔE is always positive for the whole range of concentration when only TM impurities are doped into the host materials. This means that these DMS systems favor phase separation. For wide-band-gap semiconductors, such as GaN-based DMSs, the mixing energy is particularly large, as shown in Fig. 53, and it is prohibitively difficult to fabricate homogeneous (Ga,Mn)N and (Ga,Cr)N. For (Ga,Mn)As the mixing energy is about a factor of 6 smaller and homogeneous doping might be possible using nonequilibrium crystal growth techniques. This observation corresponds well to the experimental findings (Matsukura *et al.*, 2002; Bonanni, 2007).

When donor impurities and compensating hole carriers are introduced, the mixing energy is considerably lowered as shown in Fig. 53. This arises from the energy gained by electron transfer from the higher-lying donor level to the lower level of the Mn hole. Because of this effect, in (Ga,Mn)N, (Ga,Mn)As, and (Zn,Cr)Te, ΔE becomes negative for low concentrations. This means that the solubility of TM impurities is enhanced by the introduction of donors. This technique to enhance the solubility is called co-doping and is used to overcome unipolarity of carrier doping in wide-gap semiconductors (Yamamoto and Katayama-Yoshida, 1997). As discussed, in order to synthesize DMS materials with a high Curie temperature it is necessary to dope TM impurities to a high concentration above the percolation threshold. The codoping method is a promising way to overcome the low solubility limit in order to realize high-T_C DMSs. Of course, the compensation of holes suppresses ferromagnetism, so after the crystal growth one has to remove the codopant impurities by some means. Mobile donor impurities such as Mn or H interstitials might be ideal in this respect and have been discussed by Sato, Fukushima, and Katayama-Yoshida (2007b). In general, during crystal growth the mixing energy is more or less regulated unintentionally by introduction of native donors such as vacancies or interstitials. This is called self-compensation and was studied for (Ga,Mn)As systems by Erwin and Petukhov (2002).

B. Chemical pair interactions

In the previous section, it was shown that DMS systems have a general tendency toward spinodal decomposition. In order to see how the decomposition affects the magnetic properties, we simulate the inhomogeneous distribution of TM impurities using the Monte Carlo method. For this purpose, we use the alloy Ising model to describe the energetics of the system, i.e.,
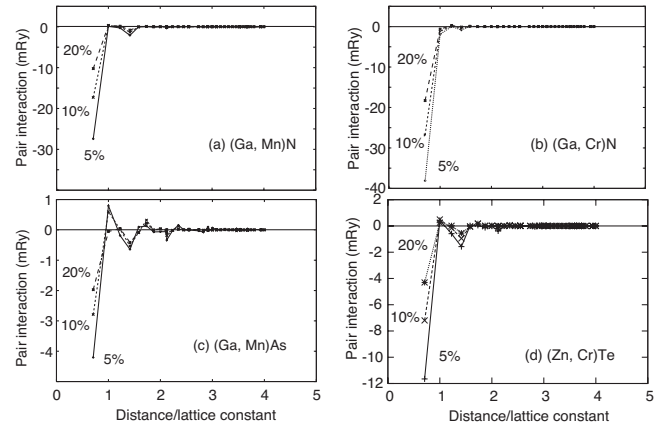

FIG. 54. Effective pair interactions between (a) Mn in GaN, (b) Cr in GaN, (c) Mn in GaAs, and (d) Cr in ZnTe as function of distance normalized to the lattice constant. Negative interactions indicate that the pair interactions are attractive.

$$H = -\frac{1}{2}\sum_{i\neq j} V_{ij}\sigma_i\sigma_j, \tag{40}$$

where V_{ij} is the effective pair interaction between sites i and j. σ_i is the occupation of an impurity atom at site i, i.e., $\sigma_i=1$ if site i is occupied by an impurity atom while $\sigma_i=0$ if site i is occupied by a host atom. For a two-component alloy $A_{1-x}B_x$ the effective pair interaction is calculated as $V_{ij}=V_{AA}+V_{BB}-2V_{AB}$, where V_{AB} is the potential energy when A and B atoms occupy i and j sites, respectively. By definition, a negative V_{ij} means an attractive interaction. The effective pair interactions V_{ij} are calculated from first principles. The prescription to calculate V_{ij} was proposed by Ducastelle and Gautier and is called the generalized perturbation method (GPM) (Ducastelle and Gautier, 1976; Gonis, 2000). We use here the formulation given by Turchi *et al.* (1988).

In Fig. 54 the calculated V_{ij} for (Ga,Mn)N, (Ga,Cr)N, (Ga,Mn)As, and (Zn,Cr)Te are shown. Most of the calculated pair interactions are negative which means that magnetic impurities attract each other in these DMSs. These DMS materials favor phase separation because of the attractive pair interactions, and during crystal growth spinodal decomposition can occur, if the related temperatures are high enough for a sufficiently long time. As a whole, the interactions are strongest in GaN-based DMSs as shown in Fig. 54 and smallest in GaAs-based DMSs. This result corresponds well to the calculations of the mixing energy and suggests that in GaN-based DMSs it is difficult to avoid clustering of the TM impurities. Once the interactions are given, we can simulate by the standard Monte Carlo algorithm the TM impurity distributions in DMS materials under spinodal decomposition (Sato *et al.*, 2005). In the next section we present simulation results of spinodal decomposition for some selected materials.

C. Self-organized nanostructures in DMS

In this section, we show results of simulations of spinodal decomposition and clustering in DMS materials for

Cr-doped ZnTe as a typical example. We also discuss the possibility of fabricating magnetic nanostructures in DMSs using the self-organization resulting from spinodal decomposition. The simulation method is easily generalized to other DMS systems (Sato *et al.*, 2005; Fukushima *et al.*, 2006a; Eriksson *et al.*, 2007). In the present simulations we take into account only the chemical pair interactions calculated using the GPM. In reality, the Hamiltonian should contain more terms, such as elastic energy, interface energy, and many-particle interactions (Vaithyanathan *et al.*, 2002). Moreover, it is known that the GPM pair interactions might be modified due to electrostatic corrections, magnetic effects, and higher local concentrations within the clusters (Ruban and Skriver, 2002; Ruban and Abrikosov, 2008). These corrections might change the details of the simulation results. However, we believe that the present simple simulations describe the basic physics underlying the clustering phenomenon in DMSs and are useful for an intuitive understanding of the possible clustering processes occurring during crystal growth.

1. Dairiseki phase

The approach used to simulate the spinodal decomposition in DMSs is very simple. We describe DMSs using the alloy Ising Hamiltonian [Eq. (40)]. The effective pair interactions V_{ij} are already calculated using the generalized perturbation method (Fukushima *et al.*, 2006b) as explained previously (Fig. 54). In the simulations, one first prepares a large supercell of the fcc structure (since the magnetic impurities in the zinc-blende structure are positioned on fcc sublattice) and distributes impurity sites randomly as an initial atomic configuration. Then the atomic configurations are updated using the Monte Carlo method, i.e., one chooses one magnetic impurity atom and tries to move it to one of the nearest-neighbor sites. The energy difference between initial and trial configurations is calculated, and we decide to accept the trial configuration or not using the Metropolis algorithm. This Monte Carlo step is repeated many times and the system is moved toward thermal equilibrium. However, one should bear in mind that the nonequilibrium crystal growth technique used in the experiments prevents the system from reaching thermal equilibrium. To simulate this situation, we interrupt the Monte Carlo loop after a certain number of steps (typically 100 MC steps per impurity atom).

Figure 55(a) shows simulation results for the spinodal decomposition in (Zn,Cr)Te. In the figure, snapshots of Cr configurations in the supercell ($14 \times 14 \times 14$ conventional fcc unit cells) after 100 Monte Carlo steps per impurity are shown for 5% of Cr (Fukushima *et al.*, 2006b). The simulations are performed at a scaled parameter $k_B T / V_{01} = 0.5$, where k_B is the Boltzmann constant and V_{01} is the chemical pair interaction between nearest-neighbor Cr atoms in (Zn,Cr)Te. In the simulation, Cr atoms are allowed to diffuse three dimensionally in the supercell (3D spinodal decomposition), i.e.,
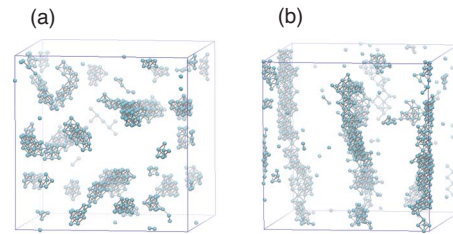

FIG. 55. (Color online) Cr configuration in (Zn,Cr)Te (a) under 3D spinodal decomposition (dairiseki phase) after 100 Monte Carlo steps. (b) The 1D konbu phase obtained by layer-by-layer crystal growth based on 2D spinodal decomposition. Cr concentration is 5% for both phases. Cr sites are indicated by spheres and nearest Cr-Cr pairs are combined by bars. By controlling the dimensionality of the phase separation, we can fabricate either the dairiseki phase or the konbu phase.

the trial site is chosen from the 12 nearest-neighbor sites of the fcc structure.

For 5% Cr [Fig. 55(a)] the magnetic impurities form only isolated clusters and the system becomes superparamagnetic. When the clusters begin to connect with each other for higher concentrations and percolate through the whole crystal, the system becomes ferromagnetic with a high T_C. We call this spinodal phase a "3D dairiseki phase" ("dairiseki" means marble in Japanese). It is shown that the magnetic impurities also form a dairiseki phase in other DMS systems such as (Ga,Mn)N, (Ga,Mn)As, and (Ga,Cr)N (Sato *et al.*, 2005; Katayama-Yoshida *et al.*, 2007b). The 3D dairiseki phase was experimentally observed in (Ga,Mn)N, (Ga,Cr)N, and (Al,Cr)N by use of transmission electron microscopy (TEM) and energy-dispersive x-ray spectroscopy (EDS) (Gu *et al.*, 2005; Tay *et al.*, 2006; Bonanni *et al.*, 2007). Kuroda *et al.* (2007) proposed that the spinodal decomposition can be controlled by *n*- or *p*-type carrier doping.

2. Konbu phase

In layer-by-layer crystal growth as is realized in molecular-beam epitaxy (MBE), metal-organic vapor-phase epitaxy (MOVPE), and metal-organic chemical-vapor deposition (MOCVD), atomic diffusion is restricted to the surface layer. This condition can also be included into our simulations of spinodal decomposition [two-dimensional (2D) spinodal decomposition]. The simulation procedure is as follows. First, the first layer is annealed by use of the Metropolis algorithm. Next, we deposit the second layer and perform simulated annealing only for the second layer in the annealed environment of the frozen first layer. The configuration of the second layer is fixed when the third layer is deposited. By repeating the above process up to the required number of layers, we can obtain the spinodal decomposition phase under layer-by-layer growth conditions.

Figure 55(b) shows simulation results of layer-by-layer crystal growth for 5% Cr-doped ZnTe (Fukushima *et al.*, 2006a). As shown in Fig. 55(b), in contrast to the case of 3D spinodal decomposition, here the Cr atoms

form characteristic quasi-one-dimensional structures along the crystal growth direction. This is due to the attractive interaction of the newly deposited Cr atoms with the Cr clusters formed in the layer beneath. The Cr clusters in the lower layers are fixed and cannot move out. As a result, the Cr clusters formed have a characteristic columnar shape as shown in Fig. 55(b). We call this quasi-1D phase the "1D konbu phase" ("konbu" means seaweed in Japanese). Even if the concentration of magnetic impurities is low it is possible to generate a 1D konbu phase with columns perpendicular to the surface by tuning of the annealing temperature and growth rate. In fact, Gu *et al.* (2005) and Jamet *et al.* (2006) observed the quasi-1D konbu phase experimentally in the (Al,Cr)N and Mn-doped Ge systems. It should be noted that the T_C of the quasi-1D konbu phase is very low, predicted to be about 15 K with the random-phase approximation (Bouzerar *et al.*, 2004, 2005a; Hilbert and Nolting, 2004). Such low-T_C ferromagnetism is due to the weak magnetic interactions between the quasi-1D structures. However, if the clusters are large enough, the system shows hysteretic behavior even at high temperature because of the superparamagnetic blocking phenomenon. This point will be discussed in the next section.

D. Superparamagnetism in DMSs

In this section, we discuss how the spinodal decomposition affects the magnetic properties of DMS systems, in particular the Curie temperature. As shown in the previous section, small clusters are formed in DMS because of spinodal decomposition. In this case, the system is considered to be superparamagnetic. In this section, we also discuss the blocking phenomenon in superparamagnetic DMS.

1. Curie temperature of spinodal decomposition phases in DMSs

In order to calculate the Curie temperature for inhomogeneous DMS materials, the random-phase approximation (see Sec. IV.B) proposed by Bouzerar *et al.* (2002, 2004, 2005a) and Hilbert and Nolting (2004, 2005) has been used. In this method, the distribution of TM impurities in a supercell is explicitly treated to calculate magnetic excitations, and from the excitation spectra T_C is estimated within the RPA. This method gives somewhat lower T_C values than the MC simulations; however, the percolation effects are correctly taken into account and T_C predictions by this method are found to be reasonable (see Sec. IV).

In Fig. 56 the T_C values of (Ga,Mn)N, (Ga,Cr)N, and (Ga,Mn)As calculated by the RPA method are shown as functions of the number of Monte Carlo steps. As explained in Sec. III.C.4, the LDA overestimates the antiferromagnetic superexchange interaction; therefore for higher concentration the LDA predicts unrealistically low values of T_C. In Fig. 56 this deficiency is corrected using the LDA+U method. As shown in Fig. 56, with
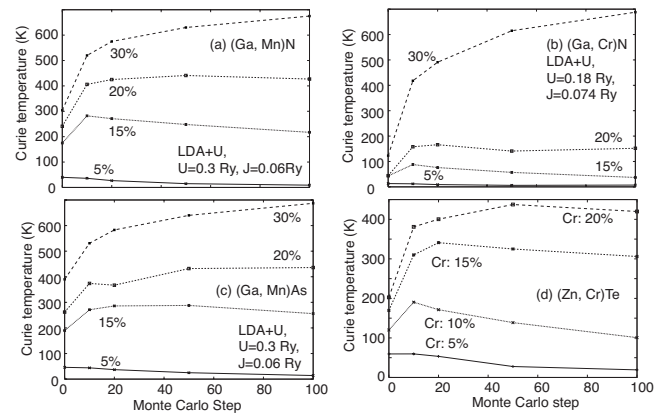

FIG. 56. T_C^{RPA} of (a) (Ga,Mn)N, (b) (Ga,Cr)N, (c) (Ga,Mn)As, and (d) (Zn,Cr)Te as a function of the number of Monte Carlo steps per impurity. As increasing the Monte Carlo steps, the phase separation develops. For higher concentrations. T_C increases due to the increased percolation path by clustering. On the other hand, for lower concentrations, T_C decreases and the system becomes superparamagnetic.

increasing number of MC steps the spinodal decomposition proceeds, leading to a random connecting network of TM impurities. Consequently, for high TM concentrations T_C increases with increasing number of MC steps, as shown in Fig. 56. However, the increase in T_C is significant only for high concentrations and the spinodal decomposition suppresses T_C for low concentrations. This is reasonable because for low concentrations TM impurities form only small clusters which are far away from each other. The ferromagnetic interactions between the clusters are negligible and the system becomes superparamagnetic ($T_C=0$) (Sato *et al.*, 2005).

2. Superparamagnetic blocking phenomenon in DMSs

As shown in Fig. 56, the spinodal decomposition helps ferromagnetism only for high concentrations. However, as shown in Fig. 55(b), rather large clusters can be formed under layer-by-layer crystal growth conditions even for low concentrations. If the clusters are large enough, a superparamagnetic blocking phenomenon becomes important and affects the magnetization process (Aharoni, 2000). For example, if the cluster size is smaller than the domain wall size, the magnetization process is governed by a uniform rotation of the magnetization. Then to flip the magnetization direction the magnetic anisotropy energy should be overcome. The energy barrier due to magnetic anisotropy leads to a finite relaxation time for reversing the magnetization and to hysteresis in the magnetization curve. The relaxation time τ follows the relation $1/\tau \propto \exp(-KV/k_BT)$, where K, V, T, and k_B are the anisotropy constant, volume of the cluster, temperature, and Boltzmann constant. This relation shows that as the cluster size becomes larger, the relaxation time becomes longer. If the relaxation time is longer than the observation time for the magnetization process, a hysteresis loop is observed in the magnetization curve, even if there is no ferromag-
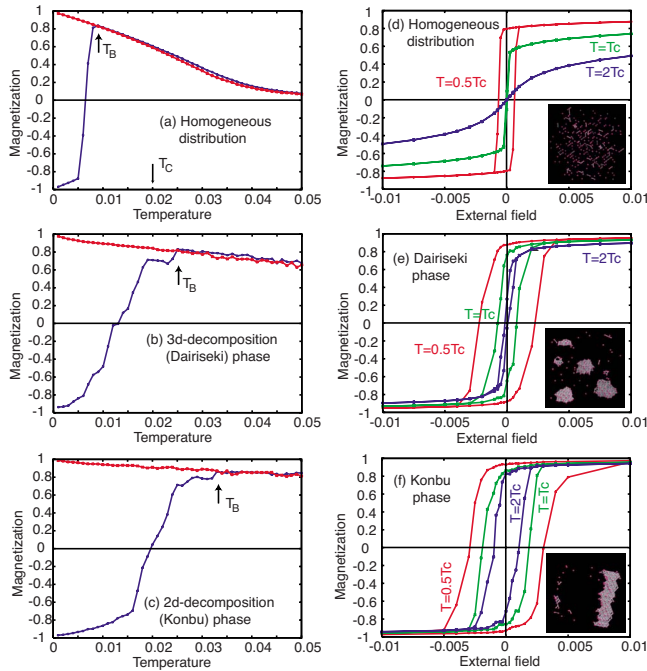
FIG. 57. (Color online) Simulated results of the superparamagnetic blocking phenomenon in (Ga,Mn)N. Left-hand panels: Magnetization as function of temperature starting from parallel or antiparallel configurations of initial magnetization to the external field. Right-hand panels: Magnetization as a function of external field. The simulations are performed for homogeneous Mn distribution [(a) and (d)], dairiseki phase [(b) and (e)], and konbu phase [(c) and (f)]. The insets in the lower panels show snapshots of Mn distribution in (Ga,Mn)N for the respective phases. Temperature ($k_B T$) and external field are scaled by the strength of the nearest-neighbor interaction $|J_{01}|$. From Sato *et al.*, 2007.

netic correlation between the clusters and T_C of the whole system is practically zero. This phenomenon is called superparamagnetic blocking (Aharoni, 2000).

A simulation of the blocking phenomenon by use of the Monte Carlo method was proposed by Dimitrov and Wysin (1996). Using this method we simulated the blocking phenomenon of a DMS material and discussed the effects of the spinodal decomposition (Sato, Fukushima, and Katayama-Yoshida, 2007a). Figure 57 shows these MCS results for various decomposition phases. The simulations were performed for homogeneous (Ga,Mn)N as well as (Ga,Mn)N in the dairiseki phase and (Ga,Mn)N in the konbu phase. In Fig. 57 the magnetization is shown as a function of temperature (left-hand panels) and of external field (right-hand panels). The snapshots of the Mn distribution in the various phases are shown in the insets of the lower panels of Fig. 57. As explained and shown in the insets, the size of the clusters in the konbu phase is larger than in the dairiseki phase and in the homogeneous phase only small clusters can be found.

The temperature dependence of the magnetization is calculated by increase of the temperature under a small external magnetic field for two initial conditions: with the initial direction of the magnetization parallel and

antiparallel to the external field. Above the blocking temperature the magnetization in the antiparallel configuration flips and the two lines coincide. As shown on the left-hand panels, the blocking temperature is significantly enhanced by the formation of clusters. The formation of larger clusters in the konbu phase results in a higher blocking temperature than in the dairiseki phase. T_C of homogeneous (Ga,Mn)N is indicated by the arrow in Fig. 57(a). Note that the dairiseki and konbu phases are superparamagnetic and that the total magnetization of the system is zero at finite temperature. In the present simulations the maximum cluster size is limited by the supercell size used. For larger supercells, larger clusters can be produced with sizes comparable to those actually observed in experiment, and higher blocking temperatures are expected.

In the right-hand panels in Fig. 57, the simulated hysteresis loops are shown for the three phases of (Ga,Mn)N. The simulations were performed for three temperatures, $T = T_C$, $0.5T_C$, and $2T_C$, where T_C is the ordering temperature of homogeneous (Ga,Mn)N with the same Mn concentration. In the homogeneous case [Fig. 57(d)], above T_C, the hysteresis loop closes and the magnetic response becomes very weak for $T = 2T_C$. On the other hand, in the dairiseki and konbu phases, due to the formation of clusters, we still observe hysteresis loops even at $T = 2T_C$. The hysteresis loop is widest for the Konbu phase as shown in Fig. 57(f).

Thus, these simulations show that the magnetic properties of a DMS are considerably affected by inhomogeneity caused by spinodal decomposition and clustering. Under the thermal nonequilibrium crystal growth method, it is difficult to control at which stage the clustering is stopped, so that the cluster size and its distribution depend on the crystal growth conditions. As a result, the magnetic properties of DMS materials strongly depend on the details of the experimental conditions. It is very likely that this is why the reported experimental T_C values scatter so much.

VII. TRANSPORT PROPERTIES OF DILUTE MAGNETIC SEMICONDUCTORS

The potential of using DMS materials in spintronic applications requires good knowledge of the transport properties of these systems, such as the anisotropic magnetoresistance, the Hall resistivity, magneto-optical properties, etc. (Ohno, 1999; Matsukura *et al.*, 2002). Some of these properties are consequences of the simultaneous presence of spin polarization and spin-orbit interaction and/or they are directly related to off-diagonal elements of the conductivity tensor. Among different scattering mechanisms responsible for a finite life-time of the carriers in DMS materials, three contributions must in general be addressed: scattering (i) by phonons, (ii) by magnons, and (iii) due to various impurities, both magnetic atoms inherent to DMS and structural defects.

The complexity of the transport behavior of DMS systems represents a difficult task for a truly first-principles approach. Existing systematic *ab initio* studies have thus

focused on the zero-temperature residual resistivity due to the impurity scattering. This effort is a natural continuation of a long-term successful application of the CPA to random metallic alloys (Butler, 1985), including spontaneous galvanomagnetic phenomena (Banhart and Ebert, 1995), effects of partial long-range ordering (Banhart and Czycholl, 2002), etc.

The CPA is an effective medium theory of chemical randomness and so provides a satisfactory description of electron states in metallic systems with the Fermi energy lying deep inside the bands. However, DMSs are characterized by a Fermi energy close to the band gap of the parent semiconductor where the CPA might be less reliable. The situation is even worse in DMS systems with an impuritylike band formed inside the semiconductor band gap, for example, Mn-doped GaN, where localized states appear, the conductivity is dominated by a hopping mechanism, and any simple mean-field theory fails. For these reasons, the *p*-type Mn-doped GaAs can be considered as a suitable DMS system for first applications of state-of-the-art *ab initio* techniques. Since the main origin of the calculated residual resistivities lies in the filling of the majority valence band (number of holes) and in the impurity scattering that is especially strong at the Fermi energy (see Fig. 31), possible effects of the weaker spin-orbit interaction (owing to the *p* orbitals of As atoms) have been neglected in all existing *ab initio* studies. The effect of spin-orbit coupling on the resistivity due to the mixing of two spin channels is greatly suppressed in half-metallic systems like (Ga, Mn)As.

A. Kubo-Greenwood linear response theory

The symmetric part of the zero-frequency conductivity tensor at zero temperature is given by the Kubo-Greenwood formula as (Kubo, 1957; Greenwood, 1958; Velický, 1969)

$$\sigma^{\mu\nu} \propto \mathrm{Tr}\langle \delta(E_F - H)j^\mu \delta(E_F - H)j^\nu \rangle, \tag{41}$$

where $\mu, \nu = x, y, z$ are the Euclidean indices, E_F denotes the Fermi energy, j^μ is the current operator, H is the random one-particle Hamiltonian, and $\langle \cdots \rangle$ denotes the configurational averaging. For spin-polarized systems with collinear spin structures and with neglected spin-orbit interaction, the resulting conductivity tensor can be expressed as a sum over two spin channels s ($s = \uparrow, \downarrow$), namely, $\sigma^{\mu\nu} = \sigma^{\mu\nu,\uparrow} + \sigma^{\mu\nu,\downarrow}$ (two-current model). The residual resistivity ρ and the conductivity σ are then given by

$$\rho = \sigma^{-1}, \quad \sigma = \sigma^\uparrow + \sigma^\downarrow, \quad \sigma^s = \sigma^{\mu\mu,s}, \tag{42}$$

where the spin-resolved conductivities σ^s of cubic systems are equal to the diagonal elements of the spin-dependent conductivity tensor $\sigma^{\mu\nu,s}$ ($\sigma^{xx,s} = \sigma^{yy,s} = \sigma^{zz,s}$). The configurational average in Eq. (41) can be reduced to averages of the form (Weinberger, 1990)
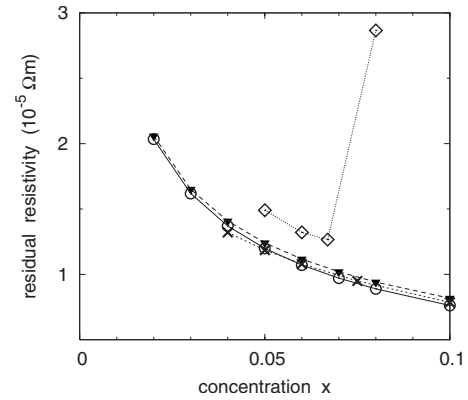

FIG. 58. Residual resistivity of the $(Ga_{1-x}Mn_x)As$ alloy as a function of the Mn concentration x calculated using the TB-LMTO method (Turek *et al.*, 2004) from the total conductivity (○) and its coherent part (▼), and using the KKR method (Lowitzer *et al.*, 2007) (×). Experimental values for annealed thin films (Edmonds *et al.*, 2002b) are displayed as well (◇).

$$\mathrm{Tr}\langle G^s(z)j^\mu G^s(z')j^\nu \rangle = \mathrm{Tr}[\bar{G}^s(z)j^\mu \bar{G}^s(z')j^\nu]$$
$$+ \xi^{\mu\nu,s}(z,z'), \tag{43}$$

where $G^s(z)$ denotes the Green's function (resolvent) for spin s, the energy arguments z, z' acquire two values $E_F^+ = E_F + i0$ and $E_F^- = E_F - i0$, and $\bar{G}^s(z) = \langle G^s(z) \rangle$ denotes the configurationally averaged Green's function. The first term in Eq. (43) represents the coherent part while the second term includes the corresponding vertex corrections to the transport.

The TB-LMTO-CPA method employs the concept of intersite electron transport (Turek *et al.*, 2002) which leads to effective current operators j^μ in Eq. (41) that are nonrandom quantities. The vertex corrections in Eq. (43) can then be formulated in a standard way (Velický, 1969); the details are given in Turek *et al.* (2004) and Carva *et al.* (2006). The KKR-CPA approach (Butler, 1985; Weinberger, 1990) rests on electron motion in the continuous real space. Consequently, the operators j^μ are represented by site-diagonal but random matrices and the averaging in Eq. (43) including the vertex contribution is more involved [see Butler (1985) for details]. It has recently been shown that the KKR and TB-LMTO approaches lead to similar results not only for random metallic alloys (Turek *et al.*, 2002, 2004) but also for DMS systems (Lowitzer *et al.*, 2007).

B. Residual resistivity of defect-free (Ga,Mn)As

The residual resistivity ρ of the bulk $(Ga_{1-x}Mn_x)As$ alloy without structural defects as obtained by the TB-LMTO method (Turek *et al.*, 2004) and the KKR method (Lowitzer *et al.*, 2007) is summarized in Fig. 58 together with values measured at liquid helium temperature for annealed thin (Ga,Mn)As films (Edmonds *et al.*, 2002b). It can be seen that theoretical values of ρ for Mn concentration $x \sim 0.05$ lie in the range $(0.5-2) \times 10^{-5}$ Ωm in good agreement with experiment (Ohno,

1999; Edmonds *et al.*, 2002b). Note that the values of ρ for diluted (Ga,Mn)As are at least one order of magnitude larger than the residual resistivity of concentrated metallic alloys. Another difference can be seen in the concentration dependence of the resistivity (Fig. 58): $\rho(x)$ decreases with increasing concentration of Mn impurities, at least for concentrations lower than 7%, which is opposite to the trend that is encountered in metallic alloys.

The calculated dependence of $\rho(x)$ can be explained by a competition of two mechanisms in the (Ga,Mn)As system (Turek *et al.*, 2004): (i) the increase in ρ with increasing concentration of Mn atoms which is due to impurity scattering; and (ii) the increase in the conductivity, i.e., the decrease in ρ, with increasing number of holes in the valence band, which in turn is proportional to the Mn concentration. Such a strong dependence on the number of carriers is missing in typical metallic alloys. It should be noted that the defect-free (Ga,Mn)As system has a completely filled minority ($s=\downarrow$) valence band (half-metallic behavior) so that $\sigma^{\downarrow}=0$, and the current is carried only by majority ($s=\uparrow$) electrons, $\rho=1/\sigma^{\uparrow}$. Comparison to the experimental values of Edmonds *et al.* (2002b) (Fig. 58) for $0.05 \leqslant x \leqslant 0.067$ provides an independent check of the reliability of both *ab initio* CPA schemes, whereas the markedly higher resistivity measured for $x=0.08$ reflects a high amount of As antisites in the prepared sample (Edmonds *et al.*, 2002b).

1. Role of the vertex corrections

Both theoretical approaches, TB-LMTO (Turek *et al.*, 2004) and KKR (Lowitzer *et al.*, 2007), revealed that the conductivity of bulk (Ga,Mn)As is dominated by the coherent part while the incoherent part (vertex corrections) is negligible (Fig. 58). This fact, however, cannot be interpreted as a weak-scattering regime of the system. A recent study of the current perpendicular to plane (CPP) conductance for (001) slabs of defect-free (Ga,Mn)As attached to nonmagnetic bcc Cr(001) leads (Carva *et al.*, 2006) indicates a more complicated picture of the CPP transport. The dependence of the majority-spin conductance on the slab thickness exhibits two different slopes: a rapid decrease for thin slabs followed by a much slower decrease for thick slabs and the minority-spin conductance decreases exponentially with the thickness over the entire interval studied. These features are compatible with the half metallicity of the bulk (Ga,Mn)As.

The minority-spin channel exhibits a tunneling transport regime while the majority-spin channel approaches an Ohmic regime for thick slabs where the conductance is dominated by the incoherent part (Carva *et al.*, 2006). These trends indicate that the intrinsic disorder of the (Ga,Mn)As slabs is strong enough to destroy the coherence after a very short distance traveled by the electrons, in qualitative agreement with the effects of strong disorder (nonquasiparticle behavior) manifested in the majority-spin Bloch spectral function at the Fermi level (see Fig. 31).
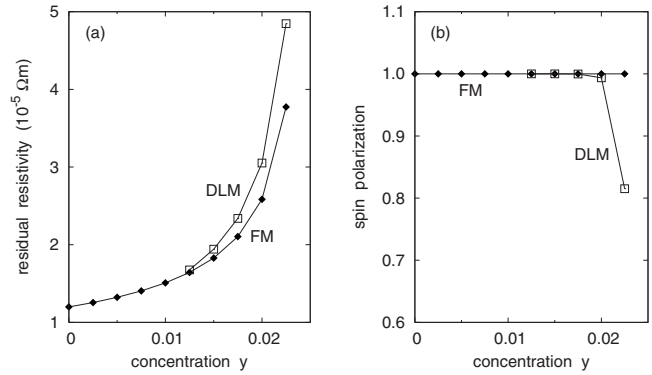

FIG. 59. Effect of As antisites on the transport properties of (Ga,Mn)As. (a) Residual resistivity and (b) spin polarization of the conductivities as function of the As antisite concentration y in the bulk ($Ga_{0.95-y}Mn_{0.05}As_y$) alloy in the ferromagnetic (FM, ♦) and the uncompensated disordered-local-moment (DLM, □) state (Turek *et al.*, 2006). Influence of As antisites and of magnetic order on transport properties of Mn-doped GaAs.

C. Influence of native defects on transport properties

The effect of native compensating defects on the resistivity of (Ga,Mn)As and on the spin polarization of the conductivity, defined as $P=(\sigma^{\uparrow}-\sigma^{\downarrow})/(\sigma^{\uparrow}+\sigma^{\downarrow})$, is shown in Fig. 59 for As antisites, simulated by alloys of composition ($Ga_{1-x-y}Mn_xAs_y$)As, and in Fig. 60 for Mn interstitials, simulated by systems ($Ga_{1-x+z}Mn_{x-z}$)AsMn$_z^i$. In general, both types of defects lead to an increase in ρ, which can be ascribed to a combined effect of increased impurity scattering and reduced number of carriers (Turek *et al.*, 2004, 2006).

1. Effect of As antisites

The presence of As antisites leads to a phase transition in the magnetic ground state of the alloy: the FM state becomes unstable for higher concentration y of As antisites and a more complex magnetic order appears,
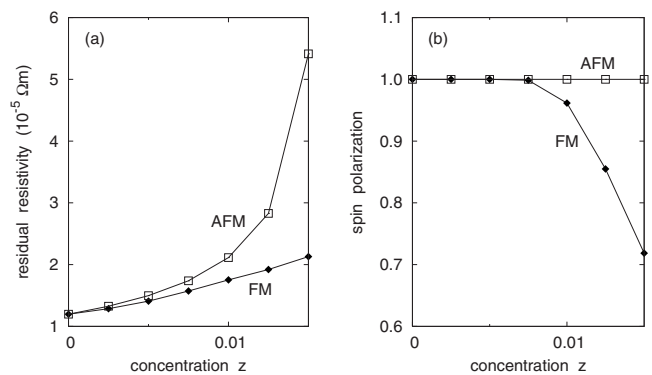

FIG. 60. Effect of Mn interstitials on the transport properties of (Ga,Mn)As. (a) Residual resistivity and (b) spin polarization of the conductivities as functions of the Mn interstitial concentration z in the bulk ($Ga_{0.95+z}Mn_{0.05-z}$)AsMn$_z^i$ alloy in the ferromagnetic (FM, ♦) and the antiferromagnetic (AFM, □) state. From Turek *et al.*, 2006. Influence of Mn interstitials and of magnetic order on transport properties of Mn-doped GaAs.

simulated here by an uncompensated DLM state (Korzhavyi *et al.*, 2002; Kudrnovský *et al.*, 2003); see also Fig. 38(a). The resistivity increases with the As antisite concentration irrespective of the particular magnetic state and it diverges in the fully compensated case ($y \rightarrow 0.025$ for $x = 0.05$) [see Fig. 59(a)], which proves that the dominating effect is the reduction of the number of carriers with increasing y. The resistivity of the FM state is smaller than of the DLM state because the magnetic disorder leads to an additional scattering.

As documented in Fig. 59(b), the conductivities in both magnetic states remain fully polarized for quite high As antisite concentration $y \leq 0.02$, despite the large changes of the resistivity values in the same interval. The full spin polarization can be explained from the known spin-polarized densities of states at the Fermi energy E_F (Korzhavyi *et al.*, 2002; Kudrnovský *et al.*, 2004). The half-metallic behavior of the alloy that leads to full polarization in the FM state is not modified by As antisites, causing mainly a shift of E_F toward the top of the majority-spin valence band (Kudrnovský *et al.*, 2004). The reversal of a few Mn moments in the (Ga,Mn)As alloy without As antisites leads to the appearance of a sharp Mn-related peak in the minority DOS located just at E_F. The presence of As antisites results again in an upward shift of the Fermi level that reduces the minority DOS at E_F to a negligible value (Korzhavyi *et al.*, 2002). This shift of E_F contributes then to energetic stabilization of the uncompensated DLM state as well as to the full spin polarization of the DLM conductivities.

2. Effect of Mn interstitials

The effect of Mn interstitials on ρ for alloys with total Mn content (substitutional and interstitial Mn atoms) fixed to $x = 0.05$ is shown in Fig. 60(a) for both parallel (FM state) and antiparallel [antiferromagnetic (AFM) state] orientations of the two local Mn moments; the ground state corresponds to the AFM state (Mašek and Máca, 2004). The resistivity increases with the Mn interstitial content z for both states; however, the two dependences differ from each other. In particular, the AFM resistivity increases quickly for compositions approaching the fully compensated state ($z \rightarrow 0.0167$ for $x = 0.05$), whereas the FM resistivity increases nearly linearly with z.

This qualitative difference can be understood in terms of the spin-polarized DOS studied for the compensated alloy (Turek *et al.*, 2004). The AFM state exhibits a conventional half-metallic behavior with E_F in the gap of the minority states [see Fig. 3(a) in Turek *et al.* (2004)]. The large resistivity is because the Fermi level lying in an energy region of strongly disordered Mn interstitial states formed in the majority band gap. On the contrary, E_F for the FM case lies in the minority Mn interstitial states at the bottom of the conduction band [see Fig. 3(b) in Turek *et al.* (2004)], so that both spin channels contribute to the conductivity and the resistivity is smaller than in the AFM case. The different DOSs in the two magnetic states are also responsible for different
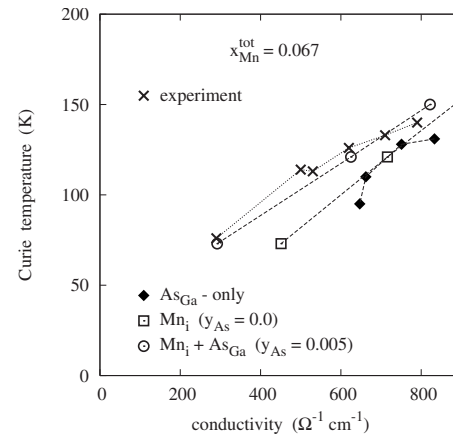

FIG. 61. Relation between Curie temperature and conductivity as calculated for three different models of the (Ga,Mn)As alloy with the nominal Mn content $x_{\mathrm{Mn}}^{\mathrm{tot}} = 0.067$, assuming that compensating defects are As antisites ($\blacklozenge$), Mn interstitials ($\square$), and both ($\bigcirc$) (Kudrnovský *et al.*, 2007). Experimental values for as-grown and annealed thin films are also shown ($\times$).

spin polarization of the conductivities [see Fig. 60(b)]. The AFM conductivities are fully polarized in the whole concentration interval, whereas the polarization of the FM conductivities becomes reduced significantly for Mn interstitial content $z \geq 0.01$.

D. Relation between conductivity and Curie temperature

Experimental investigations of DMS materials indicate a strong relation between Curie temperature T_C and conductivity σ (Edmonds *et al.*, 2002b). Both quantities depend nontrivially on the concentration of magnetic impurities, the carrier density, and the presence of compensating defects. As shown in a recent theoretical study for Mn-doped GaAs (Kudrnovský *et al.*, 2007), first-principles tools can reproduce roughly the measured T_C-σ relation and shed some light on the dominating structure defects in the prepared samples.

The Curie temperature for (Ga,Mn)As alloys with both As antisites and Mn interstitials was calculated using the model of magnetically inactive pairs of a substitutional and an interstitial Mn atom as explained in Sec. IV.E. However, the conductivity calculation took into account all magnetic impurities and structure defects on equal footing. Three different models were considered: (i) with As antisites as the only compensating defects, (ii) with Mn interstitials as the compensating defects, and (iii) with a small concentration of As antisites in addition to Mn interstitials. The results are summarized in Fig. 61 together with experimental data for thin (Ga,Mn)As films (Edmonds *et al.*, 2002b) with a nominal Mn concentration $x_{\mathrm{Mn}}^{\mathrm{tot}} = 0.067$ after various stages of annealing, ranging from an as-grown sample (low T_C and σ) to an almost perfectly annealed sample (high T_C and σ).

The following conclusions can be made. (i) As antisites as the only compensating defects fail to reproduce both the experimental T_C and the conductivity, which seems to be too high in this model. (ii) The presence of

Mn interstitials significantly improves the agreement between theory and experiment by correctly reproducing the almost linear dependence of the T_C on the conductivity with an acceptable quantitative agreement. While the calculated Curie temperatures agree with experimental data well, the conductivity still seems to be slightly overestimated. (iii) The additional presence of a small amount of As antisites ($y_{As}=0.005$) reduces the conductivity, which brings the theory into a good quantitative agreement with experimental data.

VIII. SUMMARY

Diluted magnetic semiconductors have attracted substantial attention in both experimental and theoretical work. The large interest in these materials has motivated several articles. For instance, experimental and theoretical aspects of Mn-doped GaAs were reviewed by MacDonald *et al.* (2005) and Jungwirth *et al.* (2006). The current review focuses not on one particular material, but on the theoretical aspects of the whole group of DMS materials, where general trends of magnetism can be distinguished. Hence, we summarize in this review primarily the results of density-functional calculations for understanding dilute magnetic semiconductors, in particular their magnetic as well as their thermal properties. The approach we focus on primarily consists of a combination of *ab initio* methods for calculating the exchange coupling constants and statistical methods like Monte Carlo simulations to calculate the Curie temperature, assuming a Heisenberg model for the underlying magnetic interactions. Thus we review investigations that address the central problem for dilute ferromagnetic semiconductors: Do DMSs with Curie temperatures T_C well above room temperature exist, such that realistic applications are feasible? The hope for high-T_C values was raised by Dietl *et al.* (2000). However, this hope is so far not supported by *ab initio* calculations, which moreover indicate that many experimentally observed high-T_C values are due to smaller or larger magnetic clusters and segregated phases with very high impurity concentrations, but not to a homogeneous DMS.

In Sec. II we first discuss the hybridization of the transition-metal d states with the valence band p states, leading to bonding states in the valence band and antibonding states in the gap. We discuss multiple charge states of TM impurities and correlation effects due to screening. Calculations for lattice relaxations are reviewed; at least for the well-known (Ga,Mn)As system they are not important in real technological applications. Then we discuss the electronic structure of concentrated DMSs by applying the coherent potential approximation. This workhorse for alloy theory provides a useful mean-field description of the electronic structure. The application to III-V and II-VI DMSs reveals simple trends for the filling of the gap states, and at the same time large differences between, for example, Mn in wide-gap and narrow-gap DMSs. Within this mean-field treatment of the electronic structure the energetic stability of the ferromagnetic state versus the disordered local moment state shows clear trends.

Section III discusses the role of exchange interactions in DMSs. First the relation between the exchange coupling constants J_{ij} and the Curie temperature in the mean-field approximation is derived. The next central topic concerns the evaluation of the J_{ij} interactions from the basic electronic structure. The method of choice is due to Liechtenstein *et al.* (1987) but is generalized to a disordered medium as described by the coherent potential approximation. By asymptotic analysis these coupling constants show an exponential decrease with distance, superimposed on an oscillatory RKKY-like behavior. The exponential decrease is to a large extent the result of the half-metallic behavior of DMSs, i.e., the band gap in the minority band, and is particularly important for wide-band-gap semiconductors, for which the interaction is very short ranged. Additional damping arises for larger concentrations and larger distances from the impurity-impurity scattering. Longer-ranged interactions occur only for relatively narrow band gaps, in particular for GaAs and GaSb. Here the exponential decay due to half metallicity is less pronounced, and moreover the disorder scattering is reduced, since the d states of the impurities are centered well below E_F.

Simple models for the understanding of the exchange mechanisms are presented. Double exchange is the dominating mechanism for wide-band-gap semiconductors like GaN or ZnO. Here the atomic p levels of N and O are low in energy, leading to deep-lying p valence bands and a large band gap. For the same reason the transition-metal d states form impurity bands in the gap, which determine the magnetic interactions. Therefore double exchange is very strong and short ranged. The opposite behavior occurs for relatively narrowband DMSs like (Ga,Mn)As and (Ga,Mn)Sb. Here the atomic p levels are higher in energy, leading, on the one hand, to narrower band gaps and, on the other hand, to the majority d state of Mn being centered in the lower region of the valence p band. This leads to an increased importance of Zener's p-d exchange, which is relatively weak but longer ranged. Note that of all $3d$ impurities this situation can occur only for Mn, since only for this element is the majority d level sufficiently low, while the minority d level is still empty. With these exceptions, the normal dominating mechanism for ferromagnetism in DMSs is double exchange.

Superexchange is the dominant antiferromagnetic interaction, leading to the disordered local moment phase of DMSs. It is also rather strong and basically also restricted to nearest neighbors. It is largest when the Fermi level falls in the gap between the majority and minority impurities. If E_F lies in the impurity bands, it competes with ferromagnetic double exchange. In total, a rather simple and universal behavior of the exchange interaction as a function of the Fermi energy with respect to the impurity levels is obtained.

Section IV discusses evaluation of the finite-temperature properties based on a classical Heisenberg

model, with the exchange integrals calculated by *ab initio* methods. Technically the Curie temperatures T_C are calculated with the local random-phase approximation and Monte Carlo method, which is numerically exact but requires a larger effort. Most important is that the mean-field approximation grossly overestimates the Curie temperatures of dilute systems, since the magnetic behavior is dominated by percolation problems. For a disordered diluted system on a fcc lattice (this corresponds to the Mn sublattice in a zinc-blende structure), the percolation threshold for nearest-neighbor interactions amounts to a concentration of 20%, independently of the strength of this interactions. Thus below 20%, in particular in the typical concentration range of 5–8 % of DMS systems, no ferromagnetism can occur for nearest-neighbor interactions only, since the impurities cannot see and talk to each other magnetically. In other words, in this concentration range the Curie temperatures are determined only by longer-ranged interactions, while in the mean-field approximation a strong nearest-neighbor interaction erroneously leads to a high Curie temperature. Since the ferromagnetism in most DMS systems is dominated by double exchange, being strong for the nearest neighbors but weak for the other neighbors, this seriously limits the Curie temperatures of DMSs, an important fact that was only recently realized (Bergqvist *et al.*, 2004; Sato, Schweika, *et al.*, 2004). Quantitatively the Curie temperature of (Ga,Mn)N with 5% Mn is overestimated in the mean-field approximation by a factor of 6. Even in (Ga,Mn)As, for which the exchange interaction is more extended, the MFA gives a value that is a factor of 2 too high. For the experimentally well investigated case of (Ga,Mn)As, the results obtained by Monte Carlo calculations agree well with the experiments as well as with the LRPA results.

In Sec. V we review the results of some other DMS systems, which have been investigated. The first example is the wide-gap semiconductor SiO_2 doped with transition metals. Consequently, the ferromagnetism in these systems, for example, in $(Si,V)O_2$ and $(Si,Mn)O_2$, is caused by double exchange. While high-T_C values are obtained for $(Si,Mn)O_2$ in the MFA, these are expected to be strongly suppressed by the percolation effect. The second example is the semiconductor $CuAlO_2$, doped with TM impurities on the Cu sublattice. In this system the magnetism is due to narrow impurity bands in the gap and ferromagnetism is caused by double exchange, characterized by strong nearest-neighbor interaction. In the dilute limit, the Curie temperatures are strongly suppressed. Even for a concentration of 20% of TM impurities, the largest T_C obtained in these calculations is below 100 K for $(Cu,Fe)AlO_2$. The last system family to be discussed is DMSs based on semiconducting Heusler alloys. Here we consider the nonmagnetic half-Heusler alloys CoTiSb and NiTiSn, both doped with 5% Mn. Strong ferromagnetism due to double exchange is found for the last two systems, but again the coupling constants are large only for the first neighbors. Thus high Curie temperatures cannot be obtained in the dilute limit; rather Mn concentrations of 25% [in Ni(Ti,Mn)Sn] or

30% [in Co(Ti,Mn)Sb] are necessary for Curie temperatures around room temperature.

Concluding from the discussion of Secs. III–V, we state that there exists a general obstacle to obtaining high Curie temperatures for DMSs, i.e., well above room temperature. In most systems ferromagnetism is driven by double exchange, representing a strong nearest-neighbor interaction, but exponentially small interactions for further neighbors, since below the percolation threshold of 20% (for a fcc lattice with NN interaction), magnetic percolation can only be caused by the weak longer-ranged interaction. This leads to very low Curie temperatures in the physically most interesting concentration region of 5–10 %. The physics is somewhat different for Mn-doped semiconductors with heavier cations, like GaAs or GaSb, where the Mn *d* level is located deep in the valence band. Here the ferromagnetism has an important contribution also from Zener's *p-d* exchange, which is longer ranged and therefore not as much influenced by the percolation problem, resulting in a reduction of the MFA T_C value for 5% Mn in GaAs by only about 50%. But the size of this interaction is rather small, so that in this case also the Curie temperatures are not sufficiently high.

We conclude therefore that the Curie temperature can be significantly increased only if routes are found to increase the impurity concentrations, since then restrictions arising from the percolation effect are reduced. An example for this is the codoping method, for example, trying to increase the TM solubility by codoping with donor atoms.

A second possibility for effectively increasing the concentration is discussed in Sec. VI. The idea is to profit from the metastability of the homogeneous phase and to form, by spinodal decomposition during annealing, small clusters and aggregates of defects with a higher local concentration of magnetic impurities. The kinetic Monte Carlo simulations based on *ab initio* potentials for the interaction reveal that by three-dimensional decomposition large nonoverlapping clusters are formed, which show a superparamagnetic behavior with a relatively high blocking temperature. For higher concentrations (above 20%) a 3D network of percolating clusters with substantially increased Curie temperatures can be obtained. Of more interest for applications is the two-dimensional decomposition in the surface layer and the resulting controlled growth of magnetic columns perpendicular to the surface, which can be controlled by nanoscale seeding and changes of the metal vapor pressure. These two-dimensional columns show a strongly increased blocking temperature. In total, the simulations show that the size, shape and distribution of the clusters strongly depend on the crystal growth conditions, thus providing a simple understanding of why the reported experimental T_C values scatter so strongly.

The last section reviews the state of the art in understanding and predicting the residual resistivity of DMS. The method used is the Kubo-Greenwood linear response formalism, combined with the coherent potential approximation and including vertex correction. This

method is the workhorse for resistivity calculations of metallic alloys and surprisingly also gives excellent results for (Ga,Mn)As despite the large number of defects and the nearly insulating behavior. Calculations show that the transport is totally dominated by the majority band and that vertex corrections are of minor importance. Most important is the simulation of native defects, i.e., As antisites and Mn interstitials. While the resistivity strongly increases with the concentration of these defects, the conductance remains fully spin polarized up to large concentrations, in particular for As antisites, arising from the shift of the Fermi level to higher energies, which conserves half metallicity up to large concentrations of compensating defects. Experimental investigations of DMS systems indicate an interesting nearly linear relation between the Curie temperature and the conductivity, two quantities which from the theoretical point of view are very different. However, the calculations indeed give a linear behavior, provided the compensating defects are (mostly) Mn interstitials, while for only As antisites a pronounced nonlinear behavior is obtained, in contradiction to the experiments.

In conclusion, we stress that *ab initio* calculations have led to substantial progress in the understanding and prediction of the magnetic properties of DMSs. Most important is the identification of two ferromagnetic exchange mechanisms, i.e., double exchange and *p-d* exchange, with different properties and valid for two different classes of materials. Even more important is the identification of magnetic percolation as a basic obstacle to obtaining high Curie temperatures in the dilute concentration range of 5–10 %. The results of *ab initio* calculations seem to suggest that it is rather unlikely to obtain T_C values as high as room temperature or above in this range. The percolation problem might be overcome if it is possible to substantially increase the concentration of magnetic impurities. This could be achieved by increasing the solubility by suitable co-dopants or by increasing the effective local concentration by spinodal decomposition and self-organized growth.

REFERENCES

Aharoni, A., 2000, *Introduction to the Theory of Ferromagnetism* (Oxford University Press, Oxford), p. 92.

Akai, H., 1989, J. Phys.: Condens. Matter **1**, 8045.

Akai, H., 1998, Phys. Rev. Lett. **81**, 3002.

Akai, H., 2002, http://sham.phys.sci.osaka-u.ac.jp/~kkr/

Akai, H., and P. H. Dederichs, 1993, Phys. Rev. B **47**, 8739.

Andersen, O. K., H. L. Skriver, H. Nohl, and B. Johansson, 1980, Pure Appl. Chem. **52**, 93.

Anderson, P. W., 1950, Phys. Rev. **79**, 350.

Anderson, P. W., 1961, Phys. Rev. **124**, 24.

Anderson, P. W., 1963, in *Solid State Physics*, edited by F. Seitz and D. Turnbull (Academic, New York), Vol. 14, p. 99.

Anderson, P. W., 1975, Phys. Rev. Lett. **34**, 953.

Anderson, P. W., and H. Hasegawa, 1955, Phys. Rev. **100**, 675.

Anisimov, V. I., F. Aryasetiawan, and A. I. Lichtenstein, 1997, J. Phys.: Condens. Matter **9**, 767.

Antropov, V. P., B. N. Harmon, and A. N. Smirnov, 1999, J. Magn. Magn. Mater. **200**, 148.

Baibich, M. N., J. M. Broto, A. Fert, F. Nguyen van Dau, F. Petroff, P. Etienne, G. Cruzet, A. Friederich, and J. Chazelas, 1988, Phys. Rev. Lett. **61**, 2472.

Banhart, J., and G. Czycholl, 2002, Europhys. Lett. **58**, 264.

Banhart, J., and H. Ebert, 1995, Europhys. Lett. **32**, 517.

Beeler, F., O. K. Andersen, and M. Scheffler, 1985, Phys. Rev. Lett. **55**, 1498.

Belhadji, B., R. Zeller, P. H. Dederichs, K. Sato, and H. Katayama-Yoshida, 2007, J. Phys.: Condens. Matter **19**, 436227.

Bergqvist, L., O. Eriksson, J. Kudrnovský, V. Drchal, A. Bergman, L. Nordström, and I. Turek, 2005, Phys. Rev. B **72**, 195210.

Bergqvist, L., O. Eriksson, J. Kudrnovský, V. Drchal, P. Korzhavyi, and I. Turek, 2004, Phys. Rev. Lett. **93**, 137202.

Bergqvist, L., P. A. Korzhavyi, B. Sanyal, S. Mirbt, I. A. Abrikosov, L. Nordström, E. A. Smirnova, P. Mohn, P. Svedlindh, and O. Eriksson, 2003, Phys. Rev. B **67**, 205201.

Binasch, G., P. Gruenberg, F. Saurenbach, and W. Zinn, 1989, Phys. Rev. B **39**, 4828.

Binder, K., and D. W. Heermann, 2002, *Monte Carlo Simulation in Statistical Physics* (Springer, Berlin), p. 39.

Blackman, J. A., and R. J. Elliott, 1969, J. Phys. C **2**, 1670.

Bonanni, A., 2007, Semicond. Sci. Technol. **22**, R41.

Bonanni, A., M. Kiecana, C. Simbrunner, T. Li, M. Sawicki, M. Wegscheider, M. Quast, H. Przybylinska, A. Navarro-

Quezada, R. Jakiela, A. Wolos, W. Jantsch, and T. Dietl, 2007, Phys. Rev. B **75**, 125210.

Bouzerar, G., 2007, EPL **79**, 57007.

Bouzerar, G., R. Bouzerar, and O. Cepas, 2007, Phys. Rev. B **76**, 144419.

Bouzerar, G., R. Bouzerar, J. Kudrnovský, and T. Ziman, 2006, Phys. Status Solidi A **203**, 2989.

Bouzerar, G., and P. Bruno, 2002, Phys. Rev. B **66**, 014410.

Bouzerar, G., J. Kudrnovský, L. Bergqvist, and P. Bruno, 2003, Phys. Rev. B **68**, 081203(R).

Bouzerar, G., T. Ziman, and J. Kudrnovský, 2004 Appl. Phys. Lett. **85**, 4941.

Bouzerar, G., T. Ziman, and J. Kudrnovský, 2005a, Europhys. Lett. **69**, 812.

Bouzerar, G., T. Ziman, and J. Kudrnovský, 2005b, Phys. Rev. B **72**, 125207.

Bouzerar, R., G. Bouzerar, and T. Ziman, 2006, Phys. Rev. B **73**, 024411.

Bouzerar, R., G. Bouzerar, and T. Ziman, 2007, EPL **78**, 67003.

Bruno, P., 1995, Phys. Rev. B **52**, 411.

Bruno, P., and C. Chappert, 1991, Phys. Rev. Lett. **67**, 1602.

Bruno, P., J. Kudrnovský, V. Drchal, and I. Turek, 1996, Phys. Rev. Lett. **76**, 4254.

Butler, W. H., 1985, Phys. Rev. B **31**, 3260.

Callen, H. B., 1963, Phys. Rev. **130**, 890.

Carva, K., I. Turek, J. Kudrnovský, and O. Bengone, 2006, Phys. Rev. B **73**, 144421.

Ceperley, D. M., and B. J. Alder, 1980, Phys. Rev. Lett. **45**, 566.

Cheng, X. M., and C. L. Chien, 2003, J. Appl. Phys. **93**, 7876.

Chiba, D., *et al.*, 2003, Appl. Phys. Lett. **82**, 3020.

Coey, J. M. D., M. Venkatesan, and C. B. Fitzgerald, 2005, Nature Mater. **4**, 173.

Dalpian, G. M., S. H. Wei, X. G. Gong, A. J. R. da Silva, and A. Fazzio, 2006, Solid State Commun. **138**, 353.

de Gennes, P. G., 1960, Phys. Rev. **118**, 141.

de Gennes, P. J., 1962, J. Phys. Radium **23**, 630.

Dietl, T., H. Ohno, F. Matsukura, J. Cibert, and D. Ferrand, 2000, Science **287**, 1019.

Dimitrov, D. A., and G. M. Wysin, 1996, Phys. Rev. B **54**, 9237.

Dinh, V. A., and H. Katayama-Yoshida, 2005, J. Electron Microsc. **54**, i61.

Dinh, V. A., K. Sato, and H. Katayama-Yoshida, 2005, Solid State Commun. **136**, 1.

Dreizler, R., and E. Gross, 1995, *Density Functional Theory* (Plenum, New York).

Ducastelle, F., 1991, *Order and Phase Stability of Alloys* (North-Holland, Amsterdam).

Ducastelle, F., and F. Gautier, 1976, J. Phys. F: Met. Phys. **6**, 2039.

Dudarev, S. L., G. A. Botton, S. Y. Savrasov, C. J. Humphreys, and A. P. Sutton, 1998, Phys. Rev. B **57**, 1505.

Edmonds, K. W., P. Boguslawski, K. Y. Wang, R. P. Campion, S. N. Novikov, N. R. S. Farley, B. L. Gallagher, C. T. Foxon, M. Sawicki, T. Dietl, M. Buongiorno Nardelli, and J. Bernholc, 2004, Phys. Rev. Lett. **92**, 037201.

Edmonds, K. W., *et al.*, 2002a, Appl. Phys. Lett. **81**, 3010.

Edmonds, K. W., *et al.*, 2002b, Appl. Phys. Lett. **81**, 4991.

Epicier, T., and C. Esnouf, 1990, Philos. Mag. Lett. **61**, 285.

Eriksson, O., D. Iuşan, R. Knut, and B. Sanyal, 2007, J. Appl. Phys. **101**, 09H114.

Erwin, S. C., and A. G. Petukhov, 2002, Phys. Rev. Lett. **89**, 227201.

Faulkner, J. S., and G. M. Stocks, 1980, Phys. Rev. B **21**, 3222.

Filippetti, A., and N. A. Spaldin, 2003, Phys. Rev. B **67**, 125109.

Fukumura, T., Z. Jin, M. Kawasaki, T. Shono, T. Hasegawa, S. Koshihara, and H. Koinuma, 2001, Appl. Phys. Lett. **78**, 958.

Fukumura, T., Y. Yamada, H. Toyosaki, T. Hasegawa, H. Koinuma, and M. Kawasaki, 2004, Appl. Surf. Sci. **223**, 62.

Fukushima, T., K. Sato, and H. Katayama-Yoshida, 2004, Jpn. J. Appl. Phys., Part 2 **43**, L1416.

Fukushima, T., K. Sato, H. Katayama-Yoshida, and P. H. Dederichs, 2006a, Jpn. J. Appl. Phys., Part 2 **45**, L416.

Fukushima, T., K. Sato, H. Katayama-Yoshida, and P. H. Dederichs, 2006b, Phys. Status Solidi A **203**, 2751.

Fukushima, T., K. Sato, H. Katayama-Yoshida, and P. H. Dederichs, 2007, J. Phys. Soc. Jpn. **76**, 094713.

Galanakis, I., and P. H. Dederichs, 2005, *Half-Metallic Alloys* (Springer, Berlin), p. 12.

Galanakis, I., Ph. Mavropoulos, and P. H. Dederichs, 2006, J. Phys. D **39**, 765.

Gijs, M. A. M., and G. E. W. Bauer, 1997, Adv. Phys. **46**, 285.

Glas, F., G. Patriarche, L. Largeau, and A. Lemaitre, 2004, Phys. Rev. Lett. **93**, 086107.

Gonis, A., 2000, *Theoretical Materials Science* (Materials Research Society, Warrendale, PA).

Goodenough, J. B., 1955, Phys. Rev. **100**, 564.

Gopal, P., and N. A. Spaldin, 2006, Phys. Rev. B **74**, 094418.

Greenwood, D. A., 1958, Proc. Phys. Soc. London **71**, 585.

Gu, L., S. Wu, H. Liu, R. Singh, N. Newman, and D. Smith, 2005, J. Magn. Magn. Mater. **290-291**, 1395.

Gyorffy, B. L., A. J. Pindor, J. Staunton, G. M. Stocks, and H. Winter, 1985, J. Phys. F: Met. Phys. **15**, 1337.

Haldane, F. D. M., and P. W. Anderson, 1976, Phys. Rev. B **13**, 2553.

Harrison, W. A., 1989, *Electronic Structure and the Properties of Solids* (Dover, New York).

Hellsvik, J., *et al.*, 2008, Phys. Rev. B **78**, 144419.

Hilbert, S., and W. Nolting, 2004, Phys. Rev. B **70**, 165203.

Hilbert, S., and W. Nolting, 2005, Phys. Rev. B **71**, 113204.

Hohenberg, P., and W. Kohn, 1964, Phys. Rev. **136**, B864.

Iuşan, D., B. Sanyal, and O. Eriksson, 2006, Phys. Rev. B **74**, 235208.

Jamet, M., A. Barski, T. Devillers, V. Poydenot, R. Dujardin, P. Bayle-Guillemaud, J. Rothman, E. Bellet-Amalric, A. Marty, J. Cibert, R. Mattana, and S. Tatarenko, 2006, Nature Mater. **5**, 653.

Janisch, R., P. Gopal, and N. A. Spaldin, 2005, J. Phys.: Condens. Matter **17**, R657.

Janisch, R., and N. A. Spaldin, 2006, Phys. Rev. B **73**, 035201.

Janotti, A., and C. G. Van de Walle, 2007, Phys. Rev. B **76**, 165202.

Jung, S. W., S. J. An, G. C. Yi, C. U. Jung, S. I. Lee, and S. Cho, 2002, Appl. Phys. Lett. **80**, 4561.

Jungwirth, T., J. Sinova, J. Maśek, J. Kućera, and A. H. MacDonald, 2006, Rev. Mod. Phys. **78**, 809.

Jungwirth, T., K. Y. Wang, J. Masek, K. W. Edmonds, J. König, J. Sinova, M. Polini, N. A. Goncharuk, A. H. MacDonald, M. Sawicki, A. W. Rushforth, R. P. Campion, L. X. Zhao, C. T. Foxon, and B. L. Gallagher, 2005, Phys. Rev. B **72**, 165204.

Kanamori, J., 1959, J. Phys. Chem. Solids **10**, 87.

Kanamori, J., and K. Terakura, 2001, J. Phys. Soc. Jpn. **70**, 1433.

Katayama-Yoshida, H., 1987, Int. J. Mod. Phys. B **1**, 1207.

Katayama-Yoshida, H., K. Kusakabe, H. Kizaki, and A. Nakanishi, 2008, Appl. Phys. Express **1**, 081703.

Katayama-Yoshida, H., K. Sato, T. Fukushima, M. Toyoda, H.

Kizaki, V. A. Dinh, and P. H. Dederichs, 2007a, J. Magn. Magn. Mater. **310**, 2070.

Katayama-Yoshida, H., K. Sato, T. Fukushima, M. Toyoda, H. Kizaki, V. A. Dinh, and P. H. Dederichs, 2007b, Phys. Status Solidi A **204**, 15.

Katayama-Yoshida, H., and A. Zunger, 1984, Phys. Rev. Lett. **53**, 1256.

Katayama-Yoshida, H., and A. Zunger, 1985a, Phys. Rev. B **31**, 7877.

Katayama-Yoshida, H., and A. Zunger, 1985b, Phys. Rev. B **31**, 8317.

Katayama-Yoshida, H., and A. Zunger, 1985c, Phys. Rev. Lett. **55**, 1618.

Katayama-Yoshida, H., and A. Zunger, 1986, Phys. Rev. B **33**, 2961.

Katsnelson, M. I., and A. I. Lichtenstein, 2000, Phys. Rev. B **61**, 8906.

Kawazoe, H., M. Yasukawa, H. Hyodo, M. Kurita, H. Yanagi, and H. Hosono, 1997, Nature (London) **389**, 939.

Kirkpatrick, S., 1973, Rev. Mod. Phys. **45**, 574.

Kittel, C., 1987, *Quantum Theory of Solids* (Willey, New York).

Kittilstved, K. R., N. S. Norberg, and D. R. Gamelin, 2005, Phys. Rev. Lett. **94**, 147209.

Kizaki, H., K. Sato, and H. Katayama-Yoshida, 2005, Jpn. J. Appl. Phys., Part 1 **44**, L1187.

Kizaki, H., K. Sato, and H. Katayama-Yoshida, 2006, Physica B **376-377**, 812.

Kobayashi, M., Y. Ishida, J. I. Hwang, G. S. Song, A. Fujimori, C.-S. Yang, L. Lee, H.-J. Lin, D.-J. Huang, C. T. Chen, Y. Tanaka, K. Terai, S.-I. Fujimori, T. Okane, Y. Saitoh, K. Kobayashi, A. Tanaka, H. Saito, and K. Ando, 2007, J. Supercond. Nov. Magn. **20**, 467.

Kohn, W., and L. Sham, 1965, Phys. Rev. **140**, A1133.

Kolesnik, S., and B. Dabrowski, 2004, J. Appl. Phys. **96**, 5379.

Korzhavyi, P., I. A. Abrikosov, E. A. Smirova, L. Bergqvist, P. Mohn, R. Mathieu, P. Svedlindh, J. Sadowski, E. I. Isaev, Yu. Kh. Vekilov, and O. Eriksson, 2002, Phys. Rev. Lett. **88**, 187202.

Kramers, H. A., 1934, Physica (Amsterdam) **1**, 182.

Kubo, R., 1957, J. Phys. Soc. Jpn. **12**, 570.

Kudrnovský, J., G. Bouzerar, and I. Turek, 2007, Appl. Phys. Lett. **91**, 102509.

Kudrnovský, J., I. Turek, V. Drchal, F. Máca, J. Mašek, P. Weinberger, and P. Bruno, 2003, J. Supercond. **16**, 119.

Kudrnovský, J., I. Turek, V. Drchal, F. Máca, P. Weinberger, and P. Bruno, 2004, Phys. Rev. B **69**, 115208.

Kundaliya, D. C., S. B. Ogale, S. E. Lofland, S. Dhar, C. J. Metting, S. R. Shinde, Z. Ma, B. Varughese, K. V. Ramanujachary, L. Salamanca-Riba, and T. Venkatesan, 2004, Nature Mater. **3**, 709.

Kunisu, M., F. Oba, H. Ikeno, I. Tanaka, and T. Yamamoto, 2005, Appl. Phys. Lett. **86**, 121902.

Kuroda, S., N. Nishizawa, K. Takita, M. Mitome, Y. Bando, K. Osuch, and T. Dietl, 2007, Nature Mater. **6**, 440.

Landau, D. P., and K. Binder, 2000, *A Guide to Monte Carlo Simulations in Statistical Physics* (Cambridge University Press, Cambridge).

Levien, L., C. T. Prewitt, and D. J. Weidner, 1980, Am. Mineral. **65**, 920.

Levy, P. M., S. Maekawa, and P. Bruno, 1998, Phys. Rev. B **58**, 5588.

Liechtenstein, A. I., M. I. Katsnelson, V. P. Antropov, and V. A. Gubanov, 1987, J. Magn. Magn. Mater. **67**, 65.

Lowitzer, S., S. Chadov, V. Popescu, and H. Ebert, 2007, *Verhandl*, DPG Vol. 71 (Deutsche Physikalische Gesellschaft, Regensburg), p. 437.

Luo, X., and R. M. Martin, 2005, Phys. Rev. B **72**, 035212.

MacDonald, A. H., P. Schiffer, and N. Samarth, 2005, Nature Mater. **4**, 195.

Mahadevan, P., and A. Zunger, 2004, Phys. Rev. B **69**, 115211.

Mahadevan, P., A. Zunger, and D. D. Sarma, 2004, Phys. Rev. Lett. **93**, 177201.

Mašek, J., J. Kudrnovský, F. Máca, B. L. Gallagher, R. P. Campion, D. H. Gregory, and T. Jungwirth, 2007, Phys. Rev. Lett. **98**, 067202.

Mašek, J., and F. Máca, 2004, Phys. Rev. B **69**, 165212.

Matsukura, F., H. Ohno, and T. Dietl, 2002, *Handbook of Magnetic Materials*, edited by K. H. J. Buschow (North-Holland, Amsterdam), Vol. 14, p. 1.

Matsukura, F., *et al.*, 1998, Phys. Rev. B **57**, R2037.

Metropolis, N., A. W. Rosenbluth, M. N. Rosenbluth, A. H. Teller, and E. Teller, 1953, J. Chem. Phys. **21**, 1087.

Mikkelsen, A., B. Sanyal, J. Sadowski, L. Ouattara, J. Kanski, S. Mirbt, O. Eriksson, and E. Lundgren, 2004, Phys. Rev. B **70**, 085411.

Mirbt, S., B. Sanyal, and P. Mohn, 2002, J. Phys.: Condens. Matter **14**, 3295.

Oguchi, T., K. Terakura, and N. Hamada, 1983, J. Phys. F: Met. Phys. **13**, 145.

Ohno, H., 1998, Science **281**, 951.

Ohno, H., 1999, J. Magn. Magn. Mater. **200**, 110.

Ohno, Y., D. K. Young, B. Beschoten, F. Matsukura, H. Ohno, and D. D. Awschalom, 1999, Nature (London) **402**, 790.

Okabayashi, J., A. Kimura, T. Mizokawa, A. Fujimori, T. Hayashi, and M. Tanaka, 1999, Phys. Rev. B **59**, R2486.

Oshiyama, A., N. Hamada, and H. Katayama-Yoshida, 1988, Phys. Rev. B **37**, 1395.

Oswald, A., R. Zeller, P. J. Braspenning, and P. H. Dederichs, 1985, J. Phys. F: Met. Phys. **15**, 193.

Ozaki, N., *et al.*, 2004, Prog. Solid State Chem. **1**, 957.

Pajda, M., J. Kudrnovský, I. Turek, V. Drchal, and P. Bruno, 2001, Phys. Rev. B **64**, 174402.

Pearton, S. J., W. H. Heo, M. Ivill, D. P. Norton, and T. Steiner, 2004, Semicond. Sci. Technol. **19**, R59.

Pemmaraju, C. D., R. Hanafin, T. Archer, H. B. Braun, and S. Sanvito, 2008, Phys. Rev. B **78**, 054428.

Perdew, J. P., and Y. Wang, 1986, Phys. Rev. B **33**, 8800.

Perdew, J. P., and A. Zunger, 1981, Phys. Rev. B **23**, 5048.

Petit, L., T. C. Schulthess, A. Svane, Z. Szotek, W. M. Temmerman, and A. Janotti, 2006, Phys. Rev. B **73**, 045107.

Ploog, K., S. Dhar, and A. Trampert, 2003, J. Vac. Sci. Technol. B **21**, 1756.

Prinz, G., 1998, Science **282**, 1660.

Priour, D. J., and S. D. Sarma, 2006, Phys. Rev. B **73**, 165203.

Ruban, A. V., and I. A. Abrikosov, 2008, Rep. Prog. Phys. **71**, 046501.

Ruban, A. V., M. L. Katsnelson, W. Olovsson, S. I. Simak, and A. I. Abrikosov, 2005, Phys. Rev. B **71**, 054402.

Ruban, A. V., and H. L. Skriver, 2002, Phys. Rev. B **66**, 024201.

Rusz, J., L. Bergqvist, J. Kudrnovský, and I. Turek, 2006, Phys. Rev. B **73**, 214412.

Saito, H., V. Zayets, S. Yamagata, and K. Ando, 2003, Phys. Rev. Lett. **90**, 207202.

Sandratskii, L., P. Bruno, and J. Kudrnovský, 2004, Phys. Rev. B **69**, 195203.

Sandratskii, L. M., and P. Bruno, 2002, Phys. Rev. B **66**, 134435.

Sandratskii, L. M., and P. Bruno, 2006, Phys. Rev. B **73**, 045203.

Sarigiannidou, E., *et al.*, 2006, Phys. Rev. B **74**, 041306.

Sato, K., P. H. Dederichs, and H. Katayama-Yoshida, 2003, Europhys. Lett. **61**, 403.

Sato, K., P. H. Dederichs, and H. Katayama-Yoshida, 2006, Physica B **376-377**, 639.

Sato, K., P. H. Dederichs, and H. Katayama-Yoshida, 2007a, J. Phys. Soc. Jpn. **76**, 024717.

Sato, K., P. H. Dederichs, and H. Katayama-Yoshida, 2007b, *28th International Conference on the Physics of Semiconductors (ICPS2006) Proceedings* (AIP, New York).

Sato, K., P. H. Dederichs, H. Katayama-Yoshida, and J. Kudrnovský, 2004, J. Phys.: Condens. Matter **16**, S5491.

Sato, K., T. Fukushima, and H. Katayama-Yoshida, 2007a, Jpn. J. Appl. Phys., Part 2 **46**, L682.

Sato, K., T. Fukushima, and H. Katayama-Yoshida, 2007b, Jpn. J. Appl. Phys., Part 2 **46**, L1120.

Sato, K., and H. Katayama-Yoshida, 2000, Jpn. J. Appl. Phys., Part 2 **39**, L555.

Sato, K., and H. Katayama-Yoshida, 2001a, Jpn. J. Appl. Phys., Part 2 **40**, L334.

Sato, K., and H. Katayama-Yoshida, 2001b, Jpn. J. Appl. Phys., Part 2 **40**, L485.

Sato, K., and H. Katayama-Yoshida, 2001c, Jpn. J. Appl. Phys., Part 2 **40**, L651.

Sato, K., and H. Katayama-Yoshida, 2002, Semicond. Sci. Technol. **17**, 367.

Sato, K., H. Katayama-Yoshida, and P. H. Dederichs, 2005, Jpn. J. Appl. Phys., Part 2 **44**, L948.

Sato, K., W. Schweika, P. H. Dederichs, and H. Katayama-Yoshida, 2004, Phys. Rev. B **70**, 201202(R).

Schulthess, T. C., W. M. Temmerman, Z. Szotek, W. H. Butler, and G. M. Stocks, 2005, Nature Mater. **4**, 838.

Schulthess, T. C., W. M. Temmerman, Z. Szotek, A. Svane, and L. Petit, 2007, J. Phys.: Condens. Matter **19**, 165207.

Sharma, P., A. Gupta, K. V. Rao, F. J. Owens, R. Sharma, R. Ahuja, J. M. Osorio Guillen, B. Johansson, and G. A. Gehring, 2003, Nature Mater. **2**, 673.

Shi, Z. P., P. M. Levy, and J. L. Fry, 1994, Phys. Rev. B **49**, 15159.

Shiba, H., 1971, Prog. Theor. Phys. **46**, 77.

Shick, A., V. Drchal, and J. Kudrnovský, 2004, Phys. Rev. B **69**, 125207.

Sluiter, M. H. F., Y. Kawazoe, P. Sharma, A. Inoue, A. R. Raju, C. Rout, and U. V. Waghmare, 2005, Phys. Rev. Lett. **94**, 187204.

Spaldin, N. A., 2004, Phys. Rev. B **69**, 125201.

Stauffer, D., and A. Aharony, 1994, *Introduction to Percolation Theory*, 2nd ed. (Taylor & Francis, New York).

Staunton, J., B. L. Gyorffy, A. J. Pindor, G. M. Stocks, and H. Winter, 1985, J. Phys. F: Met. Phys. **15**, 1387.

Sullivan, J. M., and S. C. Erwin, 2003, Phys. Rev. B **67**, 144415.

Swendsen, R. H., and J. S. Wang, 1987, Phys. Rev. Lett. **58**, 86.

Tay, M., Y. H. Wu, G. C. Han, T. C. Chong, Y. K. Zheng, S. J. Wang, Y. B. Chen, and X. Q. Pan, 2006, J. Appl. Phys. **100**, 063910.

Thompson, S. M., 2008, J. Phys. D **41**, 093001.

Timm, C., 2003, J. Phys.: Condens. Matter **15**, R1865.

Toyoda, M., H. Akai, K. Sato, and H. Katayama-Yoshida, 2006, Physica B **376**, 647.

Tuomisto, F., K. Pennanen, K. Saarinen, and J. Sadwski, 2004, Phys. Rev. Lett. **93**, 055505.

Turchi, P. E., G. M. Stocks, W. H. Butler, D. M. Nicholson, and A. Gonis, 1988, Phys. Rev. B **37**, 5982.

Turek, I., K. Carva, and J. Kudrnovský, 2006, Adv. Sci. Technol. (Faenza, Italy) **52**, 1.

Turek, I., V. Drchal, J. Kudrnovský, M. Šob, and P. Weinberger, 1997, *Electronic Structure of Disordered Alloys, Surfaces and Interfaces* (Kluwer Academic, Boston).

Turek, I., J. Kudrnovský, V. Drchal, and P. Bruno, 2006, Philos. Mag. **86**, 1713.

Turek, I., J. Kudrnovský, V. Drchal, L. Szunyogh, and P. Weinberger, 2002, Phys. Rev. B **65**, 125101.

Turek, I., J. Kudrnovský, V. Drchal, and P. Weinberger, 2004, J. Phys.: Condens. Matter **16**, S5607.

Vaithyanathan, V., C. Wolverton, and L. Q. Chen, 2002, Phys. Rev. Lett. **88**, 125503.

Velický, B., 1969, Phys. Rev. **184**, 614.

Velický, B., S. Kirkpatrick, and H. Ehrenreich, 1968, Phys. Rev. **175**, 747.

Wang, F., and D. P. Landau, 2001, Phys. Rev. E **64**, 056101.

Webster, P. J., and K. R. A. Ziebeck, 1988, *Alloys and Compounds of d-Elements with Main Group Elements* (Springer, Berlin), p. 75.

Weinberger, P., 1990, *Electron Scattering Theory for Ordered and Disordered Matter* (Clarendon, Oxford).

Wierzbowska, M., D. Sánchez-Portal, and S. Sanvito, 2004, Phys. Rev. B **70**, 235209.

Wolf, S., *et al.*, 2001, Science **294**, 1488.

Wolff, U., 1989, Phys. Rev. Lett. **62**, 361.

Wyckoff, R. W. G., 1963, *Crystal Structures* (Interscience, New York), Vol. 1, p. 111.

Yamamoto, T., and H. Katayama-Yoshida, 1997, Jpn. J. Appl. Phys., Part 2 **36**, L180.

Yu, J. L., M. van Schilfgaarde, and G. D. Samolyuk, 2005, Phys. Rev. Lett. **94**, 097201.

Yuasa, S., A. Fukushima, H. Kubota, Y. Suzuki, and K. Ando, 2006, Appl. Phys. Lett. **89**, 042505.

Zener, C., 1951a, Phys. Rev. **82**, 403.

Zener, C., 1951b, Phys. Rev. **81**, 440.

Zhang, J., R. Skomski, and D. J. Sellmyer, 2005, J. Appl. Phys. **97**, 10D303.

Zunger, A., 1986, in *Solid State Physics*, edited by F. Zeits, H. Ehrenreich, and D. Turnbull (Academic, New York), Vol. 39, p. 275.

Zunger, A., S. H. Wei, L. G. Ferreira, and J. E. Bernard, 1990, Phys. Rev. Lett. **65**, 353.

Žutić, I., J. Fabian, and S. Das Sarma, 2004, Rev. Mod. Phys. **76**, 323.